

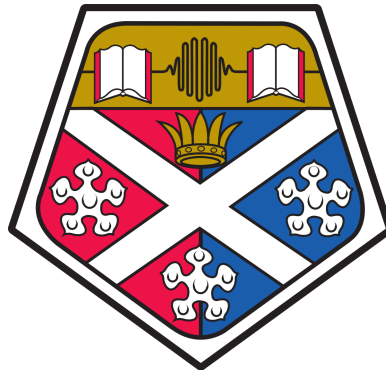
---

---

MULTI-CHANNEL OPTICAL PROBING OF HIGH POWER  
LASER-PLASMA INTERACTIONS

---

---



Written By

ZOË ELEANOR DAVIDSON

The University of Strathclyde

Department of Physics

Glasgow, Scotland

in partial fulfilment of the requirements for the degree of Doctor of Philosophy in  
Physics 2023

*All that I am, and all that I achieve, I owe to my mum - Jacqueline.*

## ABSTRACT

This thesis reports on the development of a multi-channel optical probe and the role it has in investigating when self-focusing of a high power laser pulse occurs, and what parameters it depends on in a variety of high intensity laser-plasma interaction experimental set-ups, including: in a gas jet; in preplasma on the front side of a solid target; and in a sharp density transition generated by a blade in the flow of a supersonic gas jet. These experimental set-ups are environments typically used to explore the interaction physics of channel formation, ion acceleration, laser wakefield acceleration, and x-ray generation. This new insight would enable us to gain better control of self-focusing in these experiments which could lead to utilising self-focusing as an intensity enhancement feature.

The multi-channel optical probe was developed as part of this research, to address a need for a temporally resolving diagnostic which enabled multiple 2D spatial measurements of the laser-plasma dynamics in a single interaction. The first results chapter details the development of this new approach, including the motivation, concept, optical design, and proof of concept results. The results demonstrated the need for a new diagnostic such as the multi-channel probe, to minimise the interference of shot-to-shot fluctuations on our understanding on evolving plasma dynamics, and also to complement simulation investigations. The second results

chapter explores the self-focusing in the preplasma of an opaque target, by using the multi-channel probe to measure the plasma expansion on the front side of the target. In this chapter nominal intensity versus actual on-shot intensity is discussed, as maximum proton energies emerge that exceed our calculations for nominal intensity. The final results chapter explains how the multi-channel optical probe can be adapted for use on a femto-second laser system, towards providing femtosecond resolution. In the experiment reported, the multi-channel probe is used to measure the propagation dynamics and degree of filamentation evolving when x-ray harmonics are emitted due to a newly discovered mechanism named Burst Intensification by Singularity Emitting Radiation (BISER). This experiment involves the use of a blade in the flow of a supersonic gas jet to generate electron injection by density transition, in laser wakefield acceleration. The results reported demonstrate how the multi-channel probe can enhance our understanding of laser-plasma dynamics across a range of research areas.

## DECLARATION OF AUTHORS RIGHTS

This thesis is the result of the author's original research. It has been composed by the author and has not been previously submitted for examination which has led to the award of a degree.

The copyright of this thesis belongs to the author under the terms of the United Kingdom Copyright Acts as qualified by University of Strathclyde Regulation 3.50. Due acknowledgement must always be made of the use of any material contained in, or derived from, this thesis.

Signed:

Date:

## ACKNOWLEDGEMENTS

Thank you to the Engineering and Physical Sciences Research Council (EPSRC) for funding this PhD, and to the Japan Society for the Promotion of Science (JSPS) for funding my summer fellowship.

I would like to thank Professor Paul McKenna for the opportunity to complete a PhD in his research group. Paul supported me to apply for grants to attend the American Physical Society Plasma Physics conference in the US, and in my application to the JSPS summer fellowship which enabled me to collaborate internationally. My application to JSPS would also not have been a success if it were not for the encouragement and guidance of Professor David Neely, who sadly passed away in 2020. David's passion for science was infectious and his explanations were nothing short of captivating. I have a fond memory of excitedly sharing the outcome of my JSPS summer fellowship application with David in person, and Paul on the other end of the phone. I thank both for their enthusiasm, guidance and support throughout my PhD.

Thank you to Dr Martin King for his proofreading and support with simulations. Thank you to Dr Ross Gray, my original supervisor and the inventor of the multi-channel probe, who offered me this PhD position.

I thank the members of the laser-plasma research groups I have worked with based at the University of Strathclyde, University of York, University of Belfast, the Central Laser Facility, and the Kansai Photon Science Institute, who were supportive

and friendly to work with. I am especially grateful to Dr Ceri Brenner and Dr Kate Lancaster for their unwavering support on and off experiments.

My time at Strathclyde was made significantly better thanks to the friendships built with: Jim Denholm, Bruno Gonzalez–Izquierdo, Kirsten Munro, Gail McConnell, Alison Yao, Marco Reggiani, Jessica Gagnon, Mollie McFarlane, Jordan Murray, Katrina Wesencraft, Samantha Hume, Sam Williamson. Thank you for cheering me up, and on, on more than one occasion.

All of my current colleagues in Radiotherapy Physics at the Northern Centre for Cancer Care in Newcastle upon Tyne have been a huge support this past year as I worked full time while completing this thesis. I am especially grateful to Adriana Paul, Marieke van der Putten, Liam Walker, and my line manager Judith Mott.

Thank you to my family and friends who have been incredibly patient, understanding and supportive throughout this journey. A special thanks to my parents, my aunt Sue, and my dear friends Ailis Ovens, Eilidh Muir, Bethany Ross, Hayleigh Jarrett, and Robyn Bell.

I dedicate this thesis to underrepresented people working in physics, who are often the *only* in a room. We like to hope being underrepresented has little relevance in how we are treated in science environments however, sadly we know this to be untrue [1–8]. For what it is worth, this is dedicated to you: the ones who were; those that still are; and those who just wanted to be, physicists.

## ROLE OF AUTHOR

This thesis contains the research undertaken by the author throughout her PhD at the University of Strathclyde. The results are taken from two experimental campaigns, both of which the author played a key role in. The first experimental campaign, reported in Chapters 4 and 5, was performed at the Rutherford Appleton Laboratories, in Oxford, and led by Dr Ross Gray, who co-supervised this work with Prof. Paul McKenna. The second experimental campaign was performed at the Kansai Photon Science Institute (KPSI), in Nara, led by Dr Alexander Pirozhkov. The author's role pre- and post- experiment, was done so under the supervision of Prof. David Neely and Prof. Paul Mckenna. The author's role in the experimental design, set-up, execution, measurement and analysis of these experimental campaigns are detailed below.

**Chapters 4 and 5:** The results reported in these chapters are from one experimental campaign undertaken in the first year of the author's PhD. In this experimental campaign the author was responsible for assisting Dr Ross Gray, Dr Bruno Gonzalez Izquierdo, and Dr Adam Higginson in the set-up of the multi-channel probe in the Target Area West of the Vulcan laser system. The author was also responsible for the RCF stack and for summarising all of the data measured each day on the campaign. Following the experiment, the author was responsible for all data analysis. Dr Martin King performed all of the 2D PIC simulations.

**Chapter 6:** The data reported in this chapter was from the experimental campaign performed on the J-Karen-P laser system. The author was in their second year of their PhD when we undertook an 8 week summer fellowship funded by JSPS. The author was responsible for the redesign of the multi-channel optical probe, and the packing and shipping of all equipment from the University of Strathclyde to KPSI. Under the supervision of the principal investigator of this collaborative experiment, Dr Alexander Pirozohkov, the author was responsible for building and alignment of the multi-channel probe, and the calibrations. During the experiment the author was solely responsible for the filtering and execution of the cameras implemented in the multi-channel probe, and a daily summary of the findings in preliminary observations to help to guide the next day of the experiment. The author analysed all of the experimental data presented, associated with the multi-channel probe. Dr Martin King performed all of the 2D PIC simulations and provided support in the analysis.

## PUBLICATIONS

1. **Influence of spatial-intensity contrast in ultraintense laser–plasma interactions**

R. Wilson, M. King, N. M. H. Butler, D. C. Carroll, T. P. Frazer, M. J. Duff, A. Higginson, R. J. Dance, J. Jarrett, **Z. E. Davidson**, C. Armstrong, H. Liu, S. J. Hawkes, R. J. Clarke, D. Neely, R. J. Gray, and P. McKenna, Scientific Reports, 12, 1910, 2022.

2. **Enhanced laser intensity and ion acceleration due to self–focusing in relativistically transparent ultrathin targets**

T. P. Frazer, R. Wilson, M. King, N. M. H. Butler, D. C. Carroll, M. J. Duff, A. Higginson, J. Jarrett, **Z. E. Davidson**, C. Armstrong, H. Liu, D. Neely, R. J. Gray, and P. McKenna, Physical Review Research, 6, 2, 2020.

3. **High order mode structure of intense light fields generated via a laser–driven relativistic plasma aperture**

M. J. Duff, R. Wilson, M. King, B. Gonzalez-Izquierdo, A. Higginson, S. D. R. Williamson, **Z. E. Davidson**, R. Capdessus, N. Booth, S. Hawkes, D. Neely, R. J. Gray, and P. McKenna, Scientific Reports, 10, 105, 2020.

4. **Self–referencing spectral interferometric probing of the onset time of relativistic transparency in intense laser–foil interactions**

S. D. R. Williamson, R. Wilson, M. King, M. Duff, B. Gonzalez-Izquierdo,

**Z. E. Davidson**, A. Higginson, N. Booth, S. Hawkes, D. Neely, R. J. Gray, and P. McKenna, *Physical Review Applied*, 14, 3, 2020.

5. **An optically multiplexed single-shot time-resolved probe of laser-plasma dynamics**

**Z. E. Davidson**, B. Gonzalez Izquierdo, A. Higginson, K. L. Lancaster, S. D. R. Williamson, M. King, D. Farley, D. Neely, P. McKenna, and R. J. Gray, *Optics Express*, 27, 4, 2019.

6. **Bremsstrahlung emission from high power laser interactions with constrained targets for industrial radiography**

C. D. Armstrong, C. M. Brenner, C. Jones, D. R. Rusby, **Z. E. Davidson**, Y. Zhang, J. Wragg, S. Richards, C. Spindloe, P. Oliveira, M. Notley, R. Clarke, S. R. Mirfayzi, S. Kar, Y. Li, T Scott, P. McKenna, and D. Neely, *High Power Laser Science and Engineering*, 7, e24, 2019.

# CONTENTS

ACKNOWLEDGEMENTS .....	IV
ROLE OF AUTHOR .....	VI
PUBLICATIONS.....	VIII
1 INTRODUCTION .....	1
1.1 THESIS OUTLINE .....	4
2 THE UNDERPINNING PHYSICS OF LASER-PLASMA INTERACTIONS .....	7
2.1 PLASMA .....	7
2.2 IONISATION PROCESSES .....	10
2.3 LASER INTERACTIONS WITH A PLASMA .....	15
2.4 ABSORPTION MECHANISMS.....	16
2.4.1 COLLISIONAL ABSORPTION .....	17
2.4.2 COLLISIONLESS ABSORPTION.....	17
2.5 PROPAGATION DYNAMICS IN UNDERDENSE PLASMA .....	20
2.5.1 CHANNEL FORMATION.....	20
2.5.2 SELF-FOCUSING .....	21
2.5.3 FILAMENTATION.....	23

2.5.4	WAKEFIELD ACCELERATION .....	24
2.6	INTERACTIONS WITH OVERDENSE OPAQUE TARGETS .....	27
2.6.1	FRONT SURFACE PLASMA EXPANSION .....	28
2.6.2	ION ACCELERATION MECHANISMS.....	28
3	METHODOLOGY .....	31
3.1	HIGH POWER LASER FACILITIES .....	31
3.1.1	VULCAN, RAL .....	32
3.1.2	J-KAREN-P, KPSI.....	34
3.2	DIAGNOSTIC TECHNIQUES .....	35
3.2.1	RADIOCHROMIC FILM .....	36
3.2.2	XUV SPECTROGRAPH.....	37
3.3	NUMERICAL MODELLING .....	38
3.3.1	HELIOS .....	38
3.3.2	EPOCH PIC .....	39
4	THE MULTI-CHANNEL OPTICAL PROBE .....	40
4.1	TEMPORALLY RESOLVED IMAGING AND LASER-PLASMA INTERAC- TIONS .....	41
4.2	MULTI-CHANNEL PROBE DESIGN.....	44
4.3	PROOF OF CONCEPT.....	48
4.4	SUMMARY AND CONCLUSIONS .....	57
5	THE MULTI-CHANNEL OPTICAL PROBE & FRONT SURFACE PLASMA DYNAMICS .....	59
5.1	EXPERIMENTAL METHODS .....	60
5.2	EXPERIMENTAL RESULTS .....	67
5.3	SIMULATION RESULTS .....	87

5.4	SUMMARY AND CONCLUSION.....	94
6	THE MULTI-CHANNEL OPTICAL PROBE ON A FEMTO-SECOND LASER SYSTEM.....	98
6.1	EXPERIMENTAL METHODS.....	100
6.2	EXPERIMENTAL RESULTS.....	108
6.3	SIMULATION RESULTS.....	114
6.4	SUMMARY AND CONCLUSION.....	122
7	SUMMARY AND PERSPECTIVES.....	124
7.1	THE MULTI-CHANNEL PROBE.....	124
7.2	THE MULTI-CHANNEL PROBE MEASURING FRONT SURFACE DYNAMICS	126
7.3	THE MULTI-CHANNEL PROBE AND FILAMENTATION WHEN A BLADE IS INSERTED INTO A GAS JET.....	127
7.4	REFLECTIONS AND FUTURE WORK.....	128

## INTRODUCTION

The physics of high power laser–plasma interactions involves the interplay of energy between photons and matter through ionisation and absorption mechanisms. The study of laser–plasma interactions became established in 1964 [9–11] soon after the invention of the laser in 1960 [12, 13]. Since then, many sub–fields of high power laser–plasma interactions have developed, including some with promising applications, such as: an alternative, compact particle accelerator [14, 15] and radiation source[16]; and as an environment to explore the fundamental energetic plasma physics that naturally occurs within our universe[17].

High power lasers enable the investigation of energetic plasma processes in the laboratory. Intensity scales with laser energy, and inversely with the irradiation area and pulse duration. A huge step towards maximising intensity was the development of Chirped Pulse Amplification (CPA) [18]. In 1985, Strickland and Mourou developed a method that changed the possibilities and direction of laser–plasma interaction physics forever. This was recognised in their shared award of the Nobel Prize in Physics in 2018. By using a dispersive element to spectrally and temporally stretch a

laser pulse, more energy could be pumped into the amplifying crystal and extracted by the laser pulse without damaging the optics, before compressing the pulse duration back down. This breakthrough changed the design of high power laser systems across the world, and enabled experimentalists to work with relativistically intense laser pulses ( $>10^{18}$  W/cm<sup>2</sup> for  $\lambda > 1\mu\text{m}$ ). In 1997, Optical Parametric Chirped Pulse Amplification (OPCPA) was proposed by Ross *et al.* [19] to further enhance intensities while minimising the limiting effect of bandwidth narrowing introduced by CPA. OPCPA was designed as a simple addition to a CPA high power laser system, whereby the stretched laser pulses would first have their frequency bandwidth broadened through an optical parametric amplifier before continuing on the CPA path of amplification and compression [19]. Although not necessary to achieve sub-picosecond laser pulses, when used in conjunction with CPA, the amplified pulse was compressed to an ultra-short pulse length ( $\tau < 1$  ps) with minimal bandwidth narrowing, resulting in even high laser intensities.

One of the key parameters in delivering high on-target intensity is minimising the pulse duration. Although beneficial for on-target intensities, this means that the very environments we have created to study have very short lifetimes, and the intricate dynamics that we are most interested in measuring evolve on femto- to picosecond timescales. As our laser systems develop to produce shorter laser pulses, this challenge will become harder. It is necessary we have diagnostics that can keep up with these shortening timescales, especially imaging diagnostics that enable us to track and measure the plasma evolution on short timescales.

A popular route to imaging laser-plasma interactions is by shadowgraphy and interferometry via a pump-probing arrangement [20]. A probe pulse is typically a single laser pulse created from a pick-off of the main (pump) laser pulse earlier in the laser system chain and is a non-converging beam. A pick-off is typically used for ease

as it has the same properties and characteristics as the main pulse, and makes timing control simpler than using two separate laser systems. The path length of the probe pulse, between the pick-off point and the interaction point, can be varied to control the time at which it probes the laser-plasma interaction in relation to the main pulse. In laser-plasma experiments, shadowgraphy is the imaging technique whereby the region of interest (typically at target centre) is illuminated by the probe pulse, and the areas that have density exceeding that of the critical density will appear opaque to the probe pulse and deflect the incident photons, whereas the lower density regions will allow the probe light to transmit. The resultant probe pulse can then be measured by a CCD camera which detects a 2D shadow-like image. The implementation of interferometry in laser-plasma experiments is typically in a Normarski style [21] arrangement where a focusing lens, Wollaston prism and polariser is positioned after the laser-target interaction region to create an interference pattern of the plasma density that is then measured by a CCD camera [22].

Both imaging techniques are highly effective at providing insight into the propagation and plasma expansion dynamics of laser-plasma interactions, however in this typical pump-probe arrangement the frequency of probing is limited to one image per interaction. As a workaround, many experiments have built a timing scan of the evolving plasma dynamics by accumulating one image per interaction while increasing the delay of the probe pulse with each repeated single laser-plasma interaction [23]. This method requires each repeated interaction to have the same constant laser-plasma conditions, which is often not realistically possible, especially for low repetition rate high power laser systems [24]. As a result, timing scans of the evolving plasma dynamics measured over repeated interactions are susceptible to error through shot-to-shot variations, and therefore do not give us a reliable understanding of the evolution of a single laser pulse interaction in its entirety [25–28].

This challenge is not limited to laser–plasma physics either, as there are other research areas that seek to image the evolution of stochastic events on ultra–short timescales [25], which are not easily reproducible under the same unique conditions such as: irreversible chemical reaction dynamics [29], and pump–probe microscopy [30].

As high power laser technology continues to develop to maximise on–target intensity, the pulse durations, and the timescales that the laser–plasma interaction dynamics evolve over, will continue to shorten. It is crucial that we also continually develop our diagnostics to be versatile and reliable in measuring the plasma dynamics on similar timescales. This thesis details the development of a novel optical multi–channel probe technique to help address this challenge. The multi–channel probe seeks to provide a deeper understanding of an entire single laser–plasma interaction; minimise the effects of shot–to–shot variations and error in our understanding of the evolving interaction dynamics; and to better complement the various sample time frames of simulated interactions.

## 1.1 THESIS OUTLINE

To give the reader an understanding of the underpinning physics that will be discussed in this thesis, Chapter 2 begins by introducing the mechanisms in which energy is transferred from a high power laser pulse to matter, and how plasma is generated in this process. The key mechanisms explored include: the behaviour of channel formation, filamentation, plasma turbulence, self–focusing, plasma expansion and XUV production which are all central to the results that follow.

Chapter 3 describes the key methods used in the experiments that will follow and also in the supporting simulations. The experimental methods includes: the main optical components of high power laser systems, radiochromic film, and the

spectrometer.

In Chapter 4 the development and implementation of the multi-channel probe is presented, along with the proof of concept results where the novel diagnostic was implemented into a high power laser experiment for the first time. The multi-channel probe is then used to image channel formation in underdense plasma over four time frames, and measure the change in channel gradient as an indicator of self-focusing. These results are also published in the author's first, first author publication - Davidson et al. [31]. This behaviour is measured for multiple interactions while the pressure of the helium gas jet is increased from 20 bar to 100 bar.

Chapter 5 investigates the role of the multi-channel probe in a solid target experiment to measure changes in the target front surface conditions when intensity is increased by laser energy or defocus position. Measurements made with radiochromic film and backscatter spectra are also reported to indicate any impact the changes in method of intensity control has on proton acceleration and hole-boring velocities. The comparison between interactions where intensity is scaled by laser energy and defocus position was also investigated in 2D EPOCH particle-in-cell simulations, the results of which are reported and compared to the experimental findings in Chapter 4.

In Chapter 6 the multi-channel probe is adapted for use on the femtosecond high power laser system, J-KAREN-P, at Kansai Photon Science Institute in Nara, Japan as part of a larger experiment investigating Burst Intensification by Singularity Emitting Radiation (BISER) [32–34]. The results reported in this chapter explore the propagation dynamics when a high power laser pulse interacts with a supersonic helium gas jet plume with a steep density gradient (up-ramp) induced by a blade positioned within the gas jet. Filamentation is the main propagation dynamic analysed, and is quantified with an image analysis tool I developed in Python using

signal thresholding and peak finding. The number of filaments is reported as an indicator of energy loss in the interaction, and with this its relation to on-target intensity and XUV production is investigated.

Chapter 7 summarises the results reported in this thesis, and discusses the future for the multi-channel probe in high power laser-plasma interaction experiments.

## THE UNDERPINNING PHYSICS OF LASER-PLASMA INTERACTIONS

This chapter discusses the fundamental physics associated with laser-plasma interactions. In particular this will focus on the background physics related to this thesis, such as: ionisation, absorption mechanisms, laser pulse propagation dynamics, self-focusing, particle acceleration, X-ray generation, and plasma expansion, filamentation and turbulence.

### 2.1 PLASMA

"What is plasma?" is typically the first question new researchers to the field of laser-plasma physics ask. This is a deceptively simple question with a complex answer. Simply put, it can be described as the fourth state of matter after solid, liquid and gas. Plasma is an ionised gas, meaning that the electrons within the atomic particles, in the gas, have been excited by an energy source which results in some electrons being liberated from their atoms to become "free electrons" – more on the different

types of ionisation processes to come. However, it is important to understand that not all ionised gases are plasma and there are several significant properties that must be met in order for an ionised gas to be considered as one.

The first of these conditions is: plasma has quasineutral charge and exhibits *collective behaviour* from external fields affecting the plasma as a whole. Due to protons being significantly heavier than electrons, ions are assumed to be stationary when an electric field is applied, and so the plasma motion is considered to be solely from electrons. For collective behaviour to dominate, the scale length of the plasma ( $L$ ) must be greater than a distance called the *Debye shielding distance* ( $\lambda_D$ ), in all directions,  $L \gg \lambda_D$ . The Debye shielding distance is defined by:

$$\lambda_D = \sqrt{\frac{\epsilon_0 k_B T_e}{e^2 n_e}} \quad (2.1)$$

where  $\epsilon_0$  is the permittivity of free space,  $k_B$  is Boltzmann's constant,  $T_e$  is the temperature of the electrons,  $e$  is the electron charge and  $n_e$  is the unperturbed electron density. Therefore, the Debye sphere is defined by a radius equal to  $\lambda_D$ , and beyond the Debye sphere, the electric field of a particle cannot affect other charged particles. It is critical that many charged particles must be present within this sphere to ensure the collective behaviour dominates the plasma entirely.

There also exists collisional and collisionless plasma. The mean-free path of a particle is the average distance it can travel before colliding with another particle. Collisionless plasmas are defined such that the mean-free path of the electrons is significantly greater than the plasma scale length,  $L$ , and therefore exhibits lower collision frequency than the plasma frequency,  $\omega_p$ . Derived originally from Maxwell's Equations, the plasma frequency is defined as the rate at which electrons oscillate

within a plasma:

$$\omega_p = \sqrt{\frac{n_e e^2}{\epsilon_0 m_e}} \quad (2.2)$$

where  $n_e$  is the electron density of the plasma, and  $m_e$  is the mass of an electron. From Maxwell's Equations, we know that the movement of charged particles changes the electric field, which in turn results in a change to the magnetic field, and vice-versa. This is crucial to our understanding of plasma behaviour, as plasma induces its own electromagnetic fields and currents, and because it is ultimately dominated by electromagnetic forces.

### Maxwell's Equations of Electromagnetism

(in differential form)

$$\vec{\nabla} \cdot \vec{E} = \frac{\rho}{\epsilon_0} \quad (2.3)$$

$$\vec{\nabla} \cdot \vec{B} = 0 \quad (2.4)$$

$$\vec{\nabla} \times \vec{E} = -\frac{\partial \vec{B}}{\partial t} \quad (2.5)$$

$$\vec{\nabla} \times \vec{B} = \epsilon_0 \vec{J} + \epsilon_0 \mu_0 \frac{\partial \vec{E}}{\partial t} \quad (2.6)$$

where  $\vec{E}$  is the electric field,  $\rho$  is the charge density,  $\vec{B}$  is the magnetic field,  $\vec{J}$  is the current density, and  $\mu_0$  is the vacuum permeability.

These four equations unify electricity and magnetism, which is fundamental to our understanding of electromagnetic waves and their propagation. However, it is the reduction of Maxwell's equations into the Lorentz equation that describes how materials with charged particles are influenced by external electromagnetic fields:

$$\vec{F} = q\vec{E} + q\vec{v} \times \vec{B} \quad (2.7)$$

where  $\vec{F}$  is the Lorentz force on a charged particle,  $q$  is charge,  $\vec{E}$  is the electric field,  $\vec{v}$  is the particle velocity, and  $\vec{B}$  the magnetic field. These sets of equations are central to our understanding of laser-plasma interactions.

Derived from the Lorentz force law, Ampere's law and Faraday's law, is the the Poynting vector ( $\vec{S}$ ) which demonstrates the energy flux density of an electromagnetic field. From this, the laser intensity is defined as the time-average Poynting vector:

$$I = |\langle \vec{S} \rangle| = \left\langle \frac{1}{\mu_0} \vec{E} \times \vec{B} \right\rangle \quad (2.8)$$

where  $\vec{E}$  and  $\vec{B}$  are the electric and magnetic field equations.

## 2.2 IONISATION PROCESSES

As we briefly touched on in the last section, for a plasma to be produced, ionisation must occur. Ionisation is a process that results in an atom acquiring charge by either gaining or losing electrons. In its simplest form, *the photoelectric effect* is the basic description of a primary stimulated emission ionisation process, described by Albert Einstein in 1905, that suggests that when light is incident on the surface of a material it can either be reflected, transmitted or absorbed. If the photon has sufficient energy ( $\hbar\omega$ ), it can overcome the electron's binding energy ( $E_{\text{ion}}$ ), and can be absorbed. As a result the electron will gain this kinetic energy ( $E_f = \hbar\omega - E_{\text{ion}}$ ) and enter a higher *excited state* before ejecting an electron of the same energy value from the, now ionised, material. In laser-plasma interactions, intensities are so high that there are numerous ionisation mechanisms occurring. Next we will explore the different types of ionisation processes that occur within laser-plasma interactions, and the laser intensities at which each process dominates.

Multi-photon ionisation is a spontaneous emission ionisation process that involves

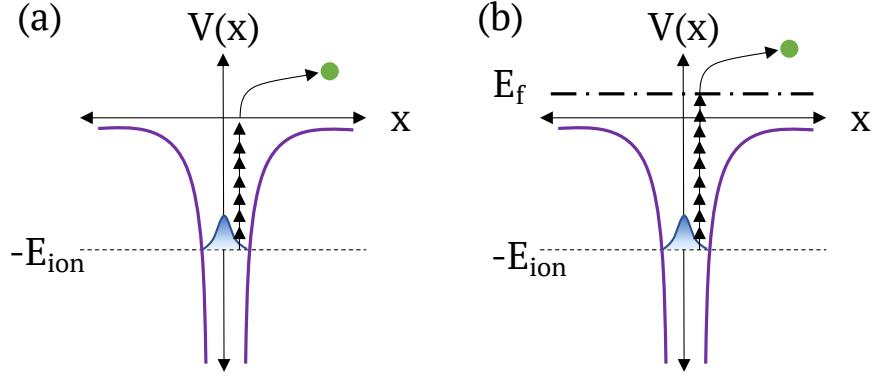


FIGURE 2.1 – Schematic of (a) multi-photon ionisation, and (b) above-threshold ionisation, where  $E_{\text{ion}}$  is the ionisation energy needed to overcome the binding energy of the electron,  $V(x)$  is the Coloumb potential,  $x$  is distance, and  $E_f$  is the final energy of the electron.

the absorption of several moderately energetic photons before ejecting an excited electron. This was first observed in 1965 by Voronov and Delone, and most commonly occurs with laser intensities  $I_L > 1 \times 10^{10} \text{ W cm}^{-2}$ . Multi-photon ionisation can be defined by:

$$n\hbar\omega = E_{\text{ion}} \quad (2.9)$$

where  $n$  is the number of photons, and  $\hbar\omega$  is the photon energy. This process is spontaneous, and less predictable than other ionisation processes, because it requires a number of photons, specific to the element, to be absorbed by an atom to cumulatively have sufficient energy to supersede  $E_{\text{ion}}$ , and propel the electron from its bound state, as depicted in Figure 2.1(a). The number of photons ( $n$ ) absorbed by atom is defined by the N-photon ionisation rate ( $\Gamma_n$ ):

$$\Gamma_n = \sigma_n I_L^n \quad (2.10)$$

where  $\sigma_n$  is the cross-section of the N-photon ionisation rate. The ionisation rate increases with increasing laser intensity, as there is a higher probability of ionisation

with increased photon density. This becomes complex at laser intensities greater than the atomic binding intensity, as other non-linear ionisation mechanisms dominate: tunnelling and over-the-barrier.

The binding energy of the electron can be derived by equating the centripetal and Coulomb forces, which counteract each other while the electron is in a stable orbit:

$$E_{\text{ion}} = -\frac{e}{8\pi\epsilon_0 r_0} eV \quad (2.11)$$

where  $r_0$  is the electron orbital radius, which for hydrogen is the Bohr radius  $a_B$ .

The electric field strength is:

$$E_a = \frac{e}{4\pi\epsilon_0 a_B^2} \quad (2.12)$$

which when combined with the Poynting vector  $\vec{S}$  (equation 2.8), translates to the atomic binding threshold intensity:

$$I_a = \frac{\epsilon_0 c E_a^2}{2} \quad (2.13)$$

where  $E_a$  remains constant throughout laser propagation and unaffected by the laser field.

Above threshold ionisation is similar to multi-photon ionisation, however the electron absorbs a larger number of photons than is required for ionisation, and gives the ejected electron significantly more kinetic energy on emission, as shown in Figure 2.1(b). In this case, the electron has more momentum and probability of provoking secondary ionisation than an electron emitted by multi-photon ionisation.

Tunnelling ionisation occurs with laser intensities of  $I_L > 1 \times 10^{15} \text{ W cm}^{-2}$ . At these intensities,  $I_L$  begins to approach the atomic binding threshold intensity of

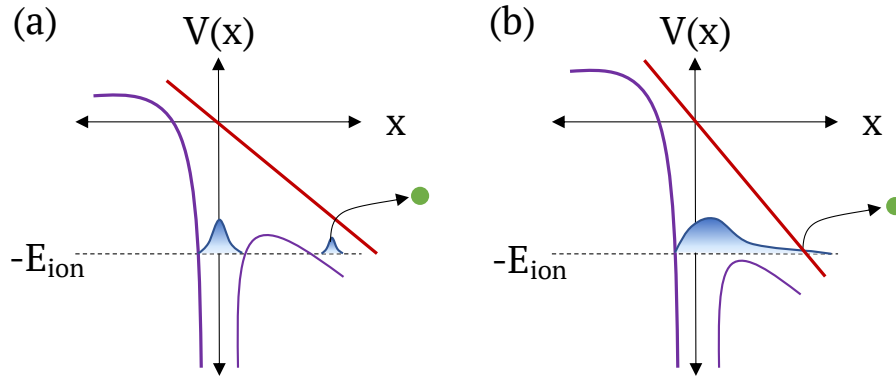


FIGURE 2.2 – Schematic of (a) tunnelling ionisation, and (b) over the barrier ionisation.

the material  $I_a$ , and so the effect of the laser field on the atomic binding potential must be considered. In this case, the potential well is deformed which results in the ionisation threshold  $E_{\text{ion}}$  lowering on one side and being enhanced on the other, as shown in Figure 2.2(a). Note, the asymmetrical suppression and enhancement of the potential well oscillates with the electric field oscillations. Quantum mechanically, this means that the probability that the electron can now tunnel through the barrier is finite and must be considered. This also means that if the potential well drops below the ionisation potential barrier,  $E_{\text{ion}}$ , for an even stronger applied electric field, the barrier could be suppressed altogether giving name to "over-the-barrier" ionisation, as shown in Figure 2.2(b). With the barrier suppressed below the ionisation potential barrier, electrons are free to leave the potential well. This is the main ionisation mechanism induced by high power laser pulses, where the laser intensity ( $\approx 10^{18} - 10^{19} \text{ W cm}^{-2}$ ) easily exceeds atomic binding intensity and suppresses the ionisation barrier. For reference, the intensity threshold for barrier suppression in hydrogen is  $I_L > 1 \times 10^{14} \text{ W cm}^{-2}$  [35]. This process is part of the laser field ionisation stage. Fundamentally, plasma formation is guaranteed if the laser intensity is greater than the atomic binding intensity,  $I_L > I_a$ .

The Keldysh parameter ( $\gamma_k$ ) is an approximation that offers a condition to distinguish between when multi-photon ionisation and tunnelling may occur, it is defined by:

$$\gamma_k = \omega_L \sqrt{\frac{2E_{\text{ion}}}{I_L}} \approx \sqrt{\frac{E_{\text{ion}}}{2\phi_{\text{pond}}}} \quad (2.14)$$

where  $\omega_L$  is the angular frequency, and  $\phi_{\text{pond}}$  is the ponderomotive potential. The ponderomotive potential is defined by:

$$\phi_{\text{pond}} = \frac{e^2 E_L^2}{4m\omega_L^2} \quad (2.15)$$

which is a representation of the energy gained by an oscillating electron in a laser field. The ponderomotive force,  $F_p$ , pushes electrons from regions of high intensity to regions of low intensity:

$$F_p = -\frac{1}{4} \frac{e^2}{\gamma m \omega_L^2} \nabla E^2 \quad (2.16)$$

The ponderomotive force plays a role in a number of plasma dynamics, such as in channel formation, in driving plasma waves, and laser self-focusing. The Keldysh parameter looks at the ratio of ionisation threshold  $E_{\text{ion}}$  and  $\phi_{\text{pond}}$  ponderomotive potential. When  $\gamma_k \gg 1$  it is said that multi-photon ionisation occurs as the laser has high frequency but low field strength – which leaves the potential well unaffected. When  $\gamma_k \ll 1$ , tunnelling ionisation dominates with low laser frequency and strong laser field strength that deforms the potential well and lowers the ionisation threshold. It is important to note – these Keldysh conditions do not rule out the presence of other ionisation mechanisms, they simply state that one ionisation mechanism dominates over the others in these given circumstances. Quantifying the boundaries of the switching on and off of such mechanisms is a long standing goal for many physicists, especially when observing the interplay of complex dynamics evolving in

laser–plasma physics.

### 2.3 LASER INTERACTIONS WITH A PLASMA

When a laser pulse has sufficient intensity and irradiates matter, electrons can be stripped from the material through the ionisation processes described. This depends on the combination of laser parameters and chosen target material, since every material has a specific electronic structure and ionisation threshold. As previously discussed, if the incident laser pulse has energy in excess of the ionisation threshold, the material will become ionised and the electrons will be free to move and become a plasma. Due to the Gaussian intensity profile of a laser pulse, the ionisation mechanism that is dominant will vary with intensity throughout the interaction.

The dispersion relation is at the root of electromagnetic wave propagation in plasma and therefore important to understand for the role it has in laser–plasma interaction physics. Dispersion can be described as the phenomenon whereby refractive index ( $\eta$ ) depends on frequency ( $\omega$ ):

$$\eta = \frac{ck}{\omega} \quad (2.17)$$

The plasma dispersion relation, derived from Maxwell’s equations, for an electromagnetic wave is represented by:

$$\omega^2 = c^2k_0^2 + \omega_p^2 \quad (2.18)$$

The solutions to this dispersion relation show that laser frequencies,  $\omega$ , must be larger than the plasma frequency  $\omega_p$  in order for the laser light to propagate in the plasma. When  $\omega = \omega_p$ , the laser light is reflected from a surface of critical density ( $n_c$ ), defined

by:

$$n_c = \frac{\omega_L^2 \epsilon_0 \gamma m_e}{e^2} \quad (2.19)$$

where  $\gamma$  is the relativistic factor. The relativistic factor accounts for the increase in electron mass at relativistic laser intensities, in this case the critical density is increased and allows more propagation of laser light than previously possible at non-relativistic laser intensities. In some cases, entire targets can become transparent to the laser light through this process called relativistically induced transparency (RIT). When  $\omega > \omega_p$ ,  $n < n_c$ , the plasma is said to be underdense; and when  $\omega < \omega_p$ ,  $n > n_c$ , the plasma is overdense. Underdense plasma is typically formed in gaseous targets or within the pre-plasma expansion on the surface of solid targets. Overdense plasma is typically formed from irradiating solid targets. In, and between, these two density states, very different plasma dynamics can be observed. In this thesis, chapters 4 and 6 will report underdense plasma results, while chapter 5 will report overdense plasma results. From the plasma dispersion relation, when the critical density condition ( $\omega_p = \omega_L$ ) is met,  $c^2 k_0^2$  would tend to zero and the threshold at which the laser can no longer propagate would be met. Below the critical density the solution is imaginary and therefore the wave is evanescent.

## 2.4 ABSORPTION MECHANISMS

After the ionisation and plasma formation, the laser pulse continues to interact with the plasma, absorption mechanisms couple energy from the laser light to the electrons, and transfer energy to the ions, within the plasma. Absorption mechanisms can be characterised as collisional or collisionless. The following subsections will outline the most common of these processes.

### 2.4.1 COLLISIONAL ABSORPTION

Inverse bremsstrahlung is the main collisional absorption mechanism. Bremsstrahlung is the "braking radiation" process whereby a charged particle is decelerated in the presence of strong electromagnetic fields, typically from a nucleus of a larger particle, which results in the generation of an X-ray by the law of conversion of energy. Inverse bremsstrahlung is just as the name suggests, where charged particles collide and energy is absorbed from a photon. The result of the absorption of a photon in the presence of an ion, accelerates an electron to carry this energy away. In low intensity regimes ( $< 10^{14} \text{ W cm}^{-2}$ ), inverse bremsstrahlung is the dominant absorption mechanism because the collisional frequency rate of electrons ( $\nu_{ei}$ ) within the underdense plasma is significantly higher than the laser pulse duration. The collisional frequency rate can be represented by:

$$\nu_{ei} \propto k_B T_e^{-3/2} \quad (2.20)$$

where  $k_B$  is Boltzmann's constant and  $T_e$  is the electron temperature.

### 2.4.2 COLLISIONLESS ABSORPTION

The laser absorption mechanisms in collisionless plasma are discussed. The movement of energy in a collisionless plasma is dominated by electrostatic interactions. Resonance, Vacuum/Brunel heating, and  $\vec{J} \times \vec{B}$  absorption processes are detailed below.

#### 2.4.2.1 RESONANCE ABSORPTION

Resonance absorption is the dominant collisionless absorption mechanism for long scale length plasmas ( $L_s$ ), that are longer than the laser wavelength ( $\lambda_L$ ), for laser

intensities between  $10^{12} - 10^{17} \text{ W cm}^{-2}$ . It is an electric-field-driven energy transfer mechanism that occurs in high density plasma at the critical surface,  $n_c$ . This mechanism transfers energy by driving electrons parallel to the density gradient of the plasma, deeper into the plasma with every electric field cycle of the laser pulse. To do this, the laser light needs to be p-polarised, and the incident laser pulse oblique to the target surface. As the laser pulse propagates deeper into the plasma, and the electron density increases, the laser pulse undergoes refraction. The oblique angle of incidence is now crucial, because it causes the laser light to arrive at the point of reflection prematurely, when the electron density,  $n_e = n_c \cos^2(\theta)$ , instead of at the critical surface,  $n_c$ . At this point of reflection, the laser pulse has refracted to the point that the electric field is now oscillating parallel to the plasma density gradient, driving electrons into reflection surface at  $n_c \cos^2(\theta)$ . Beyond this surface, the electric field evanescently decays which results in the oscillating electrons having a decaying weak restoring force which is needed to pull them back from beyond the  $n_c \cos^2(\theta)$  surface. This collisionless absorption mechanism is optimised when resonance occurs – the plasma frequency,  $\omega_p$ , matches the laser frequency  $\omega_L$ . The plasma wave of electrons mobilised by this process oscillate resonantly at the critical surface, with a frequency of  $\omega_L$ . Beyond  $I_L > 10^{17} \text{ W cm}^{-2}$ , relativistic effects dominant over resonance absorption.

#### 2.4.2.2 VACUUM / BRUNEL HEATING

Vacuum heating is an absorption mechanism that occurs in high density plasma. Although similar to resonant absorption, it is significantly less efficient as the electrons interact with just one laser cycle. In the first half of the laser cycle the electrons are pulled into the vacuum by the electric field, and the second half then re-accelerates them back into the target and beyond the corrected critical surface,  $n_c \cos^2(\theta)$ . For

this to occur, the laser pulse needs to be p-polarised and, unlike resonance absorption,  $L_s \ll \lambda_L$ . The efficiency of vacuum heating is dependent on the angle of incidence, and the energy gained is on the order of the ponderomotive potential. This mechanism also differs to resonance, in that, the electrons can easily escape the laser field beyond the corrected critical surface, which results in a net acceleration to the electron.

### 2.4.2.3 $\mathbf{J} \times \mathbf{B}$ HEATING / PONDEROMOTIVE FORCE

For laser pulses at relativistic intensities, the magnetic field component ( $\vec{v} \times \vec{B}$ ) of the Lorentz equation is no longer negligible and the  $\vec{J} \times \vec{B}$  collisionless absorption mechanism dominates for interactions with solid targets. For this process to occur, high density plasma is needed with a linearly polarised laser pulse interacting at a normal angle to the target surface. At normal incidence the electric field component, of a linearly polarised pulse, is perpendicular to the target surface, which optimises the  $\vec{J} \times \vec{B}$  force driving the electrons longitudinal oscillation into and beyond the critical surface, along the laser direction. The force applied to the electrons along the laser  $\vec{k}$ -vector direction, by the  $\vec{J} \times \vec{B}$  mechanism is:

$$\vec{F} = -\frac{m_e}{4} \frac{\delta \vec{v}_0}{\delta x} \left(1 - \frac{1 - e_1^2}{1 + e_1^2} \cos(2\omega_L t)\right) \quad (2.21)$$

where  $e_1$  is the ellipticity of the laser and  $e_1 = 0$  for linearly polarised light and  $e_1 = 1$  for circularly polarised light.

The first term in the equation,  $-\frac{m_e}{4} \frac{\delta v_0}{\delta x}$ , is the ponderomotive force —which will be described in more detail in the next section. The second term,  $\frac{1 - e_1^2}{1 + e_1^2} \cos(2\omega_L t)$ , is the  $\vec{J} \times \vec{B}$  component which drives the electrons along the laser axis oscillating at  $2\omega_L$ . This second term demonstrates that the  $\vec{J} \times \vec{B}$  heating is maximised for linearly polarised incident laser light, when  $e_1 = 0$ . As the longitudinally oscillating electrons

approach the critical surface, some can be accelerated beyond the influence of the restoring force from the laser field, yielding a net energy gain.  $\vec{J} \times \vec{B}$  heating is the absorption mechanism in high density plasma that occurs when the magnetic field dominates and the Lorentz force occurs.

## 2.5 PROPAGATION DYNAMICS IN UNDERDENSE PLASMA

At higher intensities, the dominant effect is from the ponderomotive force. This is a time integrated force exerted on electrons that is proportional to the gradient of the electric field squared,

$$\vec{F}_p = -\frac{e^2}{4m_e\omega_L^2}\nabla\vec{E}^2 \quad (2.22)$$

where  $\nabla\vec{E}$  is the gradient of the electric field. Due to the transverse intensity profile of the laser, this results in electrons moving with an overall drift velocity from high intensity regions around the propagation axis, to lower intensity regions towards the outer edge of the laser pulse spatial profile. The ponderomotive force is described as time integrated as the electrons oscillate about back and forth while travelling to the outer edge of the laser profile, as depicted in Figure 2.3. The restoring force opposing the ponderomotive decreases with time until the electrons cannot be moved any further at the laser spatial edge in the focal plane. The ponderomotive force is responsible for driving a number of effects that can be observed when a laser propagates in an underdense plasma, such as *channel formation* and *self focusing* [36].

### 2.5.1 CHANNEL FORMATION

The ponderomotive force results in the gradual build-up of electron dense channels either side of the path of the laser pulse as it propagates. During laser propagation,

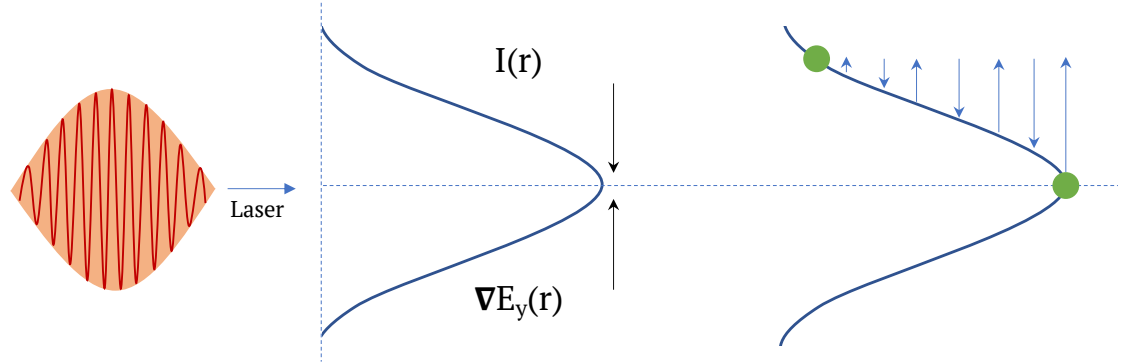


FIGURE 2.3 – Schematic of the radial view of an incoming laser pulse demonstrating the intensity  $I(r)$  and electrical field  $E(r)$  gradients increasing towards the centre of the focal spot ( $r=0$ ), and the depleting restoring force of electrons (green spheres) around the radial axis as they move from regions of high intensity to low intensity.

the ponderomotive force expels the electrons from the peak of the pulse, sweeping them out towards the wings of the laser pulse intensity profile. This time-integrated build-up of electrons on the wings joins together to form channel walls while leaving an ion cloud contained in the channel centre due to the growing charge separation forces and the ions having greater mass. The channel walls can be used to guide the remains of the laser pulse that follows. Channel formation is an advantageous effect to exploit for some laser–plasma fields of research, such as for guiding injection in laser wakefield acceleration, and guiding the main pulse in fast ignition inertial confinement fusion [37, 38].

### 2.5.2 SELF-FOCUSING

Self-focusing is a non-linear, self-generated effect where the laser converges to a point earlier than the natural beam waist as a result of plasma dynamics [39]. The typical characteristics of this are the steepening of the channel walls, increase in channel gradient, and decrease in channel width with propagation distance. The two main causes for self-focusing in plasma are ponderomotive and relativistic effects.

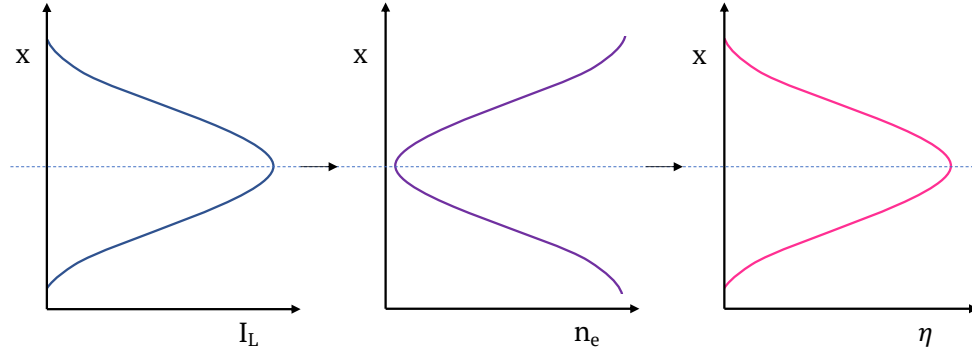


FIGURE 2.4 – Graphical representation of the radial intensity profile about the laser pulse central axis; the subsequent electron density profile due to the ponderomotive force, and the resultant refractive index profile leading to self-focusing of the laser pulse.

Just as the laser pulse propagation affects the motion of free electrons, the movement of the free electrons then alters the behaviour of the propagating laser pulse. In response to the intensity profile of the incoming laser pulse, as shown in Figure 2.4, the ponderomotive force redistributes the electrons to the wings of the laser pulse increasing the electron density ( $n_e$ ) here [36, 39]. As the electron density increases, the plasma frequency increases ( $\omega_p$ ), which in turn affects the refractive index ( $\eta$ ):

$$\eta = \sqrt{1 - \left(\frac{\omega_p}{\omega_L}\right)^2} \quad (2.23)$$

and so the refractive index changes non-uniformly on the laser profile. This change in refractive index results in a positive lens effect when  $\frac{\delta\eta}{\delta r} < 0$ , where  $\delta r$  is the change in radial coordinate.

Relativistic self focusing is also the result of a non-uniform change in refractive index across the spatial profile of laser pulse. However, it is induced by the high intensity profile of a laser pulse producing relativistic electrons at the centre of the focal spot. Due to relativistic effects, the electrons gain relativistic mass and their oscillations decrease in frequency [40, 41]. This changes the profile of plasma frequency,

as it increases towards the outer edge of the profile. The refractive index changes with the ratio of the speed of light to the phase velocity, and so the non–uniform refractive index profile is shaped. This results in the centre of the beam having a lower refractive index than at the wings, as shown schematically in Figure 2.4. In the correct environment, relativistic self–focusing can also counteract diffraction so that the two competing processes are balanced over many Rayleigh ranges [36]. For this balance to occur, the laser pulse power,  $P_0$  needs to be greater than the critical power,  $P_C$ , which can be expressed by:

$$P_0 > P_C = 17.4 \frac{\omega_0^2}{\omega_p^2} [GW] \quad (2.24)$$

### 2.5.3 FILAMENTATION

Filamentation is a non–linear transverse instability that causes the laser pulse to break up into micron scale high intensity branches, known as filaments [42, 43]. The onset of filamentation can be seeded by a number of instabilities such as laser break–up which can be due to an extremely strong positive lensing effect driven by self–focusing, and the electron density build–up from the ponderomotive force becoming too high. These filaments can be seen growing during an interaction through shadowgraphy or interferometry imaging techniques, and are indicative of inefficient energy coupling between the laser and plasma. It is understood that filamentation occurs as a result of opposing forces on the electrons from the ponderomotive force and self–focusing. Ultimately this results in a loss of laser intensity which decreases the energy transferred to the free electrons.

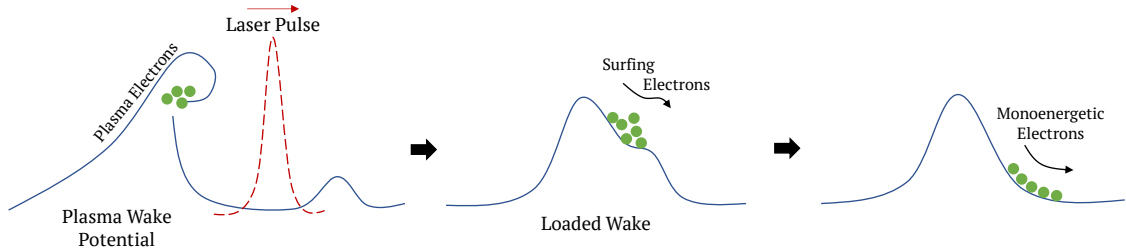


FIGURE 2.5 – Schematic depicting laser–wakefield acceleration as electrons surf on the wake of a plasma wake accelerated by a laser pulse.

### 2.5.4 WAKEFIELD ACCELERATION

Laser wakefield acceleration (LWFA) is an electron acceleration scheme that utilises the trailing wake from a high intensity laser pulse propagating in underdense plasma, which ultimately generates a plasma wave [44]. Figure 2.5 shows a simple schematic of electrons surfing on a the wake of a plasma wave. As the high intensity laser pulse drives forward through the low density plasma, the ponderomotive force sweeps the electrons out of the laser path, leaving behind ions, as already discussed. A strong charge separation is generated as a result, and in response the electrons accelerate back to their initial position but overshoot. In overshooting and rebounding, the electrons oscillate about this point at a high plasma frequency defined as:

$$\omega_p = \left( \frac{n_0 e^2}{m_e \epsilon_0} \right)^{\frac{1}{2}} \quad (2.25)$$

- thus forming the plasma wave. The strong charge separation leads to very large electric fields across the wakefield, which accelerate electrons over long distances. The electric field strength made possible in this regime surpasses the maximum acceleration gradients available in conventional radiofrequency–dependent accelerators by three orders of magnitude [45], making LWFA an even more promising field. As the electrons gain momentum ( $p_x$ ) due to the ponderomotive force ( $F_p$ ) pushing them

forward, the electric field ( $E_x$ ) experienced by the electrons from the plasma wave increases as:

$$E_x = -\frac{1}{e} \frac{dp_x}{dt} = \frac{1}{4} \frac{e}{\gamma m \omega_0^2 c} a_0^2 \omega_p \cos(\omega_p t) \quad (2.26)$$

and hence accelerates them to very high velocities [45]. A one dimensional approximation for the peak electric field achieved during LWFA was proposed by Dawson [45, 46]:

$$E_0^{WB} \approx 96 \sqrt{n_e} \quad (2.27)$$

meaning that for a typical plasma density of  $n_e = 1 \times 10^{18} \text{ cm}^{-3}$ , then  $E_0^{WB} \approx 96 \text{ GV/m}$ . When the velocity of the background plasma of density ( $n_e$ ) exceeds that of the plasma wave, the plasma wave is said to undergo wavebreaking, whereby some of the plasma electrons themselves are accelerated beyond the restoring force and the plasma wave structures is lost. For this wavebreaking condition to occur, it is assumed that the plasma wave is quasi-static with adiabatic propagation [47]. This process can be thought of as similar to when sea water breaks through a wave which was originally travelling much faster. In LWFA, wavebreaking ultimately leads to plasma electrons outrunning and escaping the plasma wave, which is not an ideal accelerating condition. To avoid electrons escaping the plasma wake prematurely, and to postpone wavebreaking, the length of the acceleration range [48] (which is dependent on the Rayleigh length,  $Z_R$ ) can be extended, and the electrons can be "trapped". Electron trapping is a name given to electrons that are accelerated in the wake of the driving plasma wave. The Rayleigh length of the laser pulse is dependent on the laser wavelength and focal spot size where  $Z_R = \frac{\pi \omega_0}{\lambda}$ , and so the plasma wavelength is usually longer than the pulse length ( $\lambda_p > \tau$ ). There are various techniques proposed to enhance the trapping of electrons, such as self-injection [49], optical injection [50], ionisation induced injection [51], but we are going to focus on discussing density

transition injection [52] as that technique is used in one of the experiments reported in this thesis.

Density transition injection is a technique based on tapering the density of the gas jet plume target either upward (called a density "up ramp") or downward (a density "down ramp") relative to the direction of the incoming laser pulse [52]. It was suggested by Bulanov [52] that a density down ramp, increases the plasma wavelength as the density decreases during laser propagation. In turn, this then lowers the phase velocity that the electrons need in order to be trapped in the wake of the plasma wave, called the trapping threshold. This technique has been shown experimentally to aid electron trapping, peak acceleration energies and energy spread [24, 53, 54]. The severity of the density gradient depends on the method implemented to shape the density ramp. The method used in this thesis, was the insertion of a razor blade in a supersonic gas jet which created a steep density jump by generating a shock front for the incoming laser pulse to transition —similar to the set-up reported by Schmid in 2010 [54]. In 2017, it was proposed from simulations by Esirkepov [55] that the addition of a blade in the flow of a supersonic gas jet can control self-focusing by the sharp density jump it generates.

#### 2.5.4.1 BISER

Burst Intensification by Singularity Emitting Radiation (BISER) was proposed by Pirozhkov in 2017 [34], and is a process whereby coherent x-rays are emitted from a relativistic laser-plasma interaction. As previously described, in LWFA a plasma wave is generated as a high intensity laser pulse drives through underdense plasma. As the pondermotive force continually pushes the electrons away from high intensity regions, cavity walls are formed as the electrons are swept aside as the plasma wave moves forward with the laser field. The multiple streams of the oscillating electrons

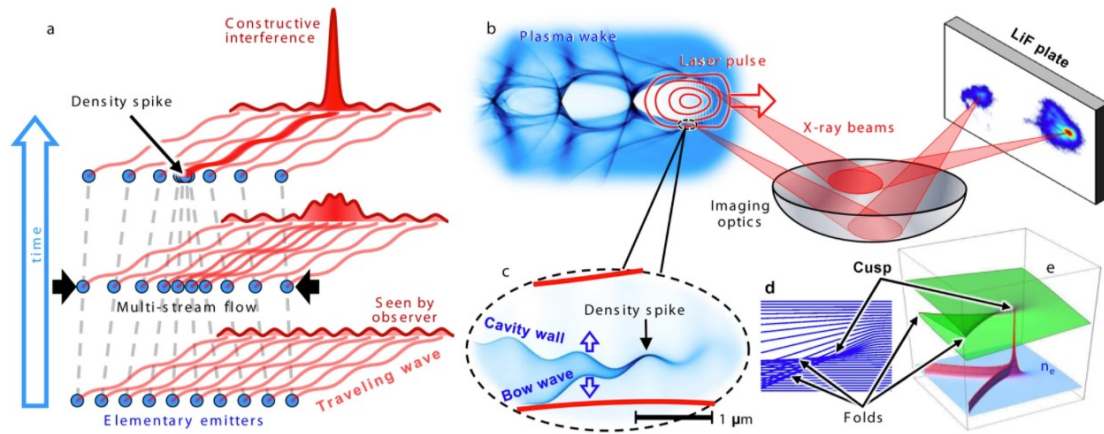


FIGURE 2.6 – Schematic of BISER taken from collaborator [34]. (a) The formation of a density spike through the convergence of a multi-stream flow. (b) Depiction of the laser pulse propagating through plasma and the emission of x-rays from the density spikes, which were focused through imaging optics and measured by a lithium fluoride (LiF) plate. (c) A zoomed in section of the density spike region of the plasma wake from the multi-stream flow of electrons sidelined by the laser field. (d, e) The density spikes form at regions of density catastrophe-point-like cusps and folds in the multi-stream flow.

at the cavity walls converge at the intersection of the bow wave and wake wave as shown in Figure 2.6. This leads to a high density spike emerging from constructive interference [34, 56]. It is within these point-like, high density sources, also called "singularities", that odd and even harmonics are generated within the spectral range of 60 to 360 eV (down to  $\approx 3.5$  nm harmonic wavelength) [32, 33]. The harmonic generation, and location of where BISER occurs, is dependent on the structure of the wake as this determines where the high-density spikes emerge as the interaction evolves.

## 2.6 INTERACTIONS WITH OVERDENSE OPAQUE TARGETS

This section details the main plasma dynamics which occur when a high power laser pulse interacts with a solid, opaque target. The interaction dynamics depend on the

laser intensity, wavelength, spot size, contrast, target material and thickness.

### 2.6.1 FRONT SURFACE PLASMA EXPANSION

Despite efforts to produce a laser pulse with little contamination from pre-pulses or Amplified Spontaneous Emission (ASE), an undesirable low intensity temporal pedestal produced by spontaneous emission in the gain media early on in the laser chain typically occurs which results in preheating of the incident target surface. Preheating can lead to plasma expansion on the front side of the target before the leading edge of the main pulse has interacted with the target. This premature plasma expansion is called preplasma, and can affect the efficiency of energy absorption and ion acceleration [57–63]. In addition to the effects of ASE or pre-pulses, the heating and pressure gradient as a result of the main laser pulse interaction would induce plasma expansion from the target into the vacuum. where the density of the plasma would decline exponentially:

$$n_e(x) = n_0 e^{-\frac{x}{L}} \quad (2.28)$$

where  $x$  is the distance away from the front of the target surface,  $L$  is the plasma scale length as previously defined, and  $n_0$  is the initial solid density of the target.

### 2.6.2 ION ACCELERATION MECHANISMS

Depending on the intensity of the incident laser pulse, a number of mechanisms can occur which will accelerate ions. Fundamentally, the forces driving these ion acceleration mechanisms can be categorised as either electromagnetic or hydrodynamic [64]. Those driven by electromagnetic forces include, target normal sheath acceleration (TNSA), radiation pressure acceleration (RPA), Coulomb explosion acceleration (CEA), skin-layer ponderomotive acceleration (SLPA), ion solitary wave acceleration

(ISWA), laser break-out afterburner (BOA), and collisionless electrostatic shock acceleration (CESA) [64]. However, in the experiments discussed in this thesis, TNSA, RPA Hole-Boring and Light Sail modes, are most relevant, and are each shown in Figure 2.7.

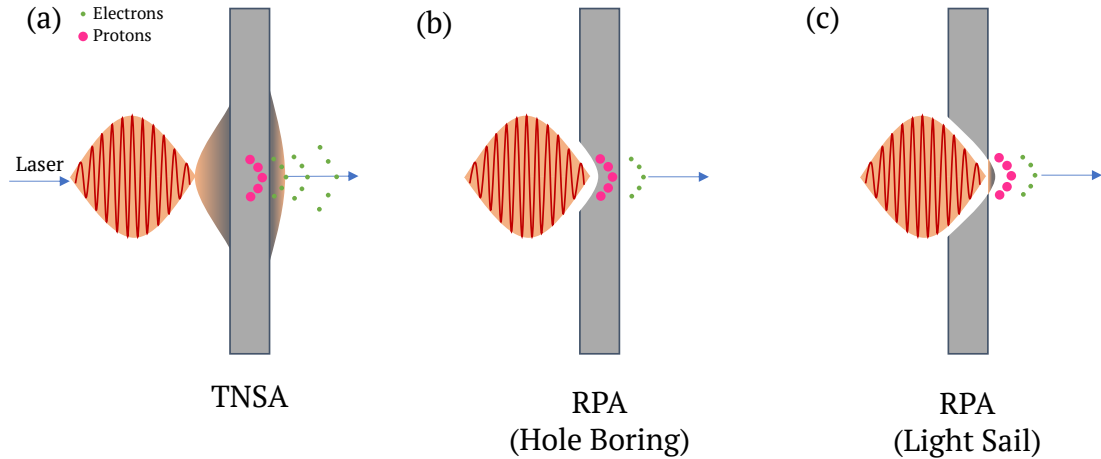


FIGURE 2.7 – Schematic representing the process of particle acceleration mechanisms in laser–solid interactions (a) TNSA, (b) RPA hole boring, and (c) RPA light sail mode.

TNSA was proposed by Wilks [65] in 2001 and involves the generation of an extremely strong electric field sheath (on the order of TV/m) on the target rear surface. When a high intensity laser pulse (greater than  $1 \times 10^{20} \text{ W cm}^{-2}$ ) interacts with a foil target of micron scale thickness, relativistic electrons are generated as a result and driven by the laser field through to the rear side of the target. The relativistic electrons collecting at the rear of the target generates a strong electric field which accelerates ions to multi-MeV energies, typically from a contaminate layer on the rear side of the target, escaping into the vacuum. Radiation pressure acceleration is the dominate acceleration mechanism for targets between micrometre and nanometre scale thickness when the incident laser pulse intensity is greater than  $1 \times 10^{21} \text{ W cm}^{-2}$  [66]. At these ultra-high intensities, the critical density surface

is deformed due to the extremely high laser pressure driving forward. The critical density surface bends inward, as if being imprinted upon by the Gaussian shape of the focal spot. The velocity at which the critical surface recesses due to RPA is called the hole-boring velocity. The motion of the critical surface into the overdense plasma generates an electrostatic field, as a charge separation layer emerges. This electrostatic field contributes to the ion acceleration as a result. For even higher laser intensities, the radiation pressure can be strong enough to push through the entire target. This is called the Light Sail mode and dominates over hole-boring RPA at these higher intensities and for targets of nanometre scale thickness. Light sail mode is optimised when the radiation pressure is balanced with the electrostatic plasma pressure, which is dependent on both laser and target parameters. If the target is not of sufficient thickness, charge separation cannot be established and Coulomb explosion of the ions will follow. However, if the target is too thick, the increase in plasma mass will lead to sub-optimal acceleration.

## METHODOLOGY

In this chapter we discuss the main optical technology behind high power laser systems and, in particular, the details of the two high power laser facilities used in the experiments reported in this thesis. The main diagnostic throughout this thesis is the multi-channel optical probe, the development of which is discussed in detail in the chapters that follow, however, in addition to the multi-channel probe, this methods chapter details how radiochromic film and an XUV spectrometer were implemented as supporting diagnostics, and which simulation methods were used.

### 3.1 HIGH POWER LASER FACILITIES

High power laser systems are of course central to high power laser-plasma experiments. As previously explained in Chapter 1, CPA and OPCPA were the breakthrough developments that enabled higher intensity laser pulses to be produced [18, 19]. Prior to the installation of CPA in high power laser systems, the peak intensity achievable was limited to  $\approx 10^{16}$  W/cm<sup>2</sup>. CPA enabled higher energy pulses to be used, and

OPCPA addressed the undesirable side effect of bandwidth narrowing caused in the CPA process [19]. Together, pulse duration and energy could be optimised to push the boundaries of high intensity laser pulses up to  $10^{23}$  W/cm<sup>2</sup> peak intensity [67].

Another undesirable effect of the amplification process in high power laser systems, is Amplified Spontaneous Emission (ASE). ASE is the amplification of low energy photons, which are produced through spontaneous emission from excited atoms within the lasing gain medium. It is important to note it is the emission of coherent photons via stimulated emission that is desired, as opposed to low energy photons being emitted sporadically in time and space, in any direction. Unfortunately, this contributes to optical noise which is then amplified later on in the laser chain. The contribution of ASE modifies the ideal Gaussian temporal–intensity profile of the main laser pulse manifests itself as a plateau shaped, temporal "pedestal" intensity profile either side of the main pulse [68], which can be of nanosecond scale duration. This is undesirable as it causes the early onset of ionisation, pre–plasma formation and can seed instabilities all before the pulse arrives at the target. The severity of the pedestal can be quantified as a ratio ( $R = I_{\text{peak}}/I_{\text{p}}$ ) comparing the peak intensity ( $I_{\text{peak}}$ ) of the main laser pulse to the pedestal intensity ( $I_{\text{p}}$ ), this parameter is termed as the laser temporal–intensity contrast ratio [68]. The higher the contrast the more prominent the main pulse is relative to the ASE, which is of course desirable if ASE effects are to be minimised. The laser pulse contrast ratio can be improved by "pedestal cleaning", either by the implementation of additional Pockels cells or plasma mirrors [68, 69].

### 3.1.1 VULCAN, RAL

The Vulcan laser system is based at the Central Laser Facility (CLF) at Rutherford Appleton Laboratory, in Oxfordshire. Vulcan is a versatile high power, neodymium–

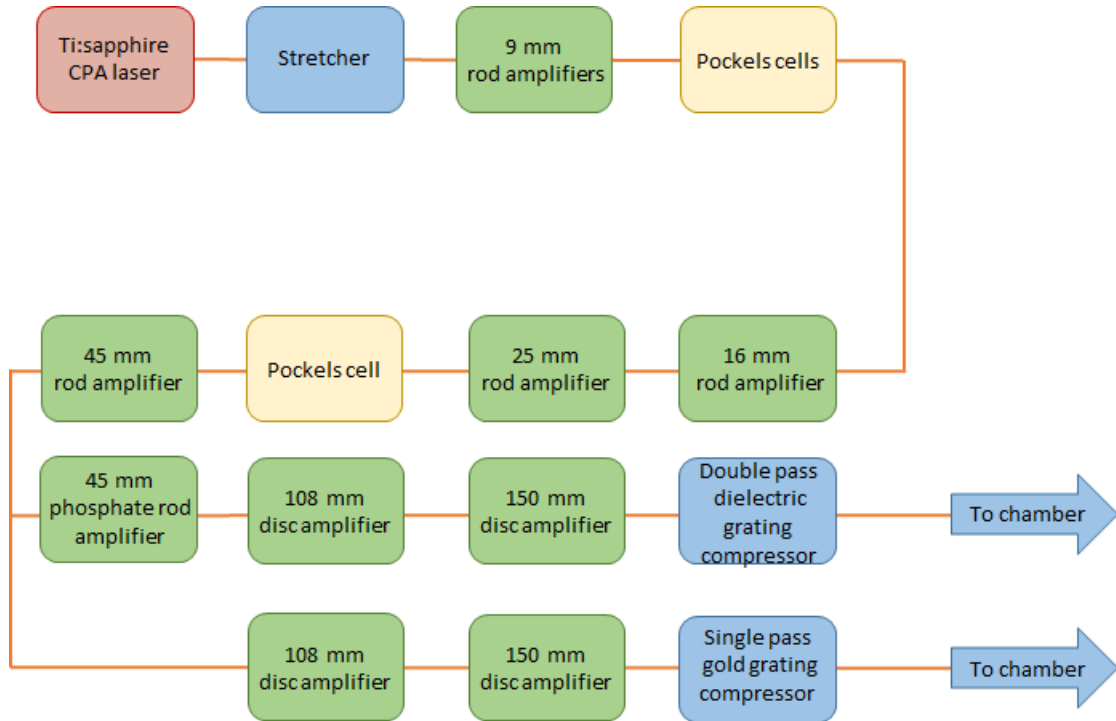


FIGURE 3.1 – Flow diagram of the key components in the Target Area West (TAW) laser chain at Rutherford Appleton Laboratory.

glass (Nd:Glass) eight pulse laser system with six long pulse, two CPA, and two target areas: Target Area Petawatt (TAP) and Target Area West (TAW). The Nd:glass lasing medium provides a central wavelength emission of 1054 nm [70]. In the experiments discussed in Chapters 4 and 5, the TAW arm of the Vulcan laser system was used in dual pulse mode for pump and probing. TAW receives two short pulse interaction beam lines ( $\approx$ ps), and six additional long pulse beams ( $\approx$ ns). As shown in Figure 3.1, from the mode-locked Ti:sapphire oscillator, which is pumped with neodymium-doped yttrium aluminium garnet (Nd:YAG), the laser pulse is first stretched before passing through a series of amplifiers, and then split in two for dual pulse mode. From here, the main interaction pulse undergoes additional amplification, before both laser pulses are compressed to durations between 0.5 - 1 ps. As a result of the extensive amplification chain built into the laser system, both beam lines have

the ability to deliver up to 250 J on target. In the experiments discussed in this thesis, the maximum laser energy is 248 J. The interaction beam achieved  $\approx 10^{19}$  W/cm<sup>2</sup> intensity, in a single 20 ps pulse, focused to a diameter of  $\approx 5.6$   $\mu$ m (FWHM) with a F/3 off-axis parabola (OAP), and the probe beam at approximately  $10^{18}$  W/cm<sup>2</sup> intensity, in a 2 ps pulse. Where F/3 denotes the f-number of the optical system, which is the ratio of the focal length and effective aperture.

### 3.1.2 J-KAREN-P, KPSI

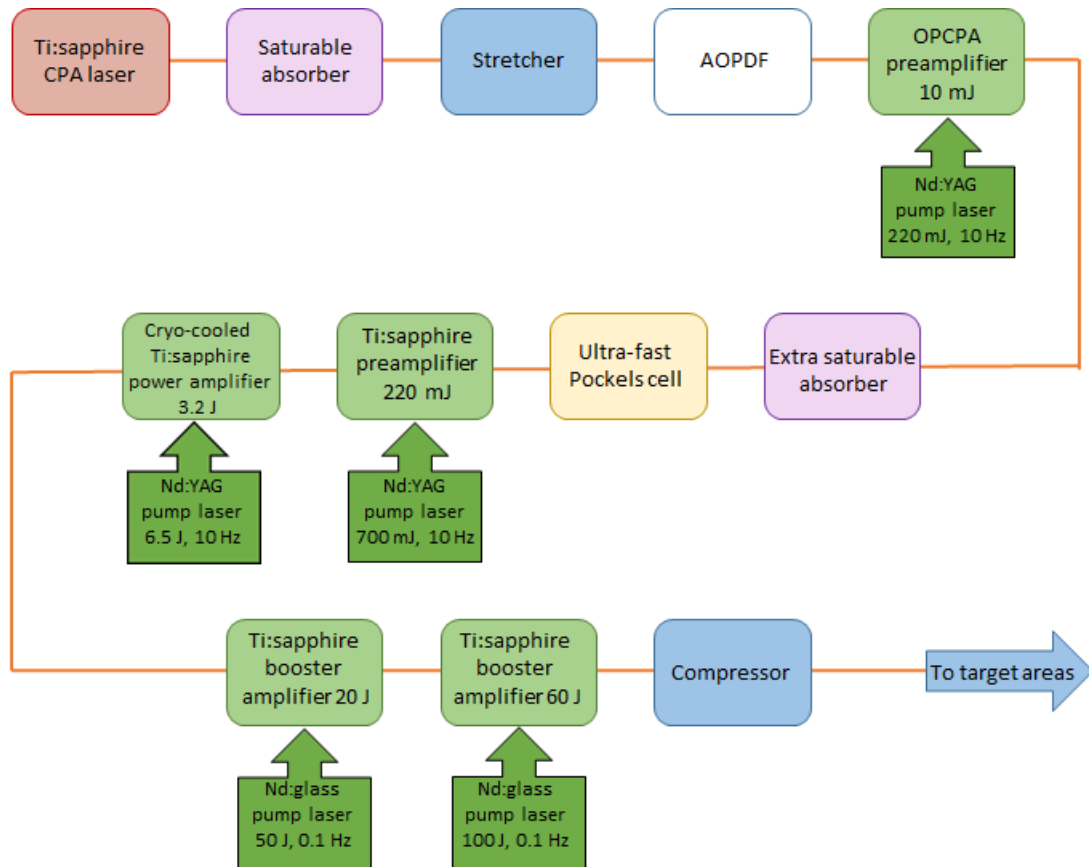


FIGURE 3.2 – Diagram of the main stages in the J-KAREN-P laser system.

The J-KAREN-P laser system, based at the Kansai Photon Science Institute in Kizugawa, Japan, is a 0.1 Hz repetition–rated, Ti:sapphire, high–power laser with

a central wavelength of 810 nm. Utilising double-CPA and OPCPA techniques [71, 72], the system can produce pulses with a maximum on-target energy of 30 J in  $\approx$  30-40 fs pulse duration resulting in a peak on-target power of  $\approx$ 1 PW with a peak intensity of  $\approx$   $10^{21}$  W/cm<sup>2</sup>, when using an F/2 OAP. In the experiment discussed in Chapter 6, the J-KAREN-P laser was operated with 0.4 J pulse energy in 27 fs pulse duration and an F/9 OAP was used to extend the acceleration range during the interaction, which resulted in a FWHM focal spot of  $\approx$ 10  $\mu$ m. In this set-up, the peak laser intensity achievable on-target is  $\approx$   $10^{18}$  W/cm<sup>2</sup>.

Figure 3.2 is a simplified flowchart diagram of the main components of the J-KAREN-P laser system [71, 72]. These include saturable absorbers and Pockels cells to minimise ASE and clean the pedestal in the pulse profile, and an acousto-optic programmable dispersive filter (AOPDF) to assist in shaping the pulse profile. The laser system uses double CPA architecture to maintain the high intensity contrast ( $10^{12}$ ) achieved in the pulse cleaning and shaping stages. A series of Ti:sapphire amplifiers are used to gradually increase the laser energy from 220 mJ to 60 J, before compression, after which the high power laser pulse is transported to the target area [71, 72]. Unlike Vulcan, TAW, there is no dual pulse mode to utilise for pump-probing technique, so a pick-off is taken from the main pulse as it enters the target area before the main pulse is focused down by the OAP.

## 3.2 DIAGNOSTIC TECHNIQUES

In addition to the multi-channel probe, radiochromic film and an XUV spectrometer were key in obtaining the results later discussed in this thesis. The details of both techniques are described in this section.

## 3.2.1 RADIOCHROMIC FILM

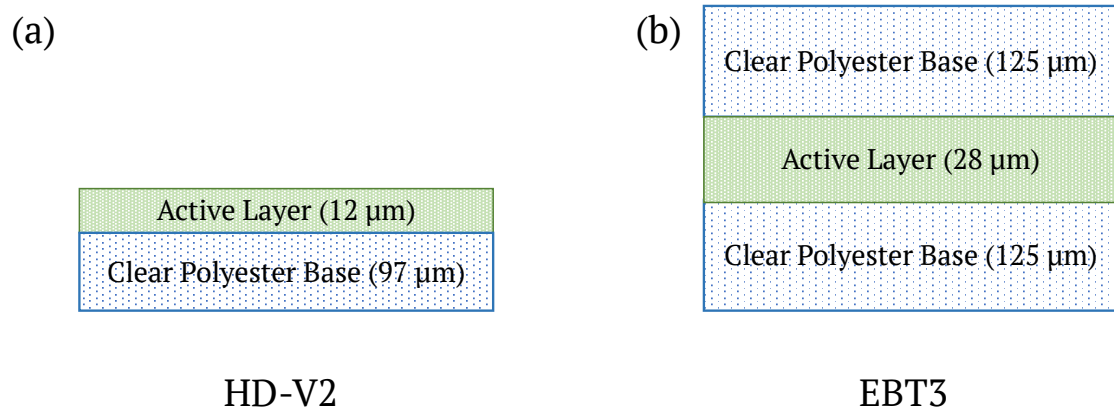


FIGURE 3.3 – Diagram of the composition of (a) HD-V2, and (b) EBT3, RCF used.

Radiochromic Film (RCF) is an ionising radiation sensitive film that self-develops through the release of dye when ionising radiation is incident on it, and is used in a range of disciplines for dosimetry. RCF changes colour, as it self-develops, due to polymerization where radiation is absorbed by photomonomer molecules in an active layer of radiation sensitive organic microcrystal. The two types of RCF used in the experiment later discussed in Chapter 5, are HDV2 and EBT3, the composition of both are shown in Figure 3.3. In laser-plasma experiments, RCF is typically used to measure the energy spectra and spatial distribution of electrons and protons incident on the film, which have been accelerated from the laser-plasma interaction. In the experiment discussed in Chapter 5, RCF is used to measure the energies of the protons accelerated from the rear surface of the target. For this use, the RCF is arranged in a stack consisting of multiple layers of RCF, interspersed with metal filters, as higher energy particles travel deeper into the stack. The number of RCF layers in the RCF stack design should be sufficient to capture the full range of the accelerated protons and electrons - our stack design included in 12 layers. Due to the characteristic Bragg peak dose deposition curve that ions have, and therefore the

steep dose fall-off, it is relatively straight forward to extract two-dimensional spatial information about incident ion beams in RCF stacks. The proton flux is determined by comparing the optical density (OD) calibrated RCF film exposed to a known proton dose from a cyclotron accelerator, where:

$$OD = \log_{10} \frac{I_0}{I_T} \quad (3.1)$$

$I_0$  is the flux of the incident light and  $I_T$  is the flux of light that is transmitted through the RCF. It is from the OD on each RCF layer that the energy spectrum can be determined.

### 3.2.2 XUV SPECTROGRAPH

Spectrographs employ a diffraction grating, to spatially separate light by wavelength; and a photodetector, to measure the intensity of this spectral light at each wavelength. Depending on the range and resolution of wavelength the user wishes to measure, different types of spectrographs are needed. In the experiment detailed in Chapter 6, a grazing-incidence flat-field spectrograph is used to measure the spectra of XUV generated by BISER [56]. This spectrograph uses a gold-coated collection mirror to maximise the input light within the XUV range. The collection mirror is followed by a spherical varied-line-space grating, leading to a back-illuminated CCD camera, more details of the XUV spectrograph can be found in [56]. The spectrograph is positioned perpendicular to the rear surface of the target, and magnets are positioned between the target and spectrograph to deflect electrons away, which could interfere with the performance of the diagnostic.

### 3.3 NUMERICAL MODELLING

In laser–plasma interactions, although many complex interactions can be produced experimentally, numerical modelling helps guide experiments and the parameters used, and also further explain experimental results in retrospect [73]. Numerical modelling allows us to simulate complex processes by repeating simplified calculations over controlled time–steps. Modelling is sometimes the only method in which some complex processes can be explored on these timescales, as they cannot be created experimentally due to a lack in resources or physical limitations. In this thesis simulations are used to compare to experimental measurements. There are many types of numerical models that can be used to simulate laser–plasma interactions, these can be categorised as hydrodynamic, kinetic, or a hybrid of both. This section will detail the radiation–hydrodynamics code, Helios, and kinetic particle–in–cell (PIC) code, EPOCH, used to provide insight into the experimental results later discussed in Chapters 4, 5, and 6.

#### 3.3.1 HELIOS

Helios is a one dimensional Lagrangian hydrodynamic model created to simulate the evolving expansion of radiating plasmas [74]. Helios simulation code can provide insight into the fast evolving dynamics of high power laser produced plasmas. As with all numerical models, assumptions are required to simplify and impose limitations on the simulations. In hydrodynamic codes, like Helios, plasma is assumed to be a fluid and treats the movement of plasma as one entity with a fluid velocity, pressure and density. Data set tables of materials are referenced by Helios to calculate relevant equations of state to describe the evolving composition of the target material and plasma during the interaction. In Chapter 5, Helios is used to simulate the front

target surface plasma expansion and determine the simulated plasma scale length to input into EPOCH PIC simulations. The table of properties selected for these simulations was PROPACEOS [75].

### 3.3.2 EPOCH PIC

EPOCH [76] is a type of particle-in-cell (PIC) code. EPOCH is an adaptable multi-dimensional kinetic based code that considers plasma to be made of macroparticles with their own set of variables which influence one another and effect the plasma as a whole [76]. Kinetic models are more realistic to what we understand to be physically occurring within plasmas, but require higher computational power and time as a result. The PIC kinetic algorithmic process is summarised in Figure 3.4. The user initiates the simulation by communicating the initial conditions via an input deck. This input deck includes details of the simulation duration, time-steps, laser pulse parameters, target material, properties and dimensions. In the simulation results discussed in this thesis, the input deck has parameters as close to the experiment as computationally possible, and EPOCH was ran in 2D only.

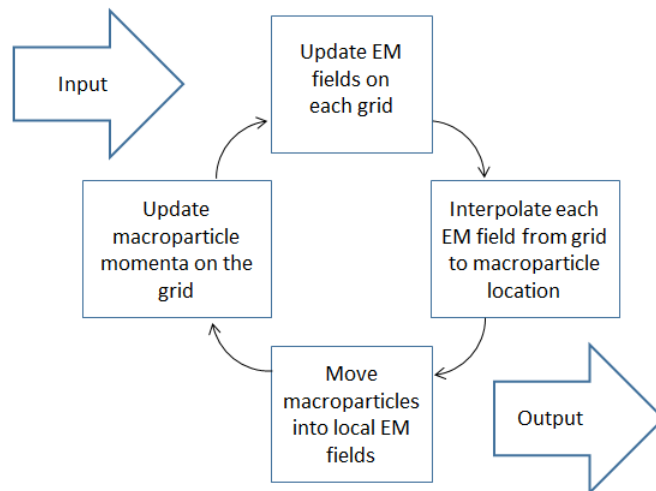


FIGURE 3.4 – Flow chart of the kinetic PIC process from input to output.

## THE MULTI-CHANNEL OPTICAL PROBE

In this chapter the multi-channel optical probe and proof of concept results are presented. We begin by unravelling the pathway that was taken in the development of the new diagnostic from the sources of inspiration to concept, to optical design and set-up. We will explore the motivation behind the development of the multi-channel probe, and the reported findings to date that have highlighted the need for a new method, such as this, to measure the evolving density structures within a single laser pulse interaction with plasma. In the results and discussion that follows, we demonstrate that single shot shadowgraphy of a laser-plasma interaction at one point in time is not sufficient for characterising the propagation and plasma dynamics, due to their transient and complex nature. To improve upon this current practice, the multi-channel probe was developed and offers a reliable means to gain a deeper insight into the evolving interaction dynamics by making measurements at 4 or more time steps – which has otherwise only been approximated based on simulations of the interaction physics.

## 4.1 TEMPORALLY RESOLVED IMAGING AND LASER-PLASMA INTERACTIONS

Temporally resolved imaging is by no means a new area of interest, and the applications span far beyond the field of laser-plasma physics. However, as laser pulses became shorter to achieve greater pulse power for higher on-shot intensity, temporally imaging the ever faster evolving dynamics continues to pose a challenge. With new multi-PW laser facilities, such as Extreme Light Infrastructure (ELI), now operating relativistic laser pulses over femto-second timescales, the development of diagnostics able to keep up and provide the temporal resolution required to fully characterise the ultra-fast dynamics yet to be uncovered in these unexplored higher intensity regimes, has never been more important. Until recently, the resolution achievable is insufficient when compared to the resolution desired. Results from the laser-plasma community continue to demonstrate the need for robust temporal resolving diagnostics to gain a better understanding of the evolution of newly discovered phenomena, behaviours and dynamics. Therefore, the growing interest and potential impact of this technique spans across the entire laser-plasma community.

This section reflects on the milestones in temporal imaging that has brought us to where we are now. Today, pump-probe is a standard technique used in laser-plasma physics and in a range of areas where ultra-fast imaging is required. The pump-probe approach to illuminate instant reactions was invented by August Toepler in 1864 who used persistence of vision to memorise and depict a blast from an electric spark while illuminating the event with a second spark. It is from this that the pump-probe method currently employed in laser-plasma physics was built upon. Similarly, Eadweard Muybridge in 1877 was the first to capture multiple images

from an array of cameras observing the evolution of a horses' gallop on film that could be reconstructed into a movie using his device named the Zoopraxiscope. This breakthrough marked the beginning of temporal imaging within a single event, and also became a classic example in demonstrating the value that temporal imaging has by revealing new information that is critical to understanding any evolving process. With the invention of the laser in 1960 [12], sparks and stroboscopic light sources were replaced in temporal imaging set-ups by short-pulse laser light. Shortly following this, in 1969, the invention of CCD cameras replaced film, which expanded the possibilities for temporal imaging ultra-fast processes. As a result, scientific research applications requiring high temporal resolution in small scale processes such as femto-chemistry, in-vivo cell biology and plasma physics all advanced. It is the combination of these innovative breakthroughs and the advancement of technology that has inspired and enabled the development of our novel approach—to use multi-channel shadowgraphy to image laser-plasma interactions with picosecond temporal resolution.

Due to laser-plasma interactions offering an accessible route to exotic states of matter, including fusion plasmas [77] and as a compact source of radiation [14], it has been a central aim to experimentally measure the temporal and spatial evolution of the underpinning plasma density and propagation dynamics which drive the interaction they depend on. However, the complex dynamics of these interactions evolve rapidly on timescales less than the laser pulse (femto- to pico-seconds) and are highly sensitive to initial plasma conditions and shot-to-shot variations in the laser pulse parameters [24]. There have been a number of recent results that highlight the sensitivity of the radiation source properties to changes in the laser and plasma parameters within a narrow range [78–80]. By comparing the experimental results to numerical simulations some of these dynamics can be elucidated, however due to limitations in the physical processes that can be included in codes and the use of idealised

input parameters, measurements in the laboratory give the most comprehensive insights. There presently exists a growing need for the development of experimental techniques which enable detailed and controlled investigation with high spatial and temporal resolution in order to better understand the complex evolving laser-plasma dynamics such as self-focusing [81] or the propagation of higher-order modes (such as Laguerre-Gaussian beams) in plasma [82]. Progress in this area will open up a new dimension of experimental measurement and provide additional capability to quantify key factors which limit the control of laser-plasma driven radiation sources.

To date a number of experimental techniques have been developed which seek to address this challenge such as proton probing [83, 84] and the use of a streak camera [85, 86]. Both of these, however, have limitations, in temporal resolution and versatility [87, 88], and spatial dimensionality [89], respectively. Optical probing using a chirped laser pulse [90, 91] has also been investigated to provide the temporal resolution desired, with the dependence on pulse bandwidth, however this approach does not work well for picosecond scale systems and lacks arbitrary control over the temporal resolution.

Complementary to all of these, single pulse optical probing is often used over multiple consecutive shots at varied probe timings in order to construct a temporal series [23]. The method of building a series of single shot shadowgraphs at staggered time intervals over repeated shots, while attempting to maintain constant conditions has been a popular route to measuring the evolution of interactions over very short timescales. However, due to the difficulty in ensuring all other interaction parameters remain fixed this approach can add more uncertainty to our understanding than it resolves. This method is inherently susceptible to changes in the interaction dynamics due to shot-to-shot variations in the laser and plasma conditions [25–28], including changes in the laser spatial profile, energy and spectrum. This issue can be

compounded by the fact that many large laser systems have low shot rates and low output stability, and therefore poor statistics with which to minimise the impact of shot-to-shot fluctuation on measurements [25]. This is a critical limitation highlighted as motivation for the development of alternative temporal measurement techniques, such as the multi-channel probe [31] and time-sequence imaging by two-colour probe [92].

## 4.2 MULTI-CHANNEL PROBE DESIGN

The multi-channel probe is a pump-probe system, that measures the temporal evolution of a single laser pulse interaction by imaging the same field of view at four varied time frames, via four probe lines. The fundamental principle of this new approach derives from the established wavelength and polarisation division multiplexing techniques which have been used widely, primarily, in telecommunications for decades [93]. This concept is adapted and implemented into a design that is appropriate for a pump-probe arrangement in a high power laser-plasma interaction environment.

A process flow diagram of the optical probe system is shown in Fig. 4.1, which is a culmination of the classic pump-probe concept from August Toepler, multiple imaging via camera array systems from Eadweard Muybridge, and the encoding of laser pulses inspired by multiplexing methods in telecommunication systems. The multi-channel optical probe system consists of one input channel and four temporally separated and encoded output channels which enables four separate images (via interferometry or shadowgraphy) to be taken of the same spatial location, with independent timing control. The multi-channel probe consists of six main parts: the pulse generator, encoding, delay control, multiplexer, demultiplexer, and the imaging system. The

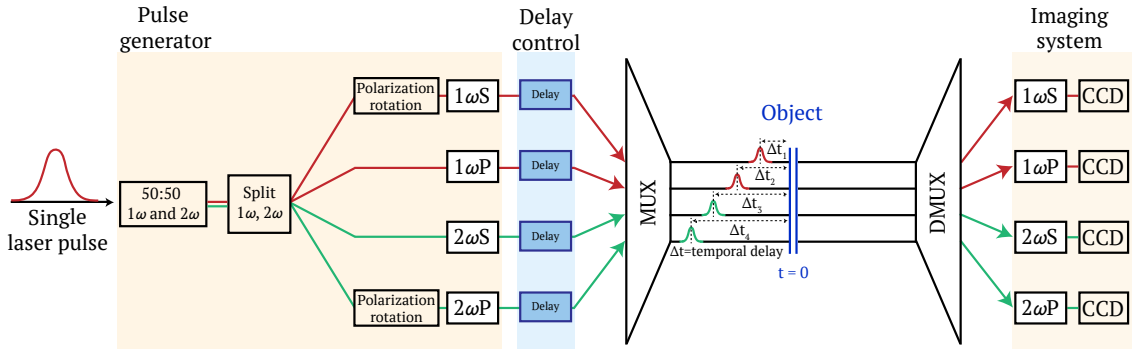


FIGURE 4.1 – Process flow diagram of multiplexed optical probe concept. A single ultrashort laser pulse is divided into four separate laser pulses which are uniquely encoded by frequency and polarisation. The four pulses are independently delayed in time and then spatially multiplexed (MUX) to propagate co-linearly in order to optically probe a given point in space and time. The inverse process (DMUX) is then applied to spatially separate and form an image for each of the channels. This enables 2D spatial and picosecond temporal resolution over multiple frames with a single laser pulse.

pulse generator is where four individual pulses are generated from an initial single seed probe pulse. The encoder then assigns an identifiable wavelength and polarisation key to each pulse so they can be easily distinguished. The delay control station adds additional path lengths, specified by the user, to each probe line to achieve the desired time delay ( $\Delta t$ ). The multiplexer is where the separate encoded pulses can be made co-linear to ensure the probe system maintains a fixed field of view when incident on the object. The demultiplexer then spatially separates the four pulses (using the identifiable wavelength and polarisation keys) into individual imaging set-ups. The imaging system consists of focusing lenses and an individual CCD camera per probe channel to maximise image resolution.

A detailed technical schematic of the optical system design for use on a high power laser experiment is shown in Fig. 4.2. By splitting the initial P-polarised pulse in two, one output can be frequency doubled by passing it through a  $\beta$ -Barium Borate (BBO) crystal of 50% conversion efficiency. This generates  $1\omega$  (1054 nm) and  $2\omega$  (527

nm) channels which can both be divided again by a beamsplitter (BS), after which one of each harmonic is passed through a half wave-plate to give a  $90^\circ$  polarisation rotation, to produce  $1\omega_S$  and  $2\omega_S$ . The final result is four laser pulses (henceforth referred to as  $1\omega_S$ ,  $1\omega_P$ ,  $2\omega_S$  and  $2\omega_P$ ) with uniquely distinguishable combinations of wavelength and polarisation. To enable independent timing control of each of the laser pulses a time delay slide is included along each beam path. A time delay stage consists of two mirrors positioned 90 degrees to one another attached to a motorised platform so that the path length to the mirrors can be extended or reduced as the motorised platform moves. A change of 1 cm to the path length translates to a 33.3 ps change to the arrival of the probe pulse. The individual delay stages facilitate both fine and coarse control of the intervals between imaging, providing flexibility to observe developments at arbitrary timesteps over a few picoseconds and at later stages of the remnants of the interaction with larger steps of hundreds of picoseconds.

After the timing stages, the four encoded pulses are made co-linear using a *multiplexer* arrangement. The  $1\omega_S$  and  $1\omega_P$  pulses are spatially overlapped using a polarising beamsplitter (PBS). These two pulses are then spatially overlapped with the  $2\omega_S$  pulse via a  $1\omega/2\omega$  dichroic beamsplitter (DBS). The final optic in the system for recombining is a non-polarising beam splitter (BS) which enables the  $2\omega_P$  pulse to overlap with the other pulses. The co-linear, temporally separated pulses are then directed transversely, across the interaction of an intense laser pulse with a plasma, as a single optical probe line. The transmitted probe light is then directed to the *demultiplexer*, external to the vacuum chamber, where the co-linear probe pulses are spatially split into four separate channels. Here the demultiplexer consists of a dichroic beamsplitter and a pair of polarising beamsplitters which enables the pulses to be split by wavelength and then by polarisation, spatially separating the four individual pulses by their encoded keys.

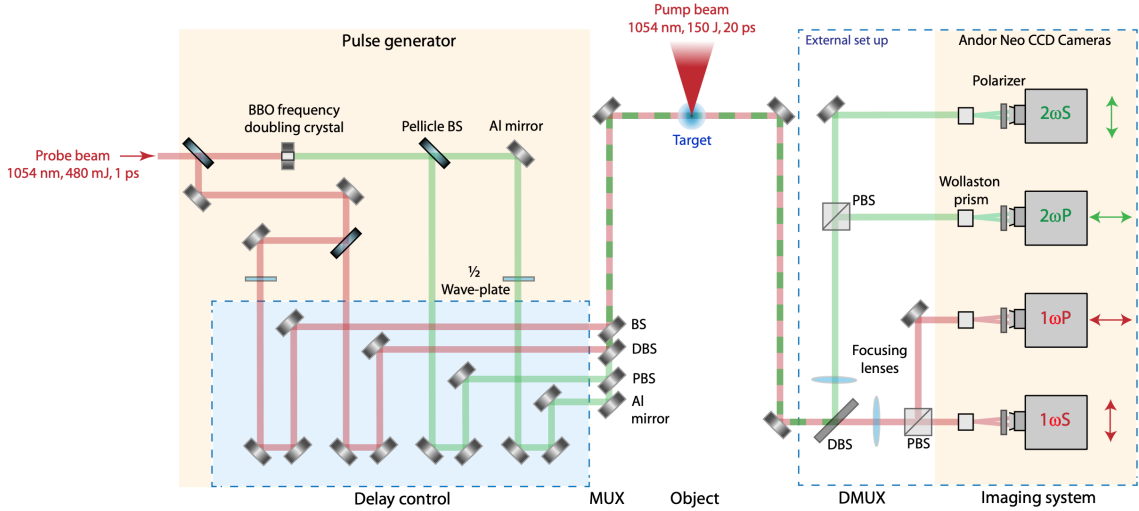


FIGURE 4.2 – Schematic of the experimental set up within the vacuum chamber where a high power pump laser pulse is focused into a gas target and a low-intensity probe pulse is passed through the internal multi-channel system and the demultiplex arrangement external to the chamber. The diagram details the optical system used in the multi-channel probe to generate the four uniquely encoded laser pulses, delay them in time, spatially multiplex and then demultiplex after the interaction point (object) to image the individual channels.

The initial design of the imaging system consists of a Normarski-type interferometer [21] by passing each pulse through a Wollaston prism and a polariser to produce an interference pattern [22]. Each of the channels is then imaged into a separate Andor Neo sCMOS camera. The use of interferometry is intended to give a direct time resolved measurement of the evolving plasma electron density [94]. The multi-channel probe system can be adapted for both interferometry and shadowgraphy.

In designing the optical set-up important considerations had to be made to ensure the spatial and temporal resolution desired were optically achievable. To minimise energy loss, the number of optics that each probe pulse was to travel through was reduced. This consideration also included configuring the order of optics that splits the probe pulse energy as equally as possible between each of the 4 probe channels, while keeping the set-up compact. To ensure the spatial information between the channels

were not easily exchanged, hence disrupting the temporal resolution, polarisation and wavelength encoding parameters were chosen that were not closely related. This is a limiting factor in extending the multi-channel encoding concept beyond four channels, as quarter wave-plates and third harmonics would diminish the clarity between, and imaging quality of, the probe channels.

### 4.3 PROOF OF CONCEPT

The new optical probing technique was first tested in an intense laser-plasma interaction experiment. The multi-channel optical probe enables direct measurement of the propagation of a relativistically intense laser pulse in a high density sub-critical [95] plasma medium during a single pump pulse interaction. The experiment was performed at the Rutherford Appleton Laboratory, Oxfordshire, UK, using the Vulcan Nd:Glass laser system in a dual short pulse beam configuration - one used for the interaction and other for the probe. The probe beam used was picked off from the 20 cm diameter probe beam with a total energy of  $\approx 30$  J and a pulse duration of  $\approx 1$  ps. The resultant picked off probe beam was 2.54 cm in diameter with 480 mJ total energy.

The intense laser plasma interaction was driven by a 1054 nm laser with 150 J pulse energy and 20 ps duration at full width at half maximum (FWHM). The laser pulse was focused to  $\approx 5.6 \mu\text{m}$  (FWHM) using an F/3 off-axis parabola, reaching a peak intensity of  $\approx 1 \times 10^{18} \text{ W/cm}^2$ . The laser pulse was focused to the centre of a helium gas jet target, which was operated at pressures of up to 100 bar, reaching electron densities of up to  $1 \times 10^{20} \text{ cm}^{-3}$  ( $0.1 n_c$  [95]).

The optical probe was timed relative to this high intensity laser pulse using a streak camera, as described in Chapter 2. Although the streak camera could reach

sub-2 ps temporal resolution, the timing resolution between the optical probe and the high intensity pulse was found to be  $\approx \pm 10$  ps. This was due to jitter in the electrical signal used to trigger the streak camera. The time delay for each pulse was adjusted using a time delay slide which had 2 ns (60 cm) maximum range of motion in a double pass configuration. A magnescape encoder was used with a position accuracy of  $\approx 10 \mu\text{m}$  ( $\approx 30$  fs). Initially all four optical probe pulses were overlapped in time with the high intensity pulse and then moved in time to provide measurements at defined points in time during the interaction. As shown in Fig. 4.2, a combination of transmissive and reflective optics were used, after the time delay system, to achieve spatial overlap between the four pulses. This process resulted in significant energy losses in some of the channels. The transmission through the multiplexer was calculated to be  $0.125E_t$  ( $1\omega\text{S}$ ),  $0.25E_t$  ( $1\omega\text{P}$ ),  $0.06E_t$  ( $2\omega\text{S}$ ), and  $0.06E_t$  ( $2\omega\text{P}$ ), where  $E_t$  is total input laser energy of the initial single probe pulse.

After the optical probe passed through the plasma and the individual pulses were spatially separated in the *demultiplexer* system, the remaining sections of the optical probe were set up to act as a Normarski-type interferometer for each of the pulses. Although interferometry was tested and demonstrated to work during the experiment, the reduction in signal caused by the introduction of a polariser and Wollaston prism was found to reduce the signal-to-noise ratio, noise being predominantly self-emission, to an unacceptable level during high power laser shots. In future set-ups the temporal gating of the CCDs could be reduced to minimise the contributions from self-emission. The data and analysis presented in the following sections is therefore limited to shadowgraphy measurements only. The field of view of the optical probe imaging system was  $\approx 0.6 \text{ mm} \times 0.5 \text{ mm}$  with a resolution of  $\approx 7 \mu\text{m}$  at  $1\omega$  and  $\approx 3.5 \mu\text{m}$  at  $2\omega$ , in both dimensions, and magnification of  $\approx 29$ , for each of the channels.

Fig. 4.3(a)–4.3(d) shows example measurements of the interaction of the intense laser pulse with a helium gas target at a gas pressure of  $P = 99.7, 98.1, 95.1$  and  $41.1$  bar respectively. From left to right in Fig. 4.3, each of the separate output channels of the probe are shown for fixed timings relative to the peak of the laser of  $t = 0, 12, 167$  and  $217$  ps, respectively. In these images the temporal evolution of a laser-driven plasma channel is clearly observed. The formation of such a channel is expected around the focal region due to the time-averaged ponderomotive force [36, 96], which acts to accelerate electrons away from regions of locally high intensity [23, 36]. This depletion of electrons from the focal region results in an intensity dependent change in the refractive index [97]. For the approximately Gaussian focal spot distribution used in this experiment, the wings of the spatial-intensity profile of the laser propagate faster in the plasma than the intense centre due to the higher electron density at edges of the channel, resulting in a rapid self-focusing of the beam [81]. The peak laser intensity in this experiment is only slightly above the  $1.24 \times 10^{18}$  W/cm<sup>2</sup> relativistic threshold for the  $1.054 \mu\text{m}$  wavelength used here. In this regard, the plasma electron Lorentz factor is close to unity and so we expect ponderomotive self-focusing effects to dominate at early times. However, given sufficient ponderomotive self-focusing, relativistic effects could play a role near the peak of the pulse [81].

The most salient point to be taken from these proof of concept measurements is the observed variability in the channel evolution due to the large dependence on initial conditions, despite there being only small fluctuations in the laser and gas target parameters. Across the three examples of repeated laser shots Fig. 4.3(a)–4.3(c) the average gas pressure is  $(98 \pm 2)$  bar ( $\pm 2\%$ ) and the average laser energy is  $(158 \pm 5)$  J ( $\pm 3\%$ ). In this range we observe the early evolution of the channel to change substantially. While in all cases there is a small region of plasma which forms at early times and then rapidly evolves into a full channel within 12 ps, in Fig.

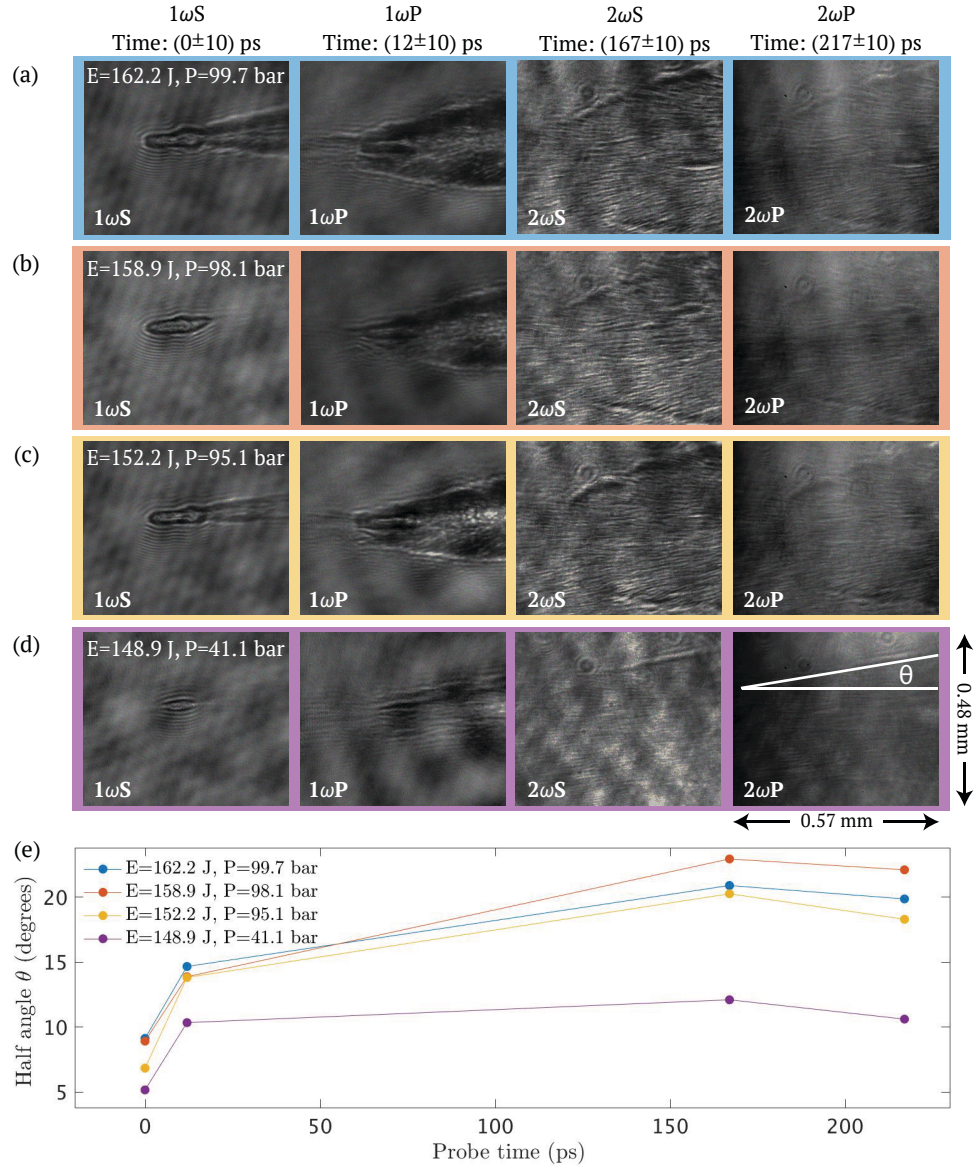


FIGURE 4.3 – Shadowgraphy measurements of each probe output channel from the experiment for (a)  $E = 162.2$  J,  $P = 99.7$  bar (b)  $E = 158.9$  J,  $P = 98.1$  bar (c)  $E = 152.2$  J,  $P = 95.1$  bar, and (d)  $E = 148.9$  J,  $P = 41.1$  bar. (e) Averaged half-angle divergence of the plasma channel wall evolving at 0, 12, 167 and 217 ps measured directly from the sets of images (a)–(d).

4.3(a) and 4.3(c) we observe an earlier onset of the full channel. This variation in the channel growth does not appear correlated with higher laser energy and plasma density alone, as in Fig. 4.3(c) both of these parameters are lower than in 4.3(b)

where the early onset of the channel is not observed in the  $1\omega\text{S}$  measurements. This earlier onset of the channel formation will induce self-focusing and, at these densities, beam collapse [96].

In the  $1\omega\text{P}$  measurements ( $t = 12$  ps), a larger degree of filamentation is clearly observed for Fig. 4.3(a) and 4.3(c) where the channel formation occurred earliest. This early time channel evolution is induced by small random variations in the laser - such as an additional prepulse - or plasma parameters, and is a quintessential example of the utility that the multi-channel optical probe can provide. In a standard single channel optical probe arrangement the temporal dynamics are extracted over consecutive repeated laser shots, where it is difficult to differentiate the evolution of the plasma dynamics from random fluctuations in the initial conditions. Relying on repeated laser shots to build a timing scan would be similar to piecing together  $1\omega\text{S}$  from (a),  $1\omega\text{P}$  from (b) and  $2\omega\text{S}$  from (c).

The measurements for the later channels show a stagnation of the channel evolution for  $t \geq 150$  ps. This is because, as well as the laser field no longer being present to interact with the plasma, the plasma temperature will be decreasing with time and dispersion will be slowing. The electrostatic force between the electrons within the channel walls and the ion cloud which is left in the centre, will push the channel walls outward. This effect will be to stagnate as the force weakens in time as the channel disperses. The  $2\omega\text{S}$  and  $2\omega\text{P}$  channels both suffer poor signal-to-noise ratio due to the presence of self-emission in the plasma which provides a source of noise in the image. The stagnation in the evolution of the channel is clearly observed in Fig. 4.3(e) where at early time the channel half angle is shown to grow rapidly then saturate on time scales longer than the laser pulse duration. The half-angle  $\theta$  is measured as defined in Fig. 4.3(d), overlaid on the the  $2\omega\text{P}$  channel. The initial half-angle of the channel shown in Fig. 4.3(a)–4.3(c) is approximately  $10^\circ$ , which is

expected for the F/3 focusing geometry used in this experiment and suggests that limited ponderomotive self-focusing has occurred early in the interaction. Later in the interaction for  $t \geq 12$  ps the half-angle of the channel has increased up to near  $15^\circ$  which is approaching an F/2 focusing geometry, induced by self-focusing of the laser pulse. The measurements at late time show an even steeper profile which is approaching an F/1 focusing geometry, which has then saturated by the final time step. This is also explained by the drifting in channel walls due to electrostatic force from the ion cloud. In addition to the images shown in Fig. 4.3(a)–4.3(c), this measurement is also made, for comparison, for  $P = 41.1$  bar and  $E = 148.9$  J in Fig. 4.3(d) and the evolution is quite different. At early times breakdown of the background gas is observed but the full channel has not yet formed. For  $t \geq 12$  ps a channel is present with a half-angle which approaches the initial F/3 geometry and remains approximately constant for the succeeding time steps.

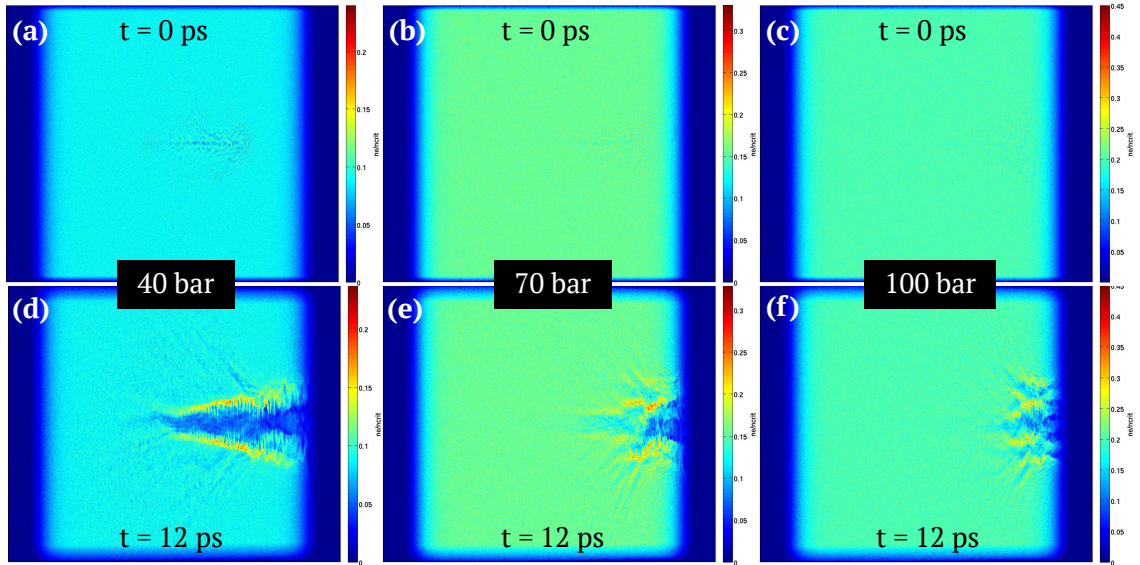


FIGURE 4.4 – Electron density plots from three 2D PIC simulations with helium gas pressures 40 bar in (a) and (d), 70 bar (b) and (e), and 100 bar in (c) and (f), sampled at time frames 0 ps and 12 ps - similar to the probe delay timings. Where the colour bar represents the electron density normalised to the critical density.

For comparison to the experimental proof of concept results, a series of three 2D PIC simulations were performed for a laser pulse with fixed peak intensity propagating in a range of helium gas pressures (40, 70 and 100 bar). As shown in Fig. 4.4, each simulation was sampled at two time frames, 0 ps and 12 ps, matching that of the earliest two channel timings from the multi-channel probe experimental set-up ( $1\omega_S$  and  $1\omega_P$ ). In Fig. 4.4 (a)–(c) at 0 ps, there is little to no evidence of the early onset of a channel forming, unlike the shadowgraphs measured experimentally in Fig. 4.3  $1\omega_S$  column for similar gas pressures. In Fig. 4.4 (d)–(f) at 12 ps, the channel has formed but the degree of filamentation and propagation depth varies with gas pressure. The depth of propagation decreases with increasing gas pressure, while the degree of beam break-up and filamentation increases with gas pressure. This is contrasting with the measurements shown in Fig. 4.3, where filamentation is maximised for the lowest pressure of 41.1 bar in  $1\omega_P$  (d), whereas at the lowest pressure of 40 bar in Fig. 4.4

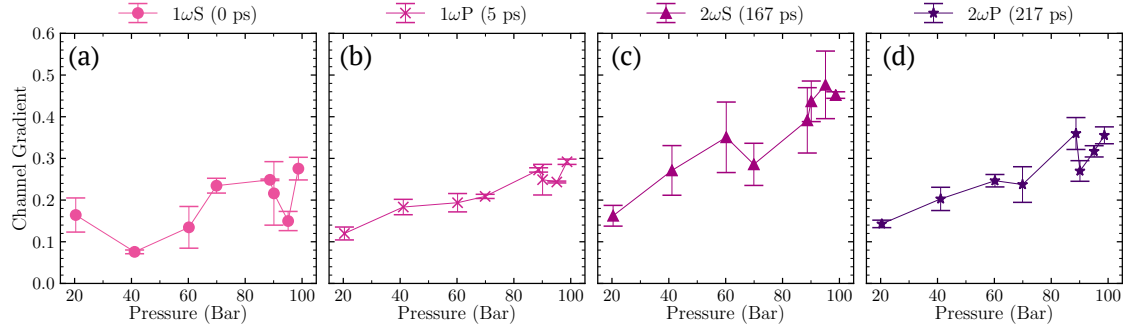


FIGURE 4.5 – The average channel gradient as a function of increasing pressure at probe timings: (a)  $1\omega S$  0 ps, (b)  $1\omega P$  12 ps, (c)  $2\omega S$  167 ps, and (d)  $2\omega P$  217 ps.

(d), filamentation is minimised most. The depth of propagation does not change with pressure in the experimental measurements, although some beam break-up may have occurred at the higher gas pressures as shown in Fig. 4.3 (a)–(c). The main conclusion from this simple comparison is that conceptually, it has been shown that the multi-channel probe provides deeper insight into the evolving dynamics at this resolution compared to both simulations and the method of building a temporal scan via repeated shots (without reproducible conditions). Simulations cannot capture the realistic fluctuations in laser pulse and prepulse parameters which have been shown to change the initial conditions and subsequently effect the seeding of instabilities.

Following the proof of concept, the experimental campaign continued exploring the temporal behaviour measured over a finer range of gas pressures in otherwise fixed laser pulse parameters. Similar to the proof of concept, the laser energy was maintained at  $(150 \pm 5)$  J and with the point of focus set 2.8 cm above the gas jet. The pressure was varied from 11 - 100 bar, with the probe timings fixed at 0 ps ( $1\omega S$ ), 12 ps ( $1\omega P$ ), 167 ps ( $2\omega S$ ), and 217 ps ( $2\omega P$ ). However, the pressure scan reported in Fig. 4.5 includes only the laser interactions with gas pressured of 20 - 100 bar, as the interaction with the gas at the lowest pressure did not provide clear enough plasma density channel structures to measure due to the low electron density. Fig. 4.5

presents the average of 3 repeated measurements of the upper channel gradient across the four channels (a) 0 ps ( $1\omega\text{S}$ ), (b) 12 ps ( $1\omega\text{P}$ ), (c) 167 ps ( $2\omega\text{S}$ ), and (d) 217 ps ( $2\omega\text{P}$ ) as a function of increasing pressure. The channel gradient was calculated in a simple image analysis GUI written in Python which took two user-defined points and calculated the gradient between them. The GUI repeated this process for each image five times and calculated a mean gradient and standard deviation as the error for each image. At all four timings, the channel gradient increases with increasing gas pressure - likely due to the higher electron density build up at the wings of the laser pulse causing a stronger degree of self-focusing. Over the earliest three timings (a)-(c) the channel gradients for all pressures generally increase with time, however at the latest probe timing (d) the channel gradient have reduced. This is expected because after the peak of the laser pulse, the remaining channel structure will continue to disperse over time. The key insight that the multi-channel probe provides is the temporal change in structure - and in this experiment - the change in channel gradient ( $\Delta m$ ) as a measure of the degree of self-focusing. Fig. 4.6 shows the increase in channel gradient measured over 155 ps in the pressure scan between two probe channels  $1\omega\text{P}$  -  $2\omega\text{S}$ . It is within this window of time that the peak of the pulse and channel gradient will have been maximised. By calculating the difference in channel gradient for all pressures, we can see that the change in gradient also increases with gas pressure. This data suggests that not only does the channel gradient correlate with increasing pressure, but the rate in which the gradient steepens also increases with pressure - an insight that would not have been possible without the application of the multi-channel probe.

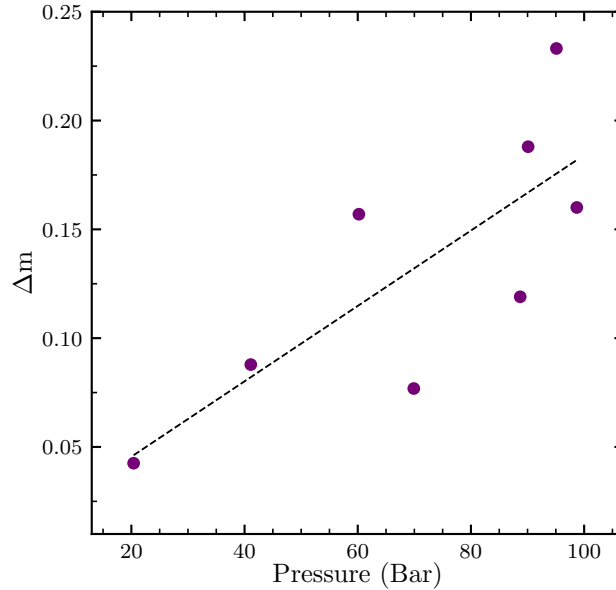


FIGURE 4.6 – The change in channel gradient over 155 ps (measured between probes  $1\omega_P - 2\omega_S$ ) as a function of increasing pressure.

#### 4.4 SUMMARY AND CONCLUSIONS

A multi-channel optical probe capable of both 2D spatial resolution and picosecond-scale temporal resolution of a single laser pulse-plasma interaction has been developed. The proof of concept results highlight the importance of reproducible conditions to ensure reliability, especially when measurements are reconstructed from a series of consecutive shots. Example experimental results demonstrate the utility of this approach, where random fluctuations in the laser and plasma parameters on the order of a few percent have been observed to modify the plasma channel evolution substantially and therefore the laser-pulse propagation dynamics. This highlights the need to employ single-shot time-resolved measurements in order to clearly deconvolve random fluctuations in experiment parameters from changes in the plasma dynamics. Equivalent estimations cannot be made using a conventional single time frame optical probe approach or simulations alone. The application of the multi-channel optical

probe to the pressure scan demonstrates the additional insight and understanding that the new diagnostic can offer. Future development of this approach will open up single-shot electron density evolution measurements via time-resolved interferometry and higher temporal resolution by modifying the system to be appropriate for femtosecond-scale laser pulses. The development of this system represents the capability in the field to make controlled and precise time-resolved measurements of intense laser-plasma interactions. This will enable new insight into the underpinning physics which drive, for example, laser-driven radiation sources and which previously could not be measured experimentally during a single interaction.

## THE MULTI-CHANNEL OPTICAL PROBE & FRONT SURFACE PLASMA DYNAMICS

In this chapter the multi-channel probe, reported in Chapter 4, is utilised in an experiment to explore the impact that different methods of laser intensity control have on the expanding front surface dynamics in an intense laser–solid interaction. As detailed in Chapter 2, intensity is typically controlled by variation of three key variables, laser input energy, focal spot size, and pulse duration. If measured correctly, a combination of these variables will, by definition, deliver the desired on-shot intensity. However, the results that follow suggest that the method in which the intensity is controlled (via different combinations of laser energy, focal spot size and pulse duration) alters the initial conditions preceding the main pulse and impacting upon the pre-plasma dynamics, which in some instances enhances the actual on-shot intensity. Since intensity is the key parameter that enables access to new regimes within light–matter interactions, control of this is fundamental. This argument is based on the comparison of experimental results between varying input laser energy and by defocus position in otherwise constant conditions, measured from single-shot

temporally resolved multi-channel shadowgraphy, RCF, back-scatter spectra, and supported by 2D EPOCH particle-in-cell simulations.

## 5.1 EXPERIMENTAL METHODS

The experiment was conducted at Rutherford Appleton Laboratory, using the Vulcan laser system in the Target Area West (TAW) operating area. As described in Chapter 3, the short pulse beamlines of Vulcan operates via two beamlines both 1054 nm in wavelength, delivering p-polarised light. In this experiment, the beamlines operate in pump-probe configuration with pulse durations (FWHM) of 20 ps (pump) and 1 ps (probe). The pump pulse delivers peak intensities up to mid  $10^{19}$  W/cm<sup>2</sup> at an angle of incidence of 25.5° to target normal. The target is 20  $\mu$ m thick copper, of 3 mm  $\times$  6 mm dimensions. The laser energy throughput of the main pump beamline was measured to be 38.7% from calorimetry measurements, taken before passing through chamber optics, and 32%–45% from the encircled energy depending on the half-width at half-max for the range of defocus positions. At best focus, a focal spot of 5.55  $\mu$ m diameter is achieved using a F3 focusing parabola.

Central to this experiment are the two laser intensity scans conducted via different methods of intensity control. The first is the laser input energy scan, consisting of four shots, ranging from 20 to 247.6 J with the target positioned at best focus, and spot diameter of 5.55  $\mu$ m. The second is the defocus scan, consisting of seven shots, where the spot diameter is varied from 5.55 to 65  $\mu$ m (FWHM) by defocusing  $\pm 500$   $\mu$ m either side of best focus at fixed laser input energy of 150 J. A positive defocus position is when the off-axis parabola is driven towards the target which shifts the best focus position beyond the target. In this case, the interaction is said to take place "before focus". Similarly, a negative defocus is when the off-axis parabola is

driven back, away from the target, which brings the laser pulse to focus in front of the target. In a negative defocus, the part of the laser pulse that interacts with the target is therefore said to be "after focus". A diagram depicting best focus, before focus and after focus is shown in Figure 5.1. The on-shot intensity is calculated for both

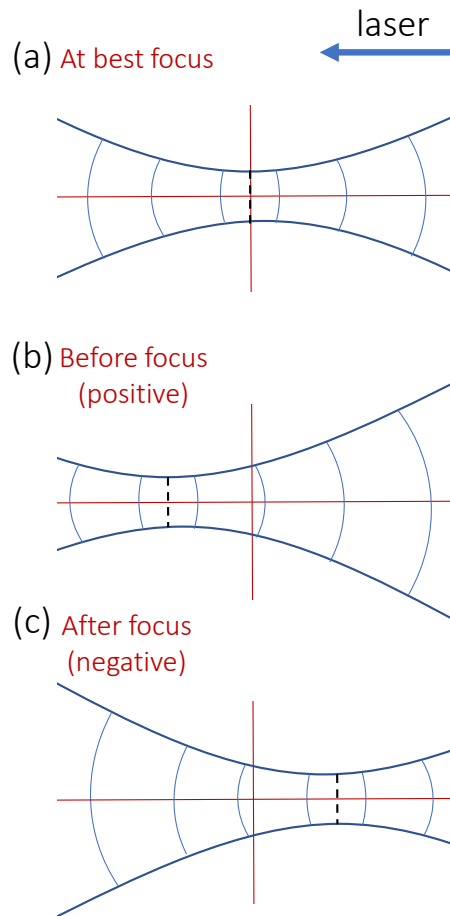


FIGURE 5.1 – Diagram of the incoming laser pulse best focus position (represented by a black dashed line) relative to the target position (represented by the red cross hairs) and the changing wavefront shape either side of best focus. (a) The target is at the best focus position; (b) the target is before focus as the laser pulse is positively defocused; and (c) the target is positioned after focus as the laser pulse is negatively defocused.

intensity scans dividing the peak power, calculated from the on-shot pulse energy and pulse duration, by the focal spot area. The focal spot sizes are measured using a focal spot camera in vacuum with a low power beam over the same target positions ( $\pm 500 \mu\text{m}$  either side of best focus). The main feature diagnostic in this experiment is the application of the multi-channel probe. The two-dimensional spatial, temporal measurements presented of the evolving target front surface and plasma expansion within a single interaction are the first optical measurements of their kind. One of the key advantages to implementing the multi-channel probe in this comparative study is that we mitigate the impact of shot-to-shot variations, as discussed in Chapter 4, that previously hindered comparison attempts where the profiles of expanding plasma were primarily constructed from a series of repeated shots [98]. The probe system has the same set-up as described in Chapter 4, with three shadowgraphy channels and one interferometry channel. As before, the probe channels are labeled as  $1\omega\text{P}$ ,  $1\omega\text{S}$ ,  $2\omega\text{P}$ , and  $2\omega\text{S}$ .

For both intensity scans, the probe channels are fixed at four distinct time frames -183 ps, -3 ps, 117 ps, 417 ps (relative to the peak of the pulse at best focus) to provide clear comparisons of 2D images of the plasma profile before, during and after the main pulse has interacted with the target. As noted in the last chapter, the field of view of the channels are  $0.57 \text{ mm} \times 0.48 \text{ mm}$ , with a resolution of  $7 \mu\text{m}$  at  $1\omega\text{P}$  and  $1\omega\text{S}$ , and  $3.5 \mu\text{m}$  at  $2\omega\text{P}$  and  $2\omega\text{S}$ , with a magnification of 29 for each probe line. For post processing purposes, multiple scripts of code were developed to rotate, translate, align and crop the series of images to hone in on the areas of interest prior to comparison and characterisation measurements. A contour tracing script was developed to use after post processing for the user to outline and measure the varying profiles of the front surface plasma for each channel across both intensity scans. It presented each image within a GUI and allowed unlimited anchor points for

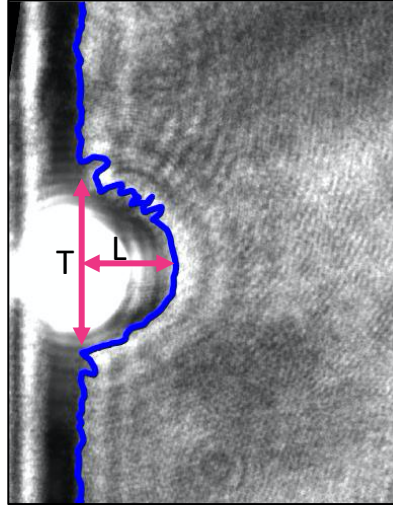


FIGURE 5.2 – An example shadowgraph image of the target front surface plasma expansion profile outlined with a contour line in blue, and characterised by longitudinal (L) and transverse (T) measurements.

the user to place on the front surface. The script then interpolated between these points to build a profile. The contours provided a clearer interface to measure the extent of the expanding plasma on the front surface at various points in time. An example of the quality of contour typically extracted, and the size of transverse and longitudinal plasma expansion measurements are shown in Figure 5.2 (a) and (b), respectively. From this, the rate of plasma expansion on picosecond timescales can be calculated. This was only a semi-automated process due to diverse plasma profiles and light levels due to self-emission making thresholding challenging. Development of a fully automated approach would be beneficial for future experiments due to the high volume of image analysis required.

To investigate the influence of the two difference intensity control methods on the acceleration of ions, an RCF stack is used as discussed in Chapter 2. The RCF stack is positioned behind the target along the target normal axis, in the direction of the highest energy accelerated ions, as shown in Figure 5.3(a). From this we can

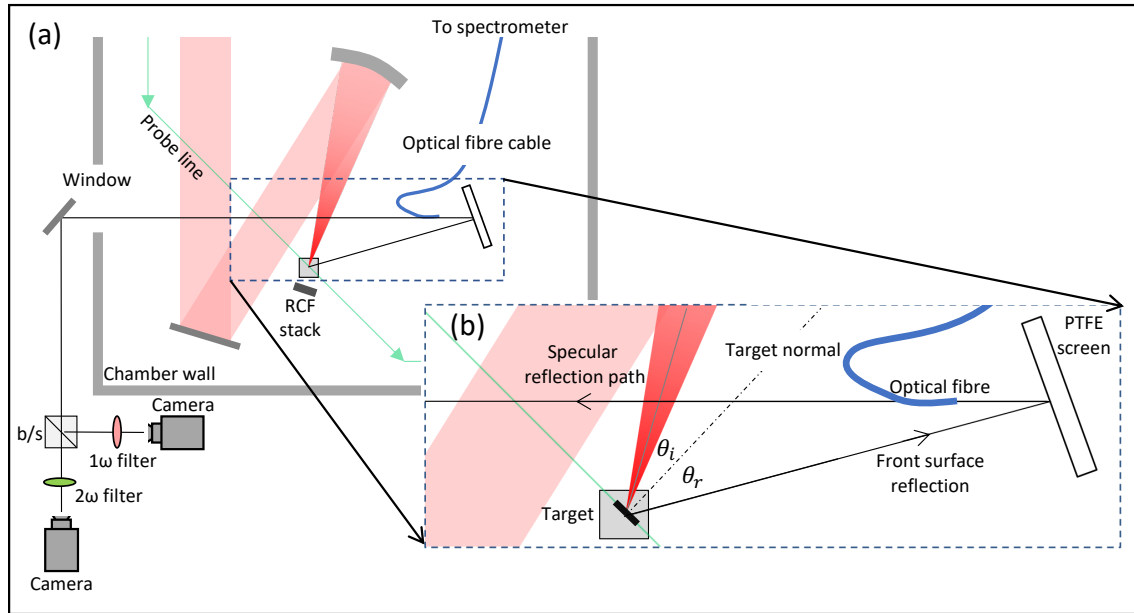


FIGURE 5.3 – Schematic of the full specular reflection path from the target front surface and RCF stack positioning in (a), and a detailed zoomed-in diagram of the specular path with respect to the target normal, and the spectrometer optical fibre placement in front of the PTFE screen, in (b).

compare maximum proton energies, over a range of nominal on-shot intensities, in both the laser energy scan and defocus scan.

In addition to these diagnostics, an Ocean Optics spectrometer was used to measure the spectrum of the specular light reflected from the target front surface, and onto a PTFE screen. The specular set-up is shown in Figure 5.3(b). The light is measured via an optical fibre in line with the angle of reflection from the PTFE screen, which is then directed out of the chamber via a patch panel and into the spectrometer. The Doppler shift in the measured reflected pulse compared with the input pulse can give an indication of the velocity of the evolving critical surface. This can be linked to the rate of plasma expansion, or compression (hole-boring velocity), due to the Doppler effect — as light is reflected from a moving surface. The following equation introduced by Wilks [99] represents the balancing of the mass

flow momentum flux (expansion) with the radiation light pressure (compression):

$$n_i m_i v_f^2 = \frac{I}{c} \quad (5.1)$$

where  $n_i$  is the ion density,  $m_i$  is the ion mass,  $v_f$  is the ion front velocity,  $I$  is the intensity and  $c$  is the speed of light. Substituting the hole-boring velocities, measured from the red-shifted reflected light into this equation provides an additional estimate of intensity for comparison to the nominally calculated, and TNSA estimated. This can be estimated for both data scans from the degree of Doppler shift in peak wavelengths, from reflection at both  $1\omega_L$  (1054 nm) and  $2\omega_L$  (527 nm) critical density surfaces. A script is developed to process the raw spectrometer data, identify the peak wavelength and the cut-off wavelength of the most red-shifted signal to input into the hole-boring velocity equation 5.1.

The experimental results presented in the next section of this chapter are supported by 1D HELIOS and 2D EPOCH simulations, that are shown later in section 5.3. The 1D Lagrangian radiation-hydrodynamic simulation code HELIOS is used to model two density profiles of the plasma expansion at the front target surface for maximum and minimum experimentally measured intensities,  $1.8 \times 10^{16}$  W/cm<sup>2</sup> and  $6.6 \times 10^{18}$  W/cm<sup>2</sup>, with  $10^6$  contrast level. The HELIOS simulations are run for 1 ns and the density profile is extracted at the end of the simulation. The plasma scale length,  $L$ , is calculated as the inverse of the expansion gradient,

$$n_e(x) = n_0 \exp\left(-\frac{x}{L}\right) \quad (5.2)$$

$$\log(n_e) = -\frac{1}{L}x + \log(n_0) \quad (5.3)$$

where  $n_e(x)$  is the electron density at a position  $x$  perpendicular outward from the

target surface,  $n_0$  is the initial electron density. The plasma scale length  $L$  can then be input into 2D EPOCH for a series of simulations to add to the comparative study of intensity effects when varied by: laser energy for fixed focal spot size, and defocus position for fixed laser input energy. A defocus scan is conducted over five PIC simulations varying defocus position from  $-300\mu\text{m}$  to  $300\mu\text{m}$  with constant maximum energy, and an energy scan over three simulations, varying at 12.5%, 31.6% and 100% of the maximum energy fixed at best focus. As a comparison and control measure of laser propagation and intensity, both sets of simulations are repeated for propagation in vacuum with no plasma. From the series of simulations, the electron energy spectra, and corresponding temperatures, as a function of intensity can be extracted and analysed. Due to transverse scale of the 2D simulations required, only the front surface plasma scale length and  $5\mu\text{m}$  of target bulk was simulated within the available computational resource. However, to complete the study – using Equation 5.4– maximum proton energies ( $E_{\text{max}}$ ) can be modelled from Mora [100] model using the electron temperatures from the simulations and comparing for both intensity scans:

$$E_{\text{max}} = 2k_b T_e [\ln(t_p + \sqrt{t_p^2 + 1})] \quad (5.4)$$

where  $E_{\text{max}}$  is the maximum proton energy,  $k_b$  is the Boltzmann constant,  $T_e$  is electron temperature, and  $t_p$  is the normalised acceleration time for protons derived from  $t_p = \omega_{\text{pi}} t_{\text{acc}} / \sqrt{2exp^1}$ ;  $\omega_{\text{pi}}$  is the ion plasma frequency, and  $t_{\text{acc}} \approx 1.3\tau_{\text{laser}}$  (where  $\tau_{\text{laser}}$  is the pulse duration) approximated by Fuchs [101]. It is important to note that the Mora model assumes one dimensional simple, uniform, isothermal, fluid expansion on the target surface [101].

## 5.2 EXPERIMENTAL RESULTS

In this section the experimental results introduce the first findings demonstrating a difference in front surface plasma dynamics between two methods of intensity control, in otherwise constant conditions. To provide a better understanding of the impact each intensity control method has on an interaction as a whole – from the initial conditions to particle acceleration – we begin by examining the maximum proton energies measured using the RCF stack. Figure 5.4(a) shows the experimentally measured maximum proton energies scaling with nominal intensity – as calculated using the measured laser pulse parameters and factoring in energy throughput and encircled HWHM energy – for variety of laser energies ( $\Delta E_L$ ) and defocus positions ( $\Delta F_P$ ). Defocus position is measured with respect to the off-axis parabola (OAP) drive position to within accuracy of  $\pm 500$  nm.

Assuming uniform behaviour with nominal intensity (in vacuum) regardless of how intensity is varied, one might naïvely expect that the maximum proton energies from each data scan would follow a linear trend with increasing intensity. However, although  $\Delta E_L$  follows this, it is clear that intensity varied by  $\Delta F_P$  does not. Instead we can see that the maximum proton energies are significantly higher for a low range of intensities for  $\Delta F_P$ . This suggests that either: 1 – initial nominal intensity values, calculated from the laser pulse parameters for the defocus pulse, are too low, or 2 – there is an error in the measurement of maximum proton energies from the RCF stack.

To investigate option 1, we calculate intensity by another method. The simplified TNSA proportionality relation ( $E_{\max} \propto \sqrt{I}$ ), derived from the Mora model [100], is applied to predict the intensity required to result in the range of proton energies experimentally measured in the defocus scan, from 0 to 20 MeV. This model is

designed to study charge separation effects within collisionless plasma and determines the maximum energy of accelerated ions. Using this in reverse, inputting the measured maximum energies of the accelerated ions, provides us with a secondary intensity check. These second intensity values are named " $\Delta F_P$  TNSA Est.". In Figure 5.4(a) we can see the trend from the energy scan  $\Delta E_L$  scales as expected, and by applying the fit to the defocus scan ( $\Delta F_P$  TNSA Est.) it is possible to estimate the required on-shot intensity according to the Mora's TNSA proportionality relation.

From this we take our first piece of evidence pointing to an increase in on-shot intensity when controlling intensity by focal spot size, compared to the Mora model TNSA fit and energy scan.

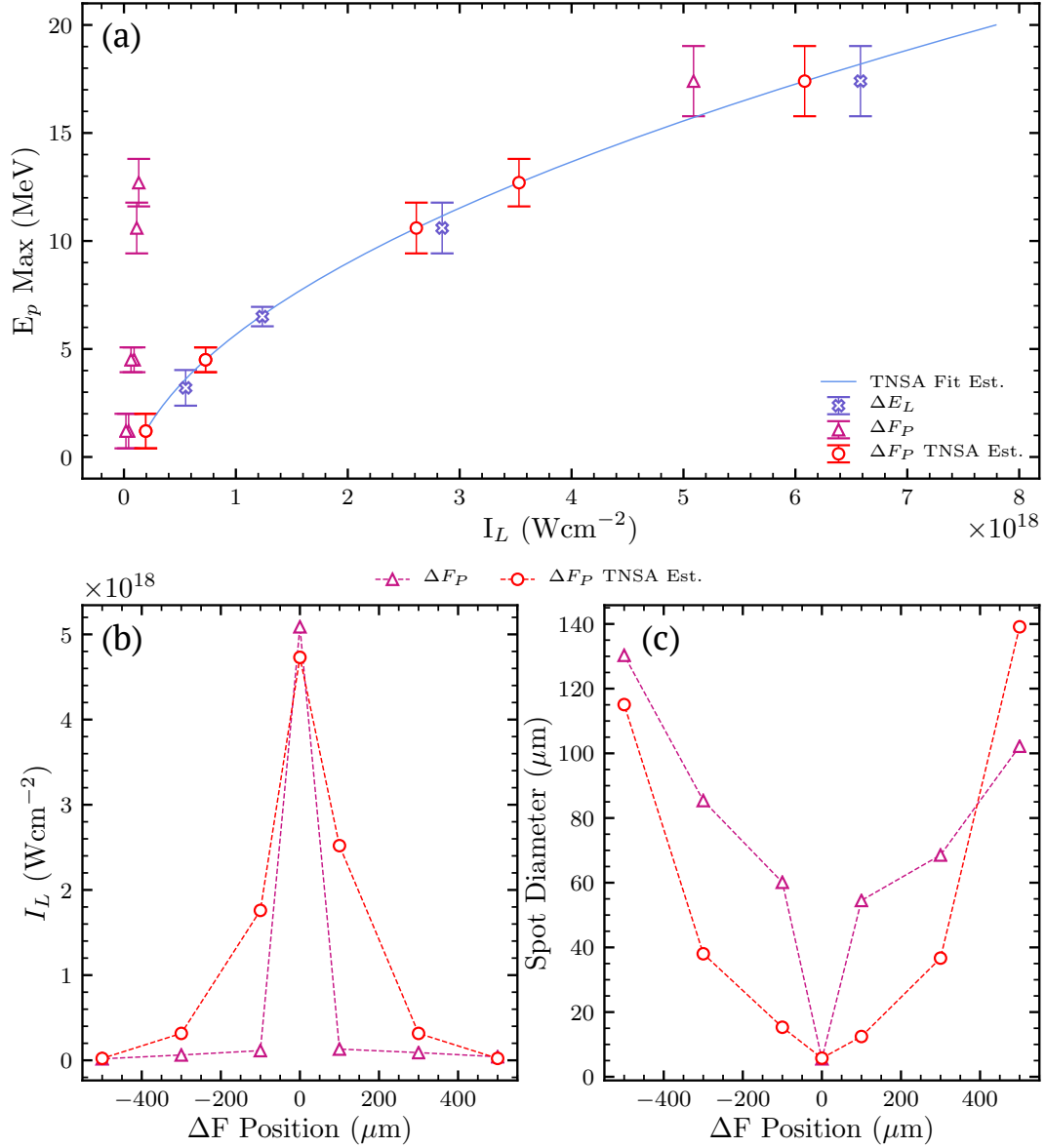


FIGURE 5.4 – (a) Experimentally measured maximum proton energies ( $E_{\text{max}}$ ) for defocus scan ( $\Delta F_P$ ), energy scan ( $\Delta E_L$ ) with a TNSA Fit from a simplified proportionality relation derived from the Mora modal, and corrected  $E_{\text{max}}$  values for defocus scan with TNSA fit ( $\Delta F_P$  TNSA Est.) as a function of nominal intensity; (b) comparison of nominal intensity values with defocus position for the defocus scan from initial measurements in vacuum from focal spot camera ( $\Delta F_P$ ) and those estimated from the TNSA fit; (c) estimates of the focal spot diameters with defocus position, as originally estimated in vacuum, compared to the focal spot diameters derived from the TNSA fit intensity estimates. The focal spot diameter was measured manually in the Java-based image processing software, ImageJ to the nearest pixel,  $0.48 \mu\text{m}$  in size.

The nominal intensities for the defocus scan are compared with defocus position, in Figure 5.4(b) for  $\Delta F_P$  and shifted  $\Delta F_P$  TNSA Est. using Mora model Recalling the parameters outlined in Chapter 2, used to estimate the on-shot intensity, the disparity can be traced back to, and explained further by, either: higher laser energy; shorter pulse duration; or smaller spot size than measured. It is improbable that the laser pulse had more energy than measured, as this would have had to be orders of magnitude more than the calculated error of the measured laser energy to account for the corresponding shift seen in the scaling of maximum proton energies. The change in intensity is too large to be accounted for by laser energy alone. It is also unlikely that a shorter pulse duration is responsible as this would have damaged the optics in the laser system cumulatively, and therefore would not have affected each laser shot within the defocus scan at a steady rate. The possibility that the intensity is higher than expected due to a smaller on-shot focal spot is the probable source of the disparity in maximum proton energy scaling. Self-focusing in plasma is an established phenomenon, as discussed in Chapter 2, which is likely to occur within pre-plasma prior to the main pulse interaction [98, 102]. Using Equation 5.5,

$$I_L = \frac{E_L}{\tau \pi r^2} \quad (5.5)$$

where  $I_L$  is intensity,  $E_L$  is the laser energy,  $\tau$  is the pulse duration, and  $r$  is the focal spot radius, the focal spot diameter for corrected nominal intensities ( $\Delta F_P$  TNSA Est.) can be calculated and compared, in Figure 5.4(c), to the measurements of the focal spot diameter as measured in vacuum. This figure shows the difference in spot size required to increase the on-shot intensity by the amount shown in (b).

To investigate the potential for on-shot spot size variation, other diagnostics are examined for further evidence of disparities in behaviour between the energy and

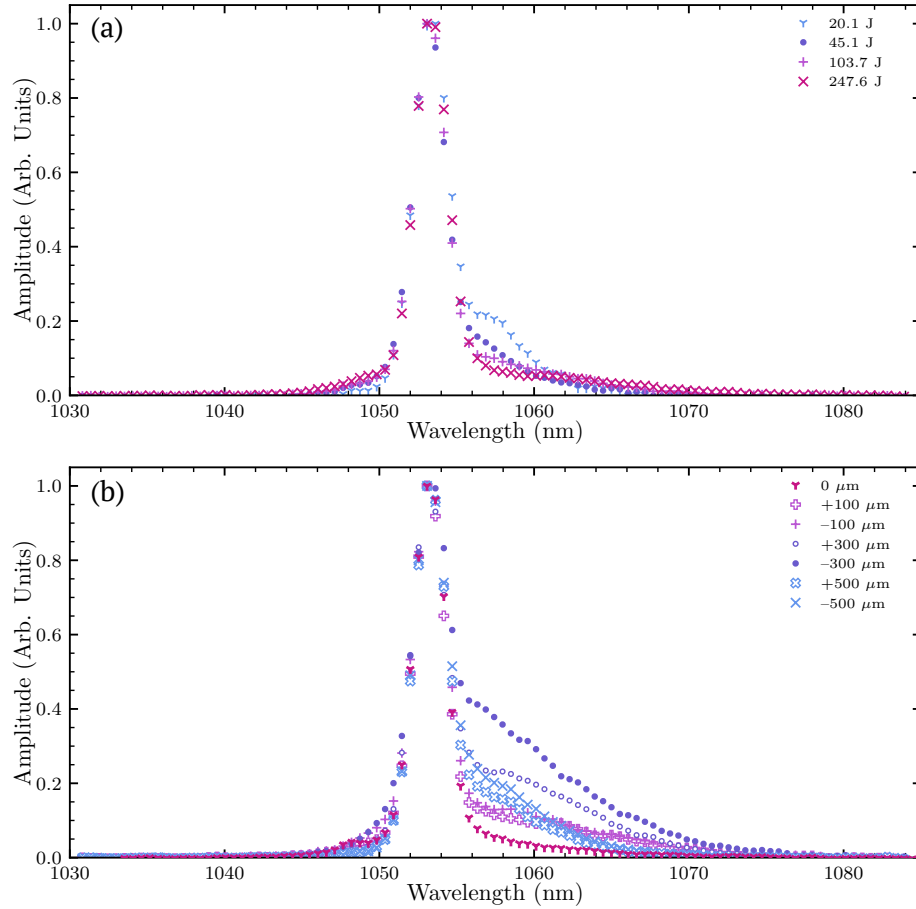


FIGURE 5.5 –  $1\omega$  specular spectra from the energy (a) and defocus (b) data sets showing the full view of measurements around  $1\omega$ .

defocus scan. The  $1\omega_L$  spectra of the specular reflected light from the front surface of the target, for both intensity scans, energy (a) and defocus (b), are shown in Figure 5.5. It is important to note that not all light reflected from the surface is captured, and the measurement is limited by the sample size. Both spectra have been normalised to their peak count at  $1\omega_L$ . By comparing the spectra between (a) and (b), it is clear that introducing a defocus appears to increase the degree of red-shift measured. To examine this more closely, Figure 5.6 zooms in on the red-shift area of both  $1\omega_L$  spectra and also shows the results of analysis of the hole-boring velocities. In (a), there appears to be an increase in red-shift with increasing intensity by laser

energy, but in (d) – where intensity is controlled by defocus – the trend is not as clear. Unlike the highest intensity data set in the energy scan, here in the defocus scan, the highest intensity (at best focus), does not appear to be the most red-shifted. To obtain a more precise measurement of the most red-shifted wavelengths for each data set relative to their peak wavelength, the point of intersection with the background noise signal at 0.001 normalised amplitude, as marked on plots (a) and (d) with a black horizontal line. The peak wavelengths measured for each spectra range from 1053.1 nm to 1054.2 nm  $\pm 0.3$  nm. From each measurement the maximum hole-boring velocity can be calculated, as the difference in red-shift from the peak wavelength of each spectra. The respective calculated hole-boring velocities ( $V_{hb}$ ) are presented as a function of  $c$ , the speed of light in vacuum, with laser energy in Figure 5.6 (b), and with defocus position in Figure 5.6 (e).

As reasonably expected the hole-boring velocity – the rate at which the laser bores into the plasma leading to compression of the plasma electron density – increases accordingly with energy, and therefore with increasing intensity in (b), when intensity tuning is controlled by laser energy. However, for the defocus scan in (e), although the hole-boring velocity increases with increasing intensity, the hole-boring velocity at best focus where the intensity is assumed to be maximised, is comparable to the hole-boring velocity at +100  $\mu\text{m}$ . In fact, the hole-boring velocity is measured to be higher for a defocus of  $-100 \mu\text{m}$  and  $-300 \mu\text{m}$  than at best focus. Recalling that the best focus data set in the defocus scan has a beam energy of 150 J, and that the energy scan is executed with the beam at best focus, we can compare the respective best focus hole-boring velocity divided by the speed of light,  $c$ , (2.58) from (e) to the energy scan plot in (b). Here there is an agreement in 150 J hole-boring velocity between that measured in (e) and the energy scan trend (b), suggesting the irregular trend with defocus position is due to a focal spot effect. Considering the intensities

initially calculated from measurements in vacuum calculated significantly lower on-shot intensities in the defocus scan than the energy scan – recall Figure 5.4(a) – it is unexpected that the hole-boring velocities are higher in most defocused positions.

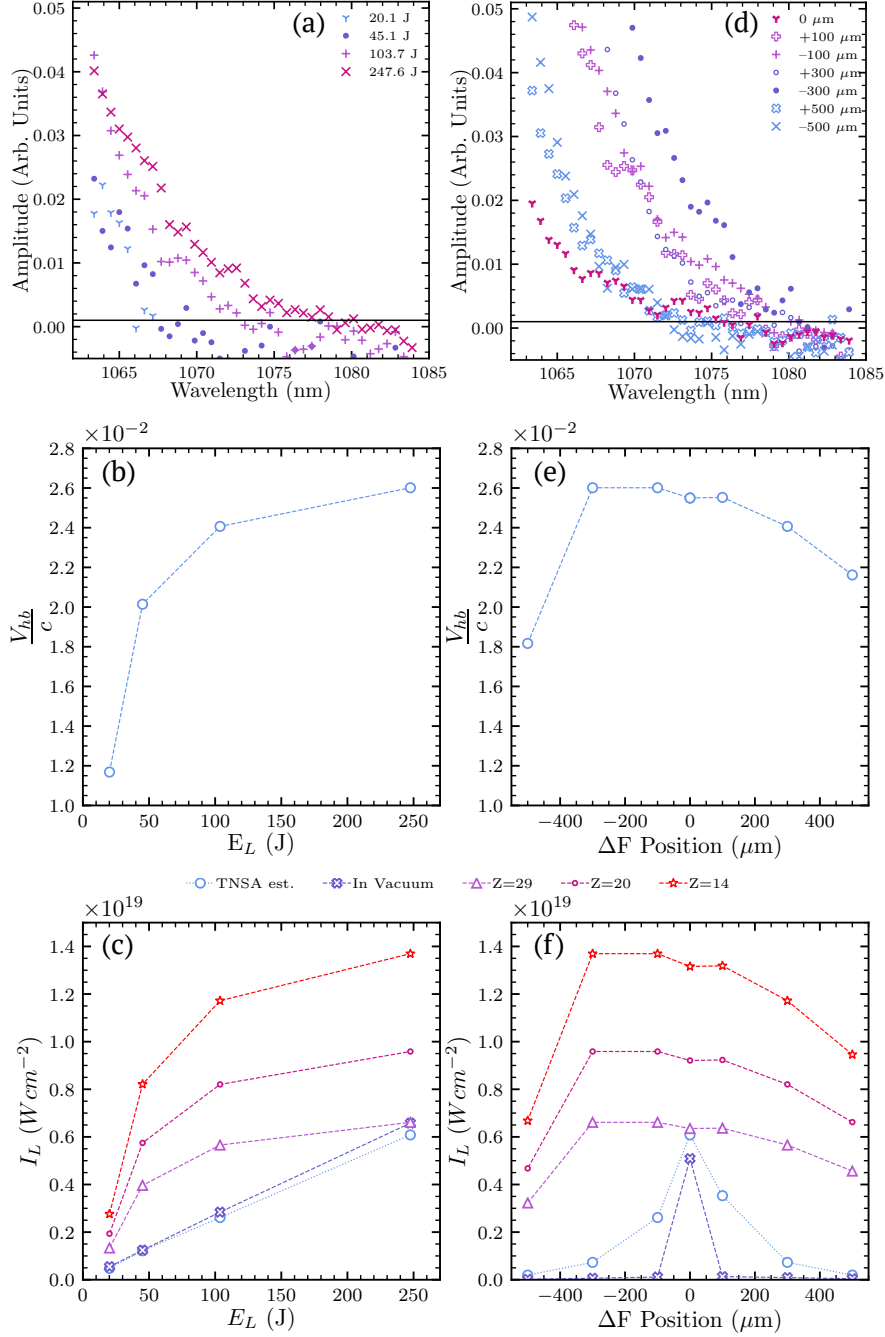


FIGURE 5.6 –  $1\omega_L$  specular spectrometer measurements for the energy scan (a)–(c) and defocus scan (d)–(f). (a) and (d) show a cropped area of the spectra most red-shifted, approaching the cut-off wavelength (that intersects with the horizontal line representing background noise), respectively. (b) and (e) show the trend of calculated hole-boring velocities ( $V_{hb}$ ) in terms of speed of light ( $c$ ), with the respective intensity dependent variables; and (c) and (f) show intensities predicted by Wilks scaling using the calculated hole-boring velocities. These intensities are predicted for various levels of ionisation by controlling the input charge states  $Z = 14, 20, 29$  to the model. Each intensity scaling is compared with those from the initial nominal intensity values calculated from laser pulse parameters in vacuum and also from the Mora model TNSA fit.

In Figure 5.6 (c) and (f), Wilks scaling [99] from equation 5.1 is used to predict the on-shot intensities required to produce the measured hole-boring velocities for both intensity scans, and is examined with laser energy (c) and defocus position (f). For comparison, both the original intensity estimates from vacuum measurements, and the TNSA fit estimations from the measured maximum proton energies are included. The Wilks scaling is applied for charge states  $Z = 14, 20,$  and  $29$  (varying the ion density parameter  $n_i$ ) to explore how the intensity may change with different levels of ionisation within the plasma, with  $Z = 29$  being fully ionised but the most unlikely case due to the intensity needed to result in full ionisation of all electrons. In (c), the Wilks intensity scaling follows a similar upward trend with laser energy, as seen in the TNSA estimate and measurements from vacuum. In the best case,  $Z=29$ , the highest energy shot estimates an on-shot intensity in close agreement with TNSA fit and vacuum values. Although, the more realistic case of  $Z=14$  over-predicts the intensity by a factor of 2.1. In the defocus scan presented in (f), all of the estimations of Wilks scaling with varying degrees of plasma ionisation predicts a significantly higher on-shot intensity than those from the TNSA fit and measurements in vacuum. However, although this may highlight the need for a more accurate model of intensity scaling with hole-boring velocity, in comparison to the energy scan (c), at defocused positions in (f) even the best case of  $Z=29$  does not predict a peak intensity close to TNSA or vacuum values, and the most realistic case of  $Z=14$  predicts the intensity to be a factor of 5.2 higher than the other nominal intensities estimations at  $-100 \mu\text{m}$ . This further consolidates that the behaviour in the specular reflected light from the front surface, is very different with defocused focal spots.

In addition to the  $1\omega_L$  analysis, the  $2\omega_L$  spectra is also examined. Second harmonics are produced when single photons combine together in a nonlinear material, like plasma, and double in optical frequency. Second harmonic light can therefore travel

deeper into plasma before being reflected from the  $2\omega_L$  critical surface. The  $2\omega_L$  results are presented a similar format in Figure 5.7, the energy scan follows the same increasing red-shift with intensity varied by laser energy in (a). Also similar to the  $1\omega_L$  results, we see in (d) that the defocus scan presents an irregular red-shift trend with intensity varied by defocus position, especially with the most red-shifted spectrum being at  $-300 \mu\text{m}$ . From calculating the hole-boring velocities for these measurements presented in (b) and (e), the  $2\omega_L$  hole-boring velocities scales with laser energy (b) as seen in  $1\omega_L$ , although the velocity is higher at the  $2\omega_L$  surface, as expected due to the dispersion relation. In contrast to the  $1\omega_L$  hole-boring velocities for the defocus scan, here in (e) the hole-boring velocity appears to follow a steadier trend with increasing intensity than previously seen from the  $1\omega_L$  measurements. However, the outlier noted at  $-300 \mu\text{m}$  in (d) is clearer in the hole-boring measurements in (e), and suggests the possibility of asymmetrical behaviour either side of best focus. Akin to the  $1\omega_L$  findings, the defocus scan  $2\omega_L$  velocities are also higher than those of the energy scan, despite lower estimated intensities. Finally, the Wilks intensity estimates are presented for the  $2\omega_L$  spectra in the same format as previous. In both the energy scan (c) and defocus (f), the Wilks scaling predicts a significantly higher on-shot intensity again, even  $Z=29$  case exceeds the TNSA fit and measurements from vacuum. Interestingly the  $2\omega_L$  Wilks scaling estimates more comparable nominal intensities between the energy and defocus scan than in the  $1\omega_L$ . Overall, the specular spectrometer results have provided further evidence suggesting there exists conflicting intensity measurements that, like the TNSA fit, are in disagreement with the nominal intensity measurements in vacuum, and are estimated higher for defocused spots.

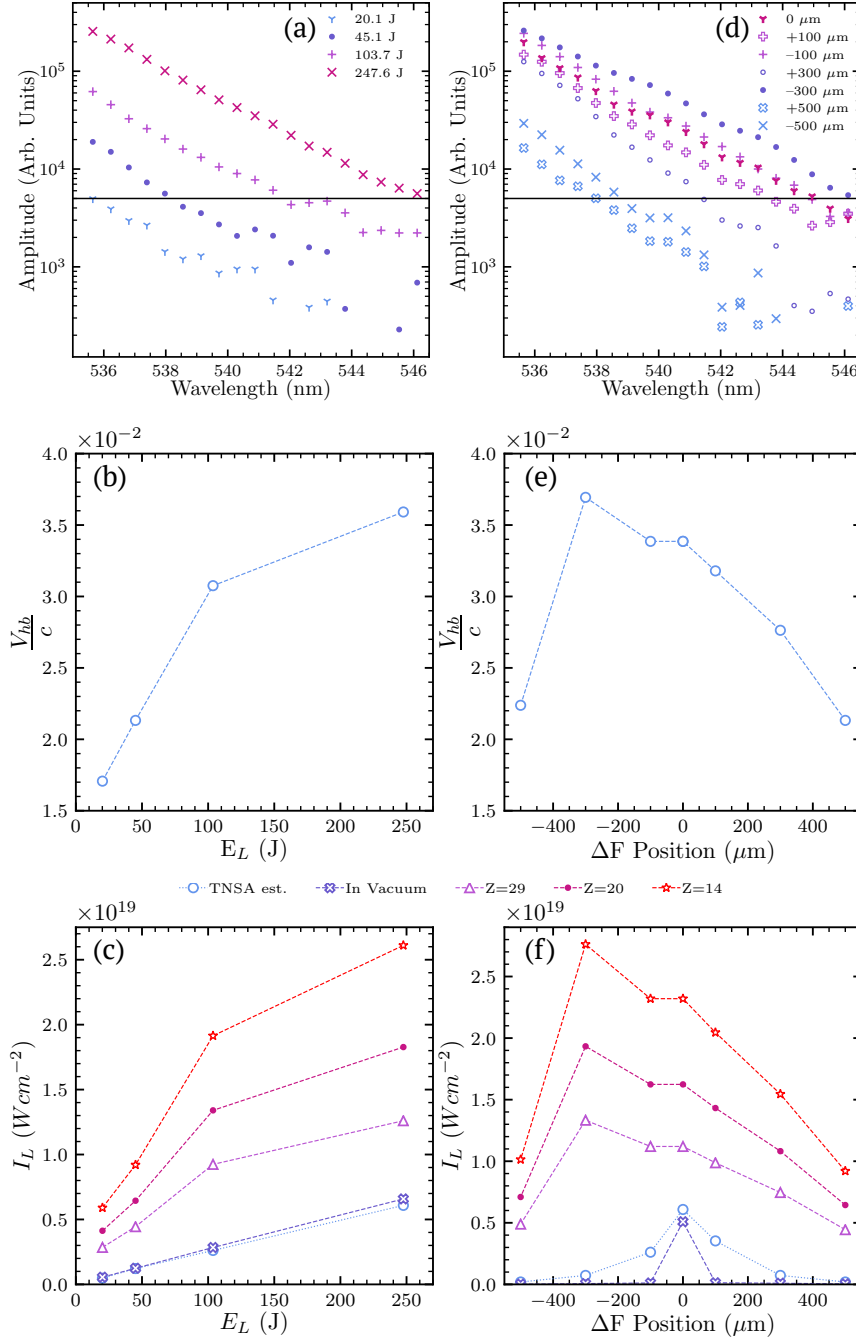


FIGURE 5.7 –  $2\omega_L$  specular spectrometer measurements for the energy scan (a)-(c) and defocus scan (d)-(f). (a) and (d) show a cropped area of the spectra most red-shifted, approaching the cut-off wavelength (that intersects with the horizontal line representing background noise), respectively. (b) and (e) show the trend of calculated hole-boring velocities ( $V_{hb}$ ) in terms of speed of light (c), with the respective intensity dependent variables; and (c) and (f) show the intensities predicted by Wilks scaling for various ionisation levels, by charge states  $Z = 14, 20, 29$  to compare to the nominal intensities calculated from laser pulse parameters, and the Mora model predicted intensities from the TNSA fit.

To investigate further, the experimental results from the multi-channel probe allow the exploration of the temporal evolution of the plasma expansion at the target front surface with increasing nominal intensity in the energy and defocus scans. Figure 5.8 shows the processed images of the energy scan in order of increasing time from left to right, and increasing nominal intensity varied by laser energy upwards (d) 20 J, (c) 45 J, (b) 103.7 J, and (a) 247.6 J. The laser pulse is entering from the right. Here, not only are the key front surface features captured, the capabilities of the probe are also demonstrated. From the presented images, the transverse and longitudinal plasma expansion can be measured, via the method shown in Figure 5.2;

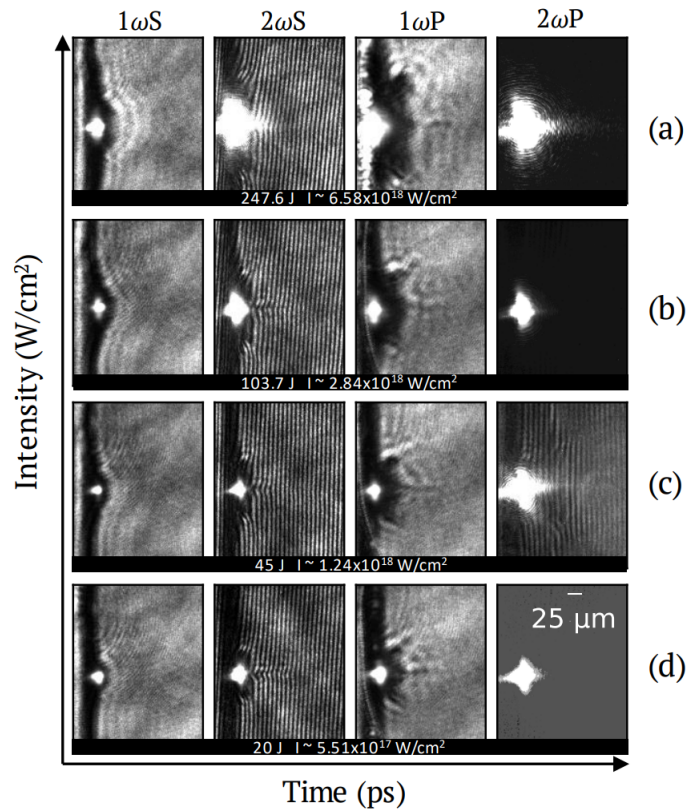


FIGURE 5.8 – The multi-channel probe images of the evolving front target surface, with laser incoming from right to left, at times -183 ps ( $1\omega_S$ ), -3 ps ( $2\omega_S$ ), 117 ps ( $1\omega_P$ ) and 417 ps ( $2\omega_P$ ) with increasing intensity varied by energy (a) 247.6 J, (b) 103.7 J, (c) 45 J, and (d) 20 J.

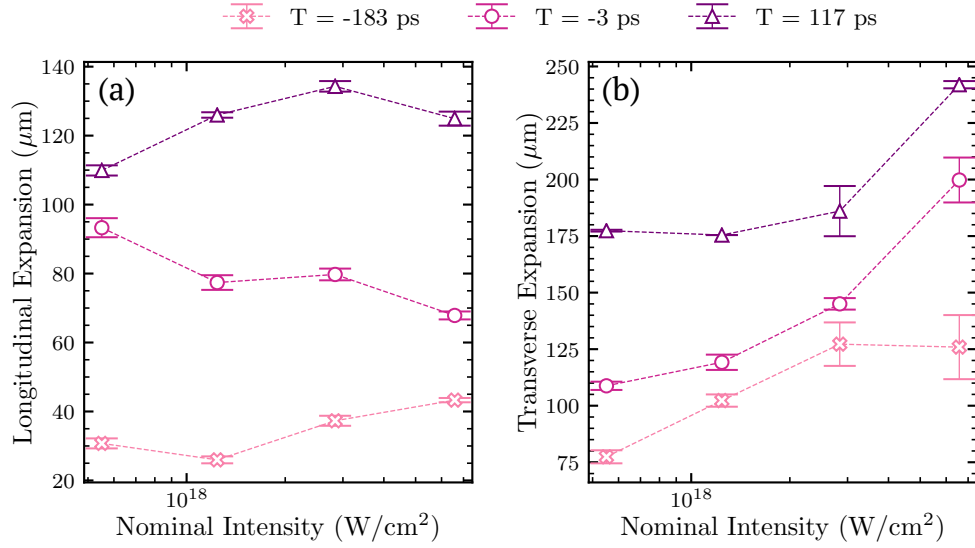


FIGURE 5.9 – Average plasma expansion (a) longitudinal, and (b) transverse measurements from the energy scan multi-channel probe images at three timings of -187 ps, -3 ps and 117 ps. Error bars defined by the standard deviation over repeated measurements.

self emission and scattered light levels can be analysed; and the front surface profile and shape extracted. Figure 5.9 shows the plasma expansion (a) longitudinal, and (b) transverse measurements obtained from image analysis of the energy scan, over three of the probe channels at timings -183 ps ( $1\omega\text{S}$ ), -3 ps ( $2\omega\text{S}$ ), and 117 ps ( $1\omega\text{P}$ ), where  $t = 0$  is the peak of the main pulse. Due to the levels of self emission and challenging contrast levels in the ( $2\omega\text{P}$ ) channel at 417 ps, expansion measurements could only be conducted for three of the four probe channels. The longitudinal plasma expansion (a) appears to increase with laser energy, and so intensity, at the earliest (-183 ps) and latest (117 ps) time frames but decreases with energy when measured immediately before the interaction (-3 ps). The longitudinal expansion rate slows down between the two earliest time frames as intensity is increasing, because with increasing intensity and thermal pressure more expansion occurs towards the end of the interaction (117 ps).

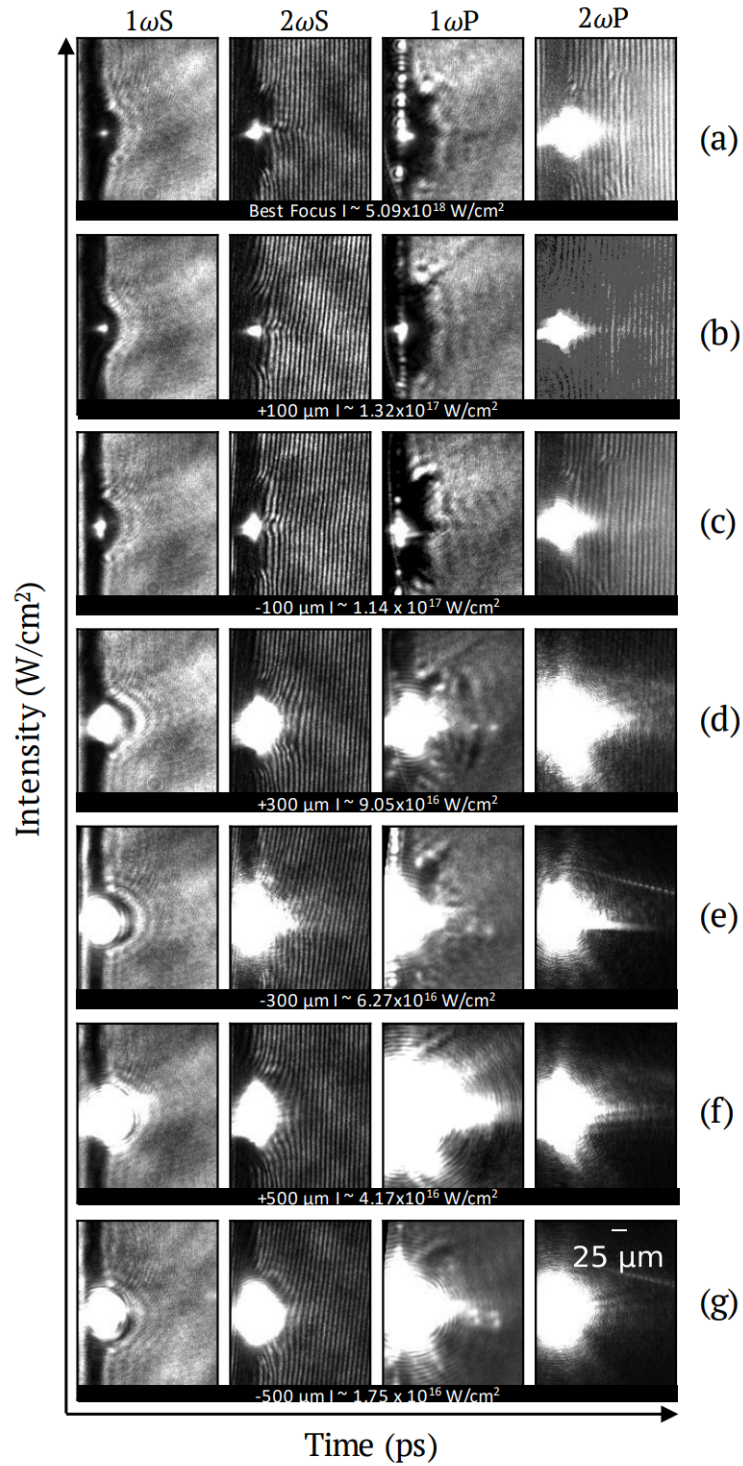


FIGURE 5.10 – The multi-channel probe images of the evolving front target surface at -183 ps ( $1\omega_S$ ), -3 ps ( $2\omega_S$ ), 117 ps ( $1\omega_P$ ) and 417 ps ( $2\omega_P$ ) with increasing intensity varied by defocus position from (a) best focus, (b) +100  $\mu\text{m}$ , (c) -100  $\mu\text{m}$ , (d) +300  $\mu\text{m}$ , (e) -300  $\mu\text{m}$ , (f) + 500  $\mu\text{m}$ , and (g) -500  $\mu\text{m}$ .

This is due to the peak of the pulse inducing greater radiation pressure on the plasma preventing it from expanding along the laser axis, as detailed in Chapter 2. The transverse plasma expansion results (b) are much clearer in showing that over all time frames the transverse expansion is increasing with intensity. Figure 5.10 shows the multi-channel probe images from the defocus scan in order of increasing time from left to right, -183 ps ( $1\omega_S$ ), -3 ps ( $2\omega_S$ ), and 117 ps ( $1\omega_P$ ) and increasing upward with intensity with defocus positions (g) -500  $\mu\text{m}$ , (f) + 500  $\mu\text{m}$ , (e) -300  $\mu\text{m}$ , (d) +300  $\mu\text{m}$ , (c) -100  $\mu\text{m}$ , (b) +100  $\mu\text{m}$ , and (a) best focus. In contrast to the self-emission observation from the energy scan, it is worth noting the levels of self-emission decrease with increasing intensity when varied by defocus position and spot size. It appears the amount of self-emission scales with increasing spot size, which could be due to a larger area of the target being excited with every increase in defocus position. Interestingly, plasma jet like structures can also be seen on the  $1\omega_P$  channel at 117 ps across both energy and defocus data sets. Plasma jets are trapped electrons within the plasma which are being field by the magnetic field. Although not included in these experiments, it would be possible to utilise the multi-channel probe to measure the evolution of plasma jets on ultra-short timescales. From the presented matrix of front surface images, the transverse and longitudinal plasma expansion is measured and presented for either side of best focus with two estimates of nominal intensity, as shown in Figure 5.11 and Figure 5.12, respectively.

In contrast to the transverse expansion increasing with increasing intensity varied by energy, in Figures 5.11(a) and (b) the transverse plasma expansion after focus is decreasing with increasing intensity varied by defocus position. Including the TNSA intensity estimate shift in (b), shows a more gradual decline across all timings. The expansion rate, seen as the distance between the temporal measurements within a single interaction is becoming smaller, and therefore the rate of expansion is slower,

with increasing intensity towards best focus. Similarly, a decrease in expansion with increasing intensity toward best focus is also apparent before focus, for both (c) and (d) with respective nominal intensity scalings. Although a decrease in transverse expansion with increasing intensity by defocus position, and therefore decreasing spot size, seems sensible as a smaller spot will interact with less of the target surface area – a decrease in the rate of plasma expansion does not. In contrast, in the energy scan, which is fixed at best focus, the rate of transverse expansion is increasing with intensity, even at lower laser energies Figure 5.9(b).

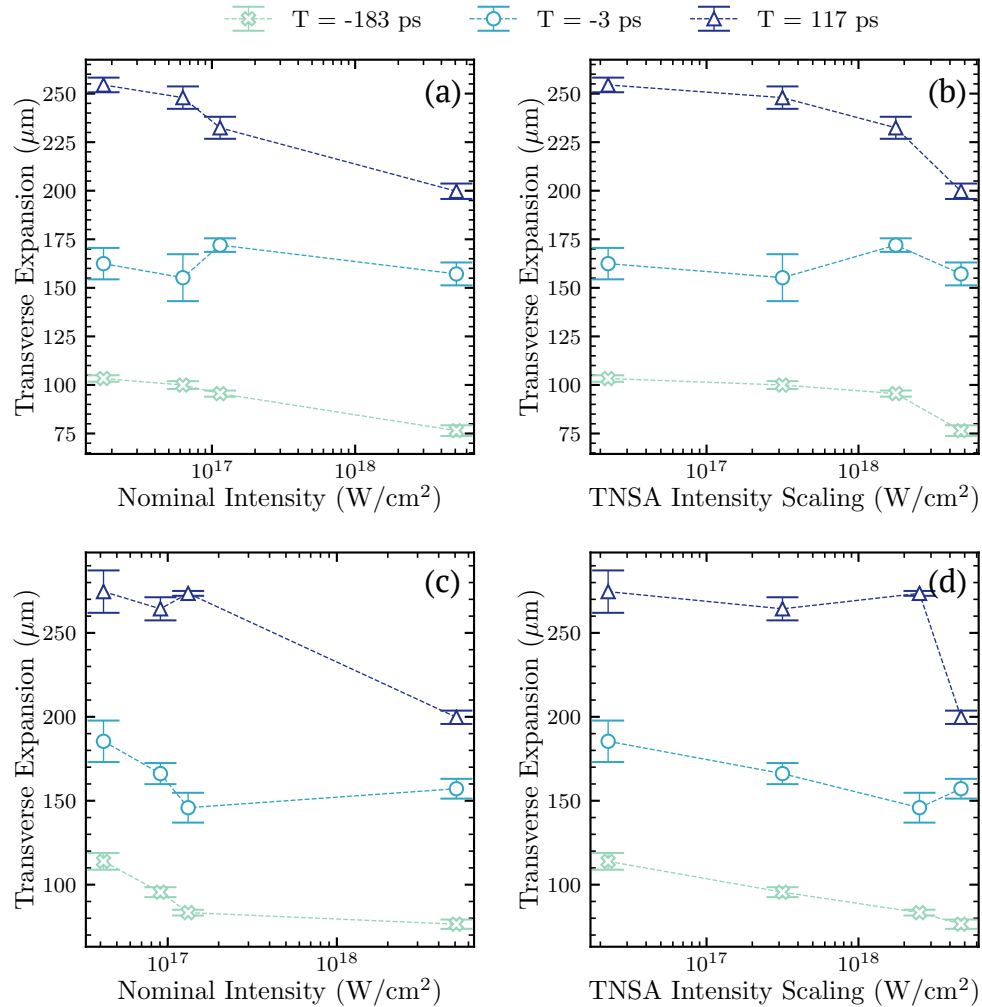


FIGURE 5.11 – The evolving, average transverse plasma expansion measurements over three probe timings  $-183$  ps ( $1\omega\text{S}$ ),  $-3$  ps ( $2\omega\text{S}$ ), and  $117$  ps ( $1\omega\text{P}$ ) for (a)+(b) after focus ( $-100$ ,  $-300$ ,  $-500$   $\mu\text{m}$ ); and (c)+(d) before focus ( $+100$ ,  $+300$ ,  $+500$   $\mu\text{m}$ ) with two measures of nominal intensity: (a) and (c) from vacuum, and (b) and (d) TNSA fit estimate. The error bars are defined by the standard deviation from the mean.

Figure 5.12(a) and (b) show the evolving longitudinal measurements of the plasma expansion after focus, with a decline in expansion size and rate with increasing intensity towards best focus. Similarly, the same downward trend of longitudinal plasma expansion is measured before focus as shown in (c) and (d), although here it appears that the expansion rate peaks for a lower intensity varied by a defocus

of  $-300 \mu\text{m}$ . This demonstrates the opposite behaviour as seen in the energy scan, where the longitudinal expansion increases in magnitude and rate with increasing intensity when varied by laser input energy.

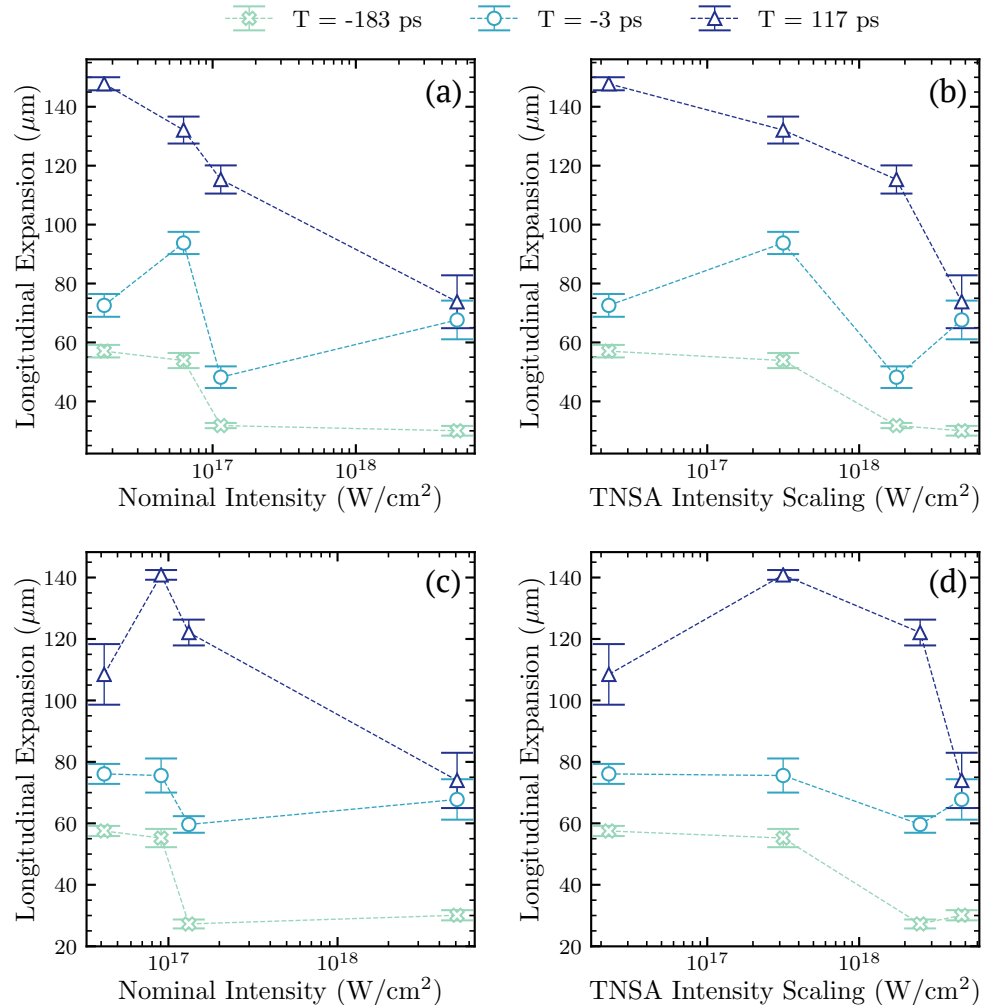


FIGURE 5.12 – The evolving, average longitudinal plasma expansion measurements over three probe timings  $-183 \text{ ps}$  ( $1\omega\text{S}$ ),  $-3 \text{ ps}$  ( $2\omega\text{S}$ ), and  $117 \text{ ps}$  ( $1\omega\text{P}$ ) for (a)+(c) before focus ( $+100, +300, +500 \mu\text{m}$ ); and (b)+(d) after focus ( $-100, -300, -500 \mu\text{m}$ ) with two measures of nominal intensity: (a)–(b) from vacuum, and (c)–(d) TNSA fit estimate. Error bars defined by the standard deviation over repeated measurements.

Figure 5.13 shows the rate of expansion with intensity for longitudinal (long) and transverse (trans) measurements in the defocus scan, before focus (BF) and after

focus (AF), and energy scan (E). Calculated by taking the difference in expansion measurements over the time interval between probe images, the figure shows that the rate of transverse expansion decreases with intensity controlled by spot size after focus and laser energy, but increases with decreasing spot size when the intensity is tuned by defocusing before focus. This could be due to the wavefront of the defocused pulse before focus matching the curvature of the front surface plasma and containing the transverse expansion better than the wavefront of a laser pulse defocused negatively (after focus) - as shown in the defocus diagram in Figure 5.1. For all data sets, the rate of longitudinal expansion appears to increase with intensity. The rate of transverse and longitudinal expansion mirror each other in the energy scan as the longitudinal plasma expansion dominates with increasing intensity due to hole-boring of the laser, and the rate of transverse expansion retreats as expansion is focused into the forward projection. This exchange in plasma expansion between the two dimensions is not as clear in the defocus scan.

To summarise the experimental findings, the measurements and analysis from three key diagnostics have been presented which include: RCF measured maximum proton energies; back-reflected specular spectra; and the temporally resolving multi-channel probe images. Each of these diagnostics provide a measure of how laser-plasma interactions and their dynamics evolve as intensity is varied by two different methods: laser energy with a fixed focal position, and defocus position with fixed laser energy. By comparing the measurements of front surface plasma expansion, hole-boring velocities, maximum proton energies, and their respective intensity scalings, between the defocus scan and energy scan we can gain an insight into whether the method in which intensity is varied influences the interaction behaviour. The results from these different diagnostics all suggest there is a difference in behaviour depending on method of intensity control, and that the difference is in the efficiency of coupling

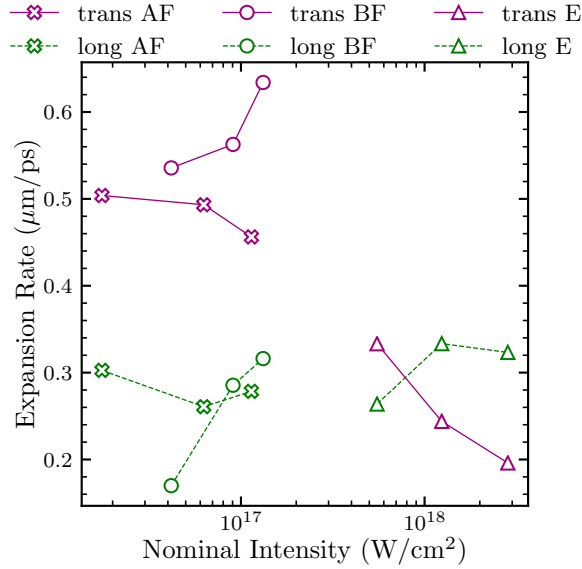


FIGURE 5.13 – The expansion rate calculated between 3 temporal measurements of transverse (pink) and longitudinal (green) plasma expansion at -183 ps ( $1\omega_S$ ), -3 ps ( $2\omega_S$ ), and 117 ps ( $1\omega_P$ ) for the defocus scan, before focus (BF) and after focus (AF), and the energy scan (E), all scaling with nominal intensity.

energy into the plasma (as seen in the plasma expansion, hole boring velocities and resultant maximum proton energies measured). In addition to this, the defocus scan has individually shown that there is a degree of asymmetric behaviour depending on which side of best focus the target is positioned. The multi-channel probe has provided, for the first time, multiple picosecond scale intra-interaction imaging that has shown significant variation in the evolution of the front surface when controlling the intensity by energy or by defocus position. The consequence of which can be measured and tracked throughout a single laser-plasma interaction and measured in spectrum of reflected light from the target front surface, and maximum proton energies.

### 5.3 SIMULATION RESULTS

In this section the simulation results are introduced that support the experimental findings reported. As detailed in the method section, 1D Lagrangian radiation-hydrodynamic simulation code HELIOS is used to provide an estimate of the scale length of plasma expansion on the target front surface. Figure 5.14 (a) shows the model of the plasma expansion profile up to  $25 \mu\text{m}$  in front of the target surface. The HELIOS simulation is run for 1 ns and the density profile is sampled at the end of the simulation. The plasma scale length is estimated at  $\approx 6 \mu\text{m}$ , using Equation 5.2, and applied to the series of 2D PIC EPOCH simulations with varying intensity by laser energy and focal position, in otherwise constant conditions. In all cases, the simulations have an initial neutralised electron density profile as shown in Figure 5.14 (b).

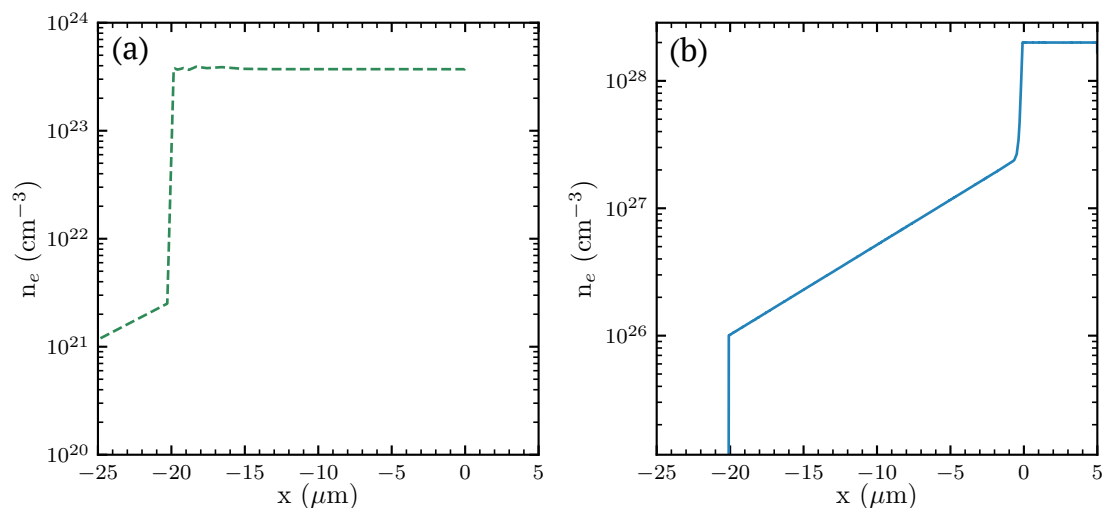


FIGURE 5.14 – (a) The extracted electron density profile from radiation-hydrodynamic simulation, HELIOS, for the minimum ( $1.75 \times 10^{16} \text{ W/cm}^2$ ) intensity achieved experimentally with a contrast of  $10^6$  at  $t=0$  relative to the peak of the pulse. (b) The initial longitudinal electron density profile used in the 2D PIC simulations.

With this, two sets of intensity scan simulations are undertaken for a defocus scan, with fixed laser energy, and an energy scan with fixed focus position. The defocus position is varied from  $-300\mu\text{m}$ ,  $-100\mu\text{m}$ ,  $0\mu\text{m}$ ,  $100\mu\text{m}$ ,  $300\mu\text{m}$  in the simulations with a fixed normalised energy equal to 1. The peak laser energy is varied by 0.125, 0.3, and 1 at best focus to simulate an energy scan in otherwise constant conditions. Both intensity scans are repeated for laser propagation with and without pre-plasma for comparison, with the PIC input parameters detailed in Table 6.1. By defocusing the laser pulse negatively and positively, the focal spot interacting with the target surface on the x-plane within the simulation is changed. A sample of the 2D PIC electron density plots at  $t=0$  from the defocus simulation series for  $\pm 100\mu\text{m}$  and best focus, in the pre-plasma determined by the HELIOS simulations at a contrast of  $10^6$ , can be seen in Figure 5.15. Time  $t=0$  is defined as when the peak of the laser interacts with the nominal front surface for each simulation. A slight asymmetry can be seen in filamentation in (a)  $+100\mu\text{m}$  and (c)  $-100\mu\text{m}$ .

From the no pre-plasma and pre-plasma cases, the maximum intensity achieved in the simulation can be determined and compared for each simulation set. The

Quantity	Value
FWHM	$3\mu\text{m}$
Peak Intensity	$5 \times 10^{18} \text{ W/cm}^2$
Peak Density	$20 n_{\text{crit}}$
Pulse Duration	800 fs
Simulation Length	3 ns
Ion Species	Cu 11+
Initial Electron Temperature	10 keV
Mesh Size	$6000 \times 16000$
Box Size	$30\mu\text{m} \times 80\mu\text{m}$

TABLE 5.1 – 2D PIC EPOCH simulation input parameters and values, for laser pulse of peak intensity  $5 \times 10^{18} \text{ W/cm}^2$  interacting with a copper target.

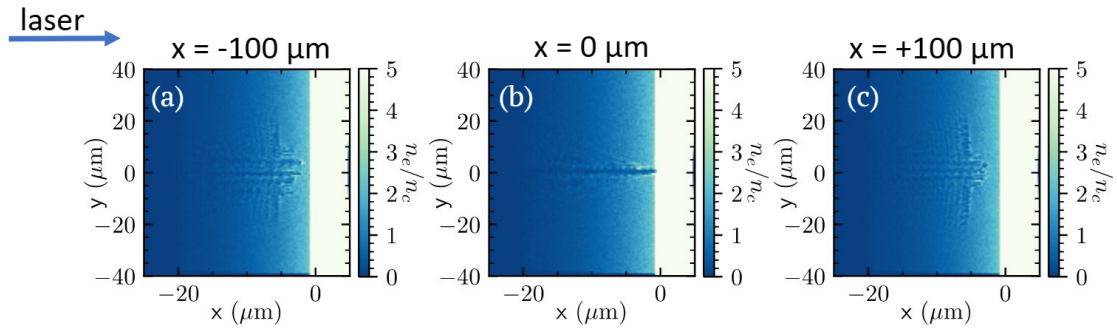


FIGURE 5.15 – 2D electron density maps obtained from the PIC simulations at a time of  $t=0$  (defined as when the peak of the laser interacts with the nominal front surface) for the intensity scan varied by defocus positions at (a)  $-100 \mu\text{m}$ , (b)  $0 \mu\text{m}$ , and (c)  $+100 \mu\text{m}$ .

maximum intensity is determined from the square of the electric field in the simulation. Figure 5.16 shows the peak intensity achieved from the simulations with no plasma for both the laser energy scan (a), and defocus scan (b). For both the energy varied and defocus varied simulations, the on-target intensity in pre-plasma is higher than the no plasma case at every incremental increase of energy and defocus position, respectively. This is due to the presence of pre-plasma inducing stronger self-focusing, as reported by [98, 102], and delivering the laser energy in a smaller focal spot and, therefore, higher on-shot intensity. With further examination, we can see that the shift in intensity in the presence of pre-plasma, is increasing with increasing laser input energy as shown in Figure 5.16 (a). In contrast, Figure 5.16 (b) shows the change in intensity is decreasing with increasing defocus position away from best focus. As a more direct comparison of the relative change in intensity in both the energy and defocus scan, Figure 5.17(a) measures the ratio ( $R$ ) of the intensity determined in pre-plasma to the no plasma control case. Here, the  $R$  value peaks at  $\approx 2.6$  for intensity varied by defocus, compared to a peak  $R$  value of  $\approx 1.8$  when intensity is varied by laser energy. Examining the gradient of the  $R$  value with nominal intensity, it appears intensity varies more strongly with reducing spot size. It should be noted

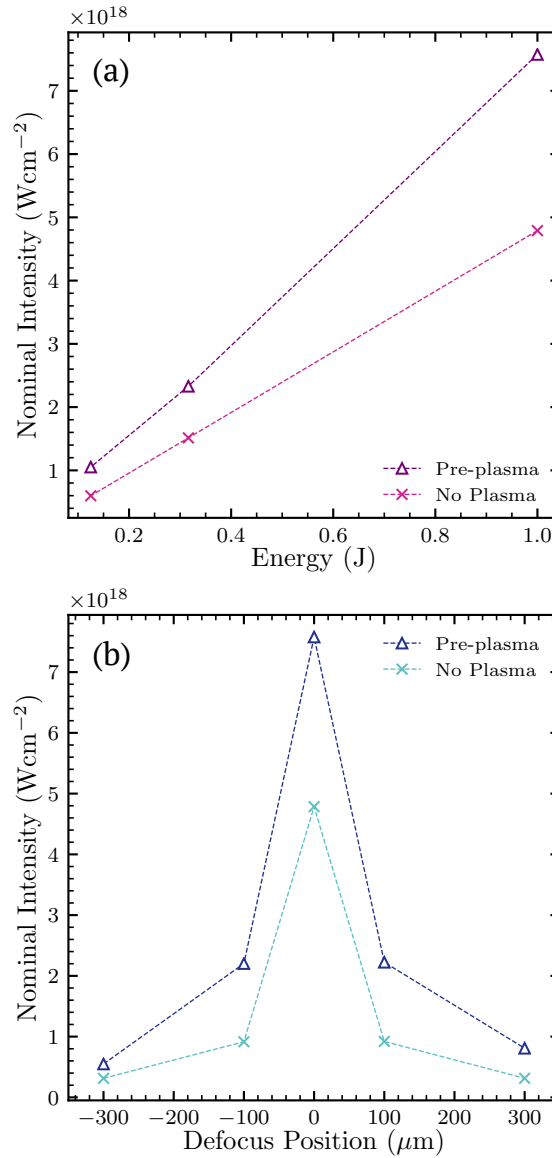


FIGURE 5.16 – Simulation results of nominal intensity values with and without pre-plasma for intensity scans varied by (a) energy and (b) defocus position.

that these are 2D simulations, and as such the increase in intensity due to reducing spot size is a linear increase with radius, as opposed to the square of the radius – therefore this effect will be more appreciable in reality. As previously discussed, attributing the change in on-shot intensity in pre-plasma to stronger self-focusing, Figure 5.17(a) suggests that self-focusing increases strongly with increasing defocus

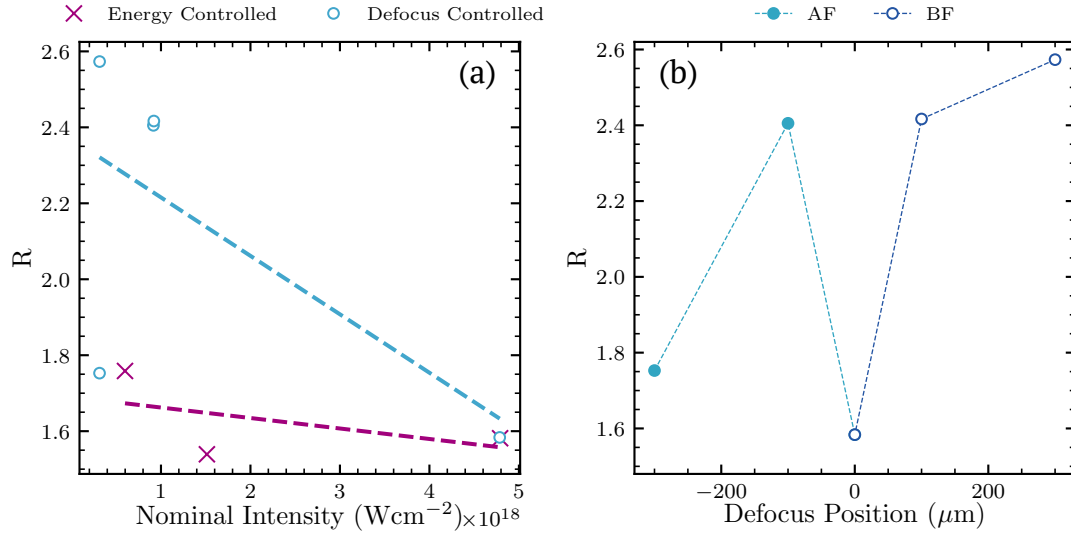


FIGURE 5.17 – Comparing ratio,  $R$ , of nominal intensity from self focusing to (a) the nominal intensity determined for no plasma, for both sets of intensity scans controlled by energy and defocus position, and (b) defocus position demonstrating asymmetries either side of best focus, before focus (BF) and after focus (AF).

position, despite the energy in all of the defocus simulations effectively being the same, and therefore with increasing spot size. From this, we propose that self-focusing has a larger impact on on-shot intensity when the focal spot is defocused, which perhaps aids self-focusing more than varying laser energy. In addition to this, Figure 5.17(b), shows the intensity ratio as a function of defocus position. Interestingly, further disparities emerge in the method in which intensity is varied as, a defocus of  $-300 \mu\text{m}$  is calculated to have a lower  $R$  value than  $+300 \mu\text{m}$ .

The corresponding electron spectra is investigated for both intensity simulation sets varied by (a) energy and (b) defocus position as shown in Figure 5.18. For the energy varied simulation series (a), the spectra for the lower input energies both cut-off between 2 – 3 MeV. Whereas, for the defocus simulation series (b), the four defocused pulses ( $\pm 100 \mu\text{m}$  and  $\pm 300 \mu\text{m}$ ) have a larger range of cut-off energies between 1.6 – 4 MeV. As the defocused simulations have a nominal intensity less than that of the reduced energy simulations, this indicates that the resultant self-focusing

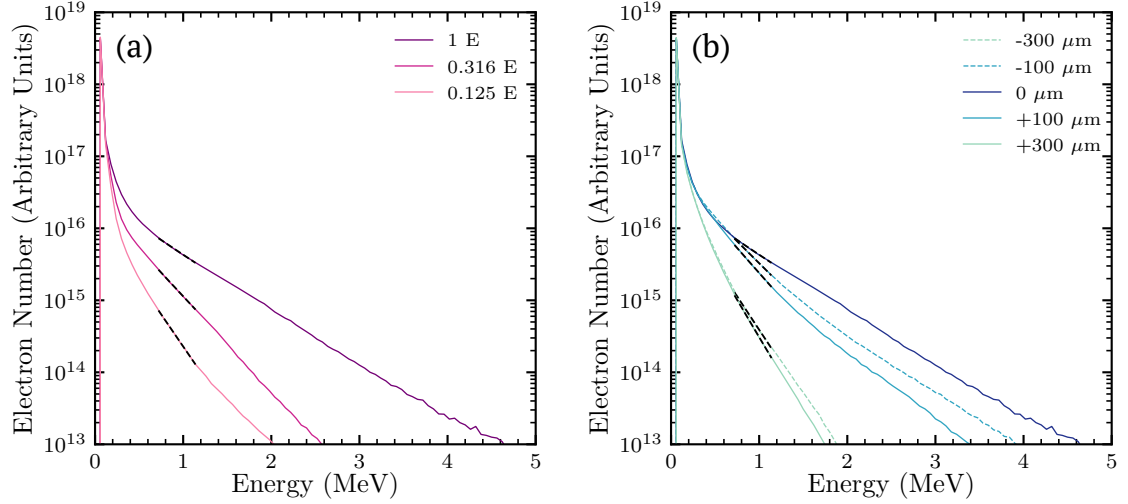


FIGURE 5.18 – The electron spectra extracted from 2D PIC simulations at the peak of the interaction for the (a) energy controlled intensity scan at full, a third, and an eighth of the maximum energy, and (b) defocus scan fixed at full energy and varying defocus positions of  $\pm 100 \mu\text{m}$  and  $\pm 300 \mu\text{m}$ , as well as best focus. The black dotted line region indicates the electron spectra gradient range used in electron temperature calculations.

intensity increase is driving the increase in maximum electron energies, compared to the equivalent intensity reached by variation of energy. To further support this, the electron temperature is extracted and presented in Figure 5.19(a) as a function of maximum intensity – determined by sampling from the electron spectra gradient between 0.6 MeV – 1.2 MeV, and marked as a dashed line in 5.18 (a) and (b). Here the electron temperature is found to scale with achieved intensity. The figure shows electron temperature increasing with achieved intensity for both energy and defocus simulation sets. However, comparing the electron temperatures in Figure 5.19(a) from the energy scan at 0.316 E and defocus scan  $\pm 100 \mu\text{m}$ , where  $I \approx 2 \times 10^{18} \text{ W/cm}^2$  for both cases, the electron temperature is higher for the defocus controlled simulations after focus compared to the energy scan simulation, and also compared to before focus. This provides further evidence of an asymmetric effect in the direction of

defocus, that could be due to the wavefront matching the curvature of the pre-plasma expansion before focus which despite resulting in a slightly higher on-shot intensity also leads to increased containment of plasma expansion through heating.

The simulated electron temperatures could then be substituted into equation 5.4 to estimate the expected maximum proton energies [100]. This provide us with a comparison to the experimentally measured maximum proton energies. This is shown in Figure 5.19(b). The simulated maximum proton energies are calculated to be highest for a defocused focal spot, after focus, compared to the energy controlled at equivalent nominal intensities. When compared with the experimental results in Figure 5.20 it can be seen that the simulations predict a similar trend in maximum proton energies with intensity controlled by laser input energy to the experimental energy scan and TNSA fit from the simplified Mora model. The simulations suggest similar maximum proton energies for the defocus scan as experimentally measured but with higher achieved intensities compared to experimentally nominal intensity values – much as the Mora model relation suggested as discussed at the start of this chapter, due to self-focusing. This result demonstrates that the method in which intensity is varied is a crucial consideration that can give rise to different degrees of self-focusing, on-target intensity and, potentially, ion acceleration.

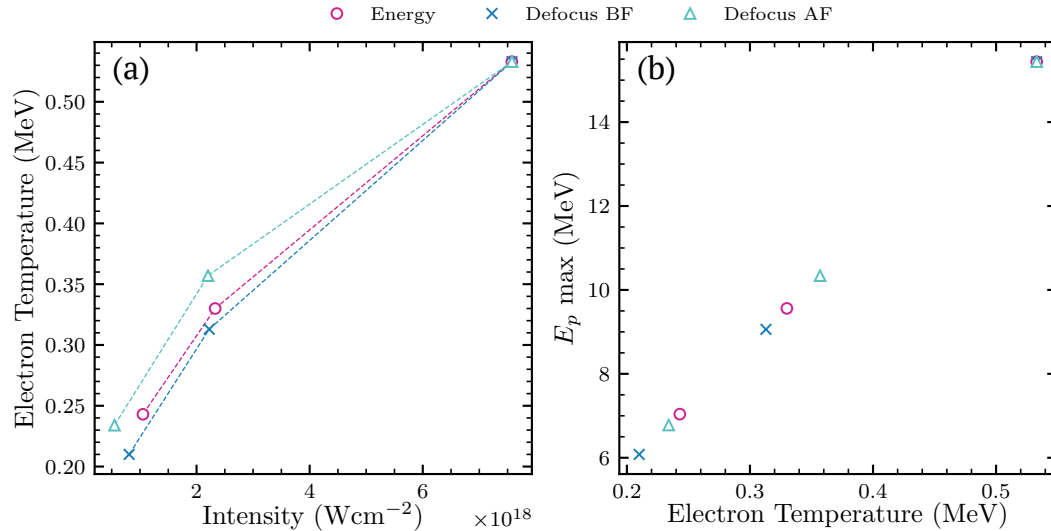


FIGURE 5.19 – (a) The electron temperatures for both the energy scan, and defocus scan (before and after focus) with nominal intensity; and (b) the corresponding maximum proton energies with electron temperature.

## 5.4 SUMMARY AND CONCLUSION

In conclusion, the sensitivity and potential impact of utilising laser input energy and defocus position as methods of intensity control has been investigated both experimentally and with simulations. The results show that the two methods produce different interaction physics. The degree of self-focusing varies with the method in which intensity is varied, evident in measurements of intensity, electron temperature and energy, maximum proton energies, hole-boring velocities, and rate of plasma expansion on the target front surface. This study has also uncovered potential asymmetrical behaviour, observed across multiple experimental diagnostics and 2D PIC simulations, between the direction of defocus either side of best focus. The asymmetries may be due to increased control of front surface plasma expansion and a stronger degree of self-focusing when the laser beam is positively defocused (before focus) and the wavefront is optimised to match the curvature of the pre-plasma surface

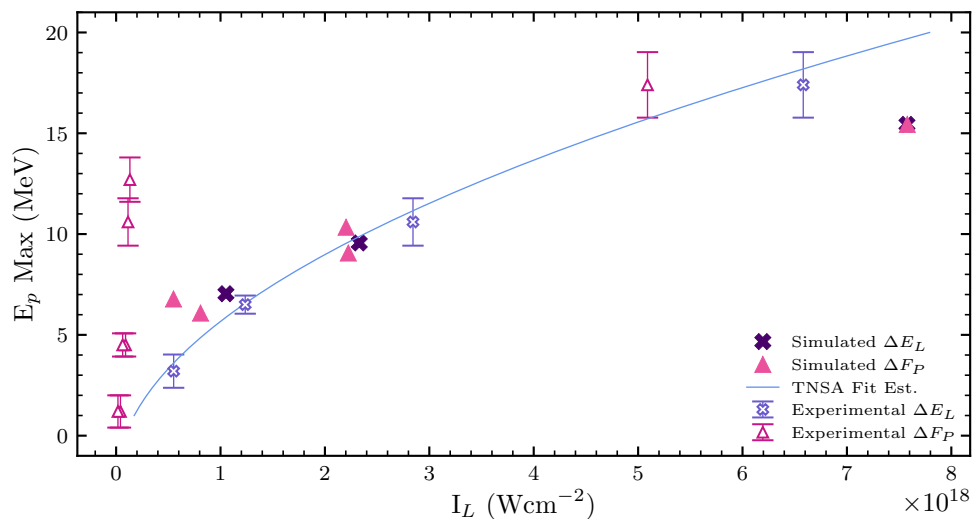


FIGURE 5.20 – Recreated plot of the first experimental results shown in this chapter, now compared to the simulated proton energies for both the energy and defocus scan, as a function of laser intensity, with the TNSA fit from the Mora model overlaid.

expansion, compared to when the laser is negatively defocused (after focus) and the wavefront is working against the curvature of the pre-plasma surface expansion. The experimental results section introduced the RCF measured maximum proton energies for both the energy and defocus scan. It was hypothesised that in order for the maximum proton energies in the defocus scan to be as high as experimentally measured, the true intensity on-target may be higher than the nominal intensity. Using the Wilks [99] intensity scaling model, and the maximum proton energy relation from Mora [100] plasma expansion model, the experimentally measured hole-boring velocities and proton energies both suggest that the on-target intensity is higher than originally calculated. However, both models disagree in absolute nominal intensity values, which is likely due to limitations in both models as they do not consider the method in which intensity is varied and consider only simple 1D plasma expansion, as suggested by Brenner et al. [103].

For the first time, the multi-channel probe has enabled temporally resolved

shadowgraphy images of the front surface conditions within a single interaction, and with that has shown that dynamics evolve differently depending on the method in which intensity is varied. The transverse plasma size increases with laser energy, and therefore intensity, but decreases with intensity when controlled by decreasing focal spot size. Similarly, the rate of plasma expansion appears to increase with increasing intensity varied by laser energy, but decreases with increasing intensity varied by defocus position. The difference in initial conditions imaged and measured, due to stronger self-focusing with larger spot sizes, contributes to the disparities later measured in the RCF stack and specular diagnostics. Simulations enable the comparison of the two methods of intensity control to be investigated, for pre-plasma and no pre-plasma, and similar behaviour was observed for achieved on-target intensities, maximum proton energies, electron energies and temperatures. The simulations indicate that a higher on-target intensity occurs when pre-plasma is present, compared to propagation in no pre-plasma. This agrees with previous findings that have shown that preformed plasma impacts proton acceleration [104, 105], laser-absorption [80] and self-focusing [98, 102]. Our findings suggest that the degree of self-focusing, and on-target intensity, is enhanced by preformed plasma when illuminated by a defocused laser pulse within the range of laser parameters explored [104]. This builds on important findings from many other studies [90, 103, 106–110] that have reported various effects due to changes in the laser spatial profile, that suggest advantages to using a defocused laser pulse, such as: higher ion flux [90]; proton energy spectra drop off [109, 111]; acceleration distance [108]; and laser absorption [107]. Furthermore, observations from this investigation have suggested, for the first time, that the behaviour is asymmetrical either side of best focus, and there may be an advantage to defocusing to one side over the other and may warrant further investigation.

The results in this chapter have highlighted that it is not appropriate to assume that intensity can be varied purely through focal spot size without considering effects such as self-focusing or wavefront geometry. This provides us with the opportunity to better understand the underlying effects of using input energy or defocus position as methods of intensity control, and to resolve whether we can better use these effects to our advantage. Doing so is a step towards maximising the tools we already have available to experimentally tailor intensity. Future experiments should consider utilising self-focusing and wavefront matching to the curvature of the pre-plasma expansion with a positively defocused laser pulse to maximise on-target intensity. Although it is important to note that the impact of shot-to-shot variation in laser pulse spatial profile and fluence may increase with defocus laser pulses and larger spot sizes. The results presented here, and by others, suggest not only exploring higher laser input energy but also optimising the efficiency of the interaction, with fixed energy, through inducing self-focusing. From this work, pinpointing the upper and lower boundaries of interaction efficiency through optimising self-focusing would be an interesting avenue to follow next. To discover the maximum on-shot intensity for minimal laser input energy by optimising self-focusing –that potentially occurs at one side of defocus– would be of great interest across the laser-plasma community. This could involve a series of experiments, measuring the intensity profile evolving over fine-tuned picosecond steps during the peak of the interaction via multi-channel probe interferometry. Temporal measurements of the on-shot intensity, evolving with different degrees of self-focusing by incrementally varying the defocus position over a range of input energy values, could lead us to characterising the most efficient combination of parameters to result in a higher on-shot intensity. This avenue of research would prioritise interaction efficiency before increasing energy and power further.

## THE MULTI-CHANNEL OPTICAL PROBE ON A FEMTO-SECOND LASER SYSTEM

In this chapter, the multi-channel probe is redesigned and developed for use with a femto-second laser system to investigate the evolving laser pulse propagation dynamics when interacting with a sharp density step produced by inserting a blade in the path of a supersonic gas jet of helium. This allows the flow of a jet to create a sharp, localised density gradient [112]. Depending on the position of the blade, the density gradient can lead to a number of different interaction dynamics and produce desirable conditions for electron acceleration and x-ray generation. As covered in 2, the most common use is in a down ramp position to trap and accelerate plasma electrons in the wake of a plasma wave [112], known as wavebreaking or shock-front stimulated injection (the result of which is typically a tunable monoenergetic electron beam [54]). However, unlike typical Laser-driven Wakefield Acceleration (LWFA) set ups, the experiment discussed here employs an up ramp to create a steep density gradient transition in an attempt to control bow wave formation, which leads to the generation of energetic, coherent x-rays through inducing BISER [55]. Although

this is yet to be demonstrated experimentally, PIC simulation results [55] suggest the addition of a blade in the path of a supersonic gas jet facilitates stimulated electron injection as the propagating laser pulse crosses the shock-front boundary and transitions into a high density region. If achievable experimentally, this would improve the efficiency in generating soft x-ray harmonics. The high-order harmonic generation mechanism was named "BISER" for Burst Intensification by Singularity Emitting Radiation in 2017 [34], following the first detection of soft x-ray harmonic comb-like structures, in the 60–360 eV energy range, over multiple experimental campaigns recorded on high spatial resolution spectrographs [32, 33]. Despite multiple measurements of BISER occurring in past experiments, there still remains a need for further experimental evidence demonstrating the unique features of laser-plasma interactions resulting in high-order harmonic generation due to BISER. The results that follow provide new insight into the effects of filamentation linked to self-focusing and defocus position, when BISER occurs, measured by the multi-channel probe and supported by 2D PIC simulations.

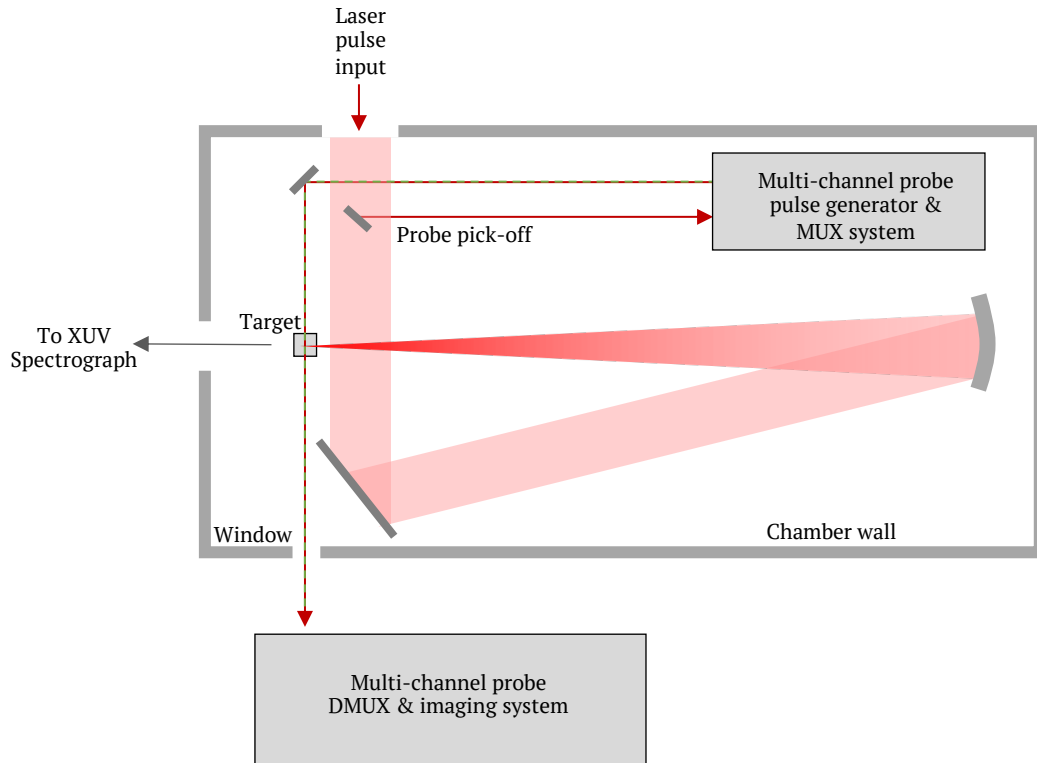


FIGURE 6.1 – Schematic of the chamber set-up from a bird’s eye view. The schematic shows the path of the interaction laser pulse to the target, and the probe pick-off line leading to the multi-channel probe pulse generator and multiplexing system. Exiting the multi-channel probe generator is a co-linear path of the probe pulses crossing perpendicularly across the path of the incoming interaction laser pulse at the target, before exiting from a chamber window to the external demultiplexing and imaging system.

## 6.1 EXPERIMENTAL METHODS

The experiment was conducted at Kansai Photon Science Institute (KPSI) in Nara, Japan, using the J-KAREN-P high power laser system. The J-KAREN-P laser is 10 TW in power, with 0.4 J pulse energy and 27 fs FWHM pulse duration, and produces a peak intensity of  $>10^{18}$  W/cm<sup>2</sup> in a spot size of 10  $\mu$ m (FWHM) when focused by the f/9 off-axis parabolic mirror. The laser pulse has a central wavelength 820 nm, and enters the vacuum chamber with a diameter of 30 cm, before being

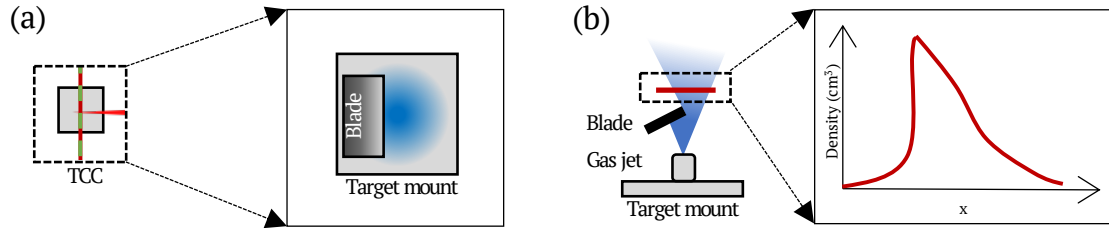


FIGURE 6.2 – (a) Zoomed in diagram of the target showing the gas jet plume and blade position from bird’s eye view. (b) Schematic of the lateral view of the blade intersecting with the gas jet plume, and a sketch of a resultant sharp density profile produced.

focused down by the OAP, as shown in Figure 6.1.

The probe pulse is picked off from the main 30 cm diameter laser pulse within the chamber using a 5 cm mirror at the periphery of the focal spot. The probe pulse is directed toward the multi-channel probe pulse generator and multiplexing system. Following this, the probe is directed perpendicularly across the interaction, and then exits the chamber to the multi-channel demultiplexing and imaging set-up. The central diagnostics in this experimental campaign are the XUV spectrometer, to confirm the presence of BISER, and the adapted multi-channel probe, to characterise the propagation and interaction dynamics. The position of the XUV spectrograph is along the laser propagation direction behind the target centre. Although the XUV spectrometer data is referenced to correlate evidence of BISER to the interaction dynamics from the multi-channel probe measurements, the adaptation, implementation and analysis of the multi-channel probe in a femtosecond laser system is the focus of this work.

At the target centre is a mount fixed with a supersonic helium gas jet and blade, as depicted in Figure 6.2(a). The blade is angled at 15 degrees to produce a steep density upward-ramp as shown in Figure 6.2(b), and to enhance the source stability of BISER. The exit nozzle of the gas jet has a diameter of 1 mm, and the laser target propagation axis is 1 mm above the nozzle exit.

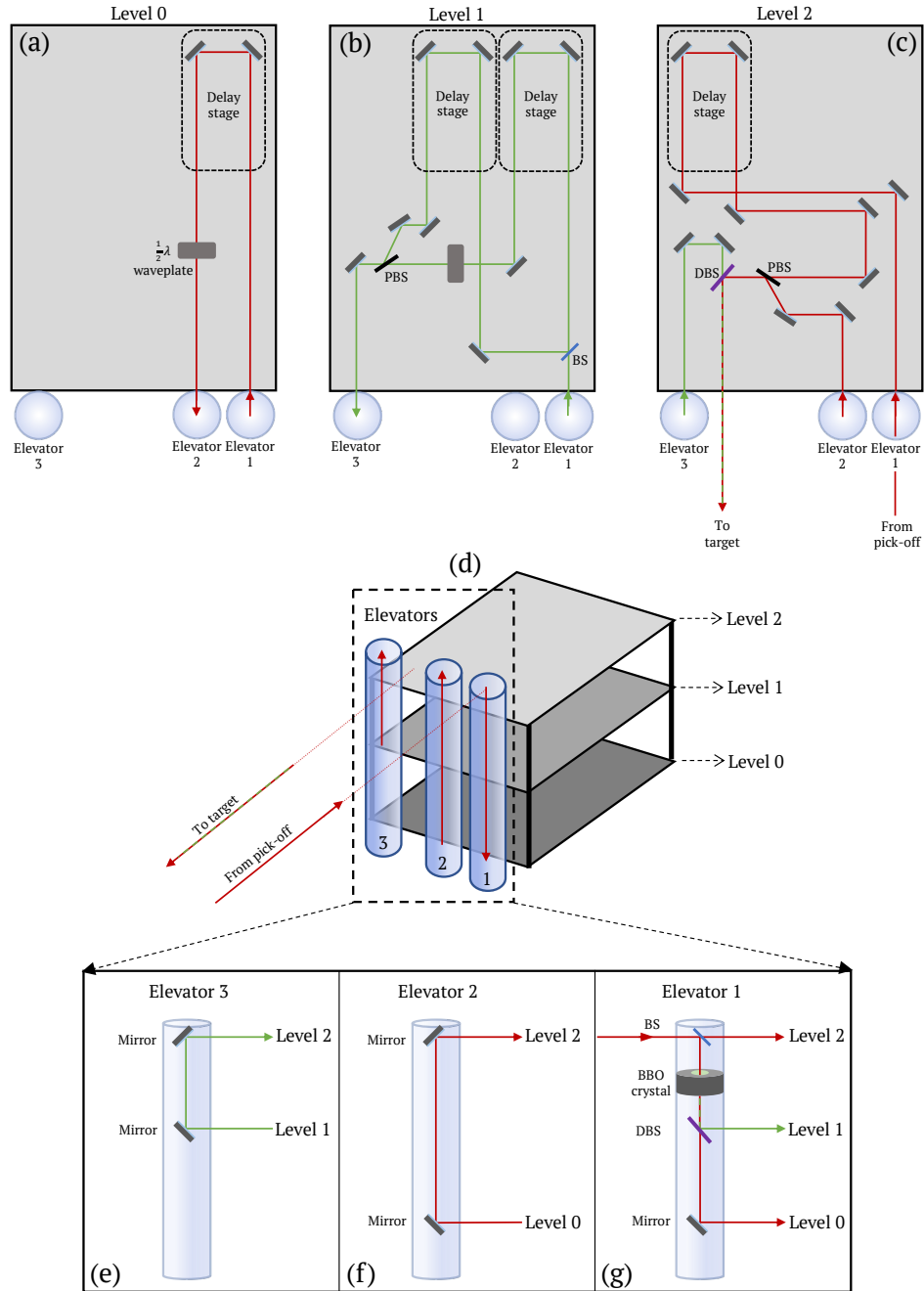


FIGURE 6.3 – Detailed schematic of the optic design on each of the multi-channel probe levels (a)  $1\omega S$  on level 0, (b)  $2\omega S$  and  $2\omega P$  on level 1, and (c)  $1\omega P$  on level 2; (d) is a schematic of the multi-channel probe levels stacked and connected by three optical elevators, the optical details of which are shown in schematic (e).

The backing pressure of the helium gas jet is varied between 1–8 MPa, producing an electron density of  $10^{19}$ – $10^{20}$   $\text{cm}^{-3}$  [33]. The defocus position of the laser relative to the target is adjusted using a step motorised positioning target stage with a resolution of  $0.5 \mu\text{m}$  (1.7 fs).

The multi-channel probe design is split over three levels due to compromising chamber space. The levels are connected by optical elevators, mirrors positioned to reflect the incoming pulse at 90 degrees without changing polarisation, as shown in Figure 6.3(d). As shown in Figure 6.3, Elevator 1 receives the incoming probe pick-off pulse, and passes it through a beamsplitter set at 45 degrees, transmitting 50 % through to level 2, and reflecting 50 % downward through a 50/50 BBO frequency doubling crystal onto a dichroic beamsplitter (DBS). There the frequency doubled light is reflected at 90 degrees onto level 1, and the  $1\omega$  light is transmitted down to the last level, where it is reflected by 90 degrees onto level 0. Elevator 2 is responsible for passing the light from level 0 back up to level 2, likewise, elevator 3 for passing the frequency doubled light from level 1 to level 2. On each level, the four pulses pass through timing delay slides and each establish individual encoding,  $1\omega\text{S}$  on level 2,  $2\omega\text{S}$  and  $2\omega\text{P}$  on level 1, and  $1\omega\text{P}$  on level 0, before being recombined on level 2. The optical design is shown in Figure 6.3, for (a) level 0, (b) level 1, and (c) level 2, and (d) shows the 3D stacking of the levels connected by optical elevators as detailed in (e), (f) and (g). Level 0, Figure 6.3(a), receives  $1\omega$  pulse with 25% that of the original pick-off intensity, from elevator 1 and is passed onto a fixed delay stage, and through a half-waveplate, becoming  $1\omega\text{P}$ . On level 1, Figure 6.3(b), the frequency doubled part of the pulse is passed through a beamsplitter and onto individual delay stages. One is then passed through a half-waveplate, becoming  $2\omega\text{S}$ , and the remaining pulse becoming  $2\omega\text{P}$ . Both  $2\omega\text{S}$  and  $2\omega\text{P}$  pulses, each with 12.5% that of the original pick-off intensity, are then recombined through a polarising beamsplitter (PBS)

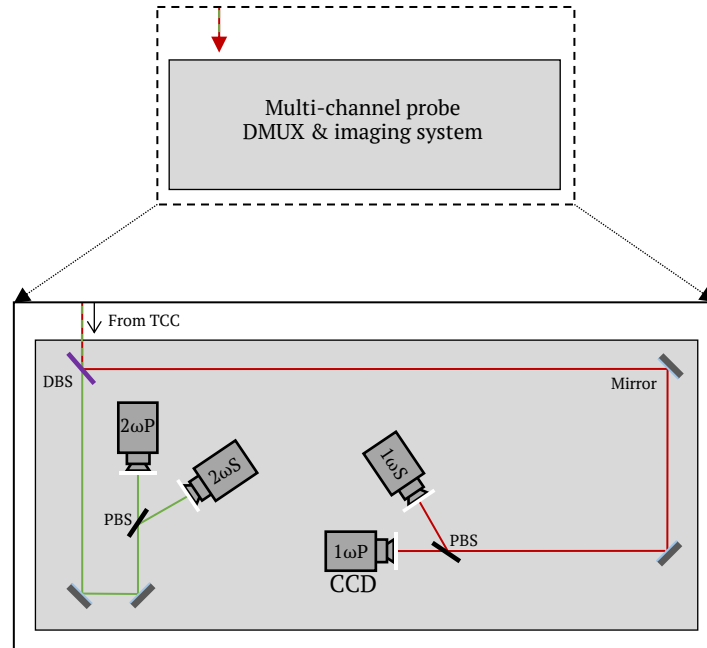


FIGURE 6.4 – Schematic of the external set-up of the multi-channel probe demultiplexing and imaging system that the probe pulses enter after exiting the chamber.

angled at 56 degrees to reflect the P-polarised pulse, and transmit the S-polarised pulse into a co-linear path. The recombined  $2\omega$  pulse is then passed to elevator 3. In Figure 6.3(c), level 2 receives the transmitted half of the original pick-off pulse, labelled as  $1\omega S$ , and passes it through a delay stage. Similar to the design of level 1, a PBS is arranged to transmit  $1\omega P$ , while reflecting the incoming  $1\omega S$  pulse from elevator 2, along the same co-linear path. A DBS is used to recombine the  $1\omega$  and  $2\omega$  pulses along a single co-linear path. Arranged at 45 degrees to the incoming  $1\omega$  pulses, the DBS reflects the  $1\omega$  pulses while transmitting the  $2\omega$  pulses from elevator 3, along one path towards the target. After the probe line passes through the target, it passes through a magnifying lens before exiting the chamber from a window, as shown in Figure 6.1. The probe pulses then enter the demultiplexing and imaging system – as depicted in Figure 6.4. The demultiplexing system employs a DBS to split the probe pulses by frequency, reflecting  $1\omega$  and transmitting  $2\omega$ . Both pulse

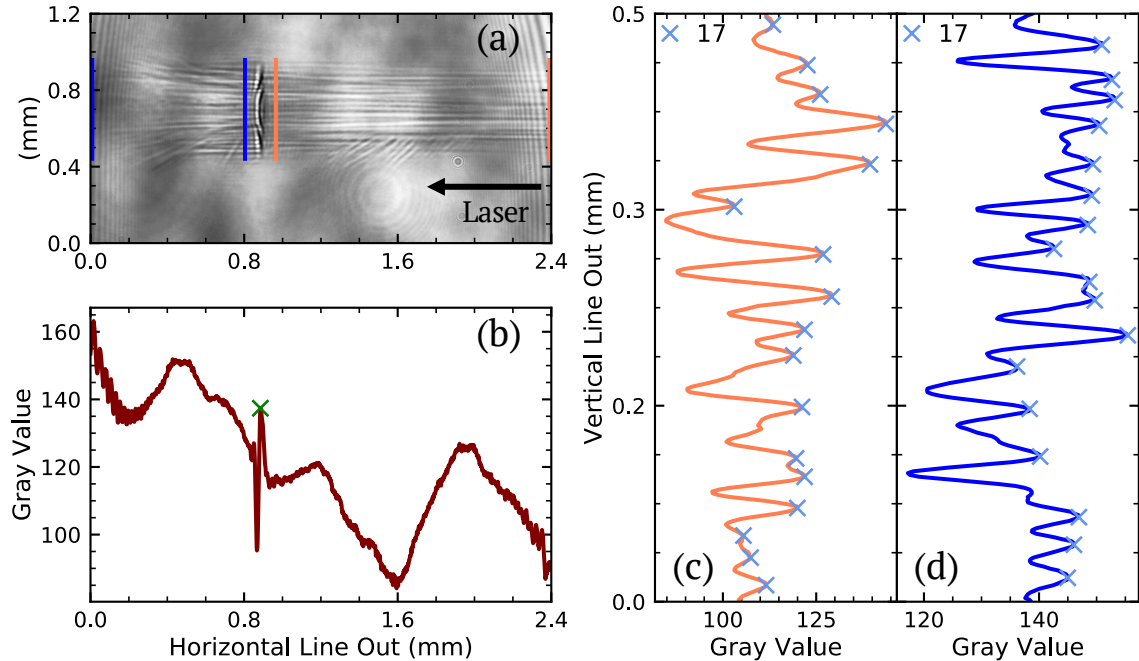


FIGURE 6.5 – Example of image analysis tool developed to (a) sum the image along the line of filamentation before the shock, between the orange markings, and after the shock, between the blue markings; (b) identify and measure the coordinates of the shock position in the image; and count the number of filaments via peak detection (c) before the shock, and (d) after the shock.

packets are then passed through PBS to split the pulses by polarisation, reflecting S-polarised light and transmitting P-polarised light, and passing each into a CCD Andor Neo Camera.

Due to delays in equipment supplies, the multi-channel probe set-up on this experimental campaign implemented three Andor Neo CCD cameras for the  $1\omega$ P,  $1\omega$ S, and  $2\omega$ S probe lines, and one Ixon CCD camera for  $2\omega$ P. Each probe image has a magnification factor of 4, providing a field of view of  $3.51 \text{ mm} \times 4.16 \text{ mm}$  in the Andor Neos, and  $3.33 \text{ mm} \times 3.33 \text{ mm}$  in the Ixon CCD. Both  $1\omega$ P and  $1\omega$ S have a resolution of  $6.5 \mu\text{m}$ . The  $2\omega$ S and  $2\omega$ P probe imaging systems have resolutions of  $3.25 \mu\text{m}$  and  $13 \mu\text{m}$ , respectively, limited by the resolution of the Ixon CCD camera.

Shown in Figure 6.5 is the output from an automated image analysis tool developed

in Python which locates and records the position of the shock imaged by multi-channel probe, and counts and records the number of filaments present either side of the shock. This was developed by analysing the patterns and characteristics of the regions of interest - the shock and the filaments. Due to limitations in image resolution and the impact noise has on the clearly identifying the filaments, a simple peak-finding function could not be used solely. The image analysis tool overcomes these limitations by following these key logical steps:

1. Input raw image.
2. Invert image.
3. Average horizontal line out through entire Y plane.
4. First derivative of average.
5. Locate shock by the point of steepest gradient.
6. Use shock coordinates as a guide to set the filament measurement sites either side of the shock.
7. Average vertical line out in front, and behind, shock separately.
8. Find and count peaks in both regions of interest.
9. Output results figures shown in Figure 6.5.

The tool begins by inverting the raw image so that the pixels of highest intensity are now the shock and the filaments. By calculating the average of the line-outs in the horizontal plane, consistent features like the shock and filaments become more prominent as a regions of high contrast in pixel count, while also minimising noise. By then taking the first derivative of this data set, the coordinates of the shock are found as the points of steepest gradient compared to neighbouring peaks, as shown

in Figure 6.5(b). Using the coordinates of the shock as a guide, the measurement sites where filaments are expected in front and behind the shock are then identified as regions of interest, as shown in Figure 6.5(a). These regions of interest are then scanned through using a peak finding function to locate and count the number of filaments Figure 6.5(c) in front of the shock, and (d) after the shock. The development of this tool was integral to the filamentation results reported in the following sections.

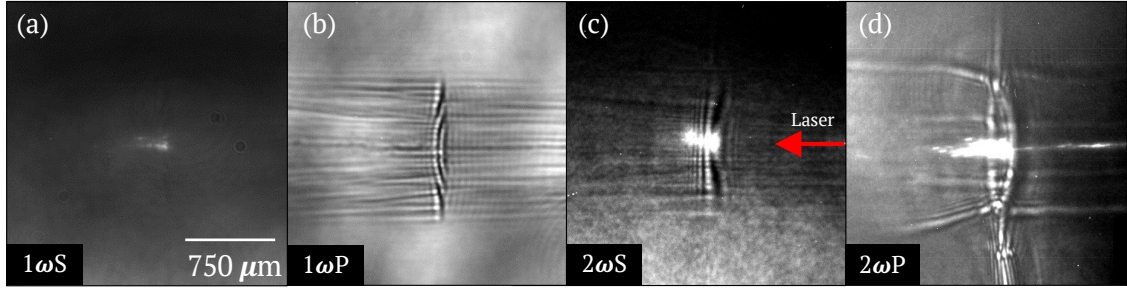


FIGURE 6.6 – Example proof of concept shadowgraphy images from the multi-channel probe integrated into a femtosecond laser system: (a)  $1\omega_S$  -370 ps, (b)  $1\omega_P$  +30 ps, (c)  $2\omega_S$  +433 ps, and (d)  $2\omega_P$  +673 ps.

## 6.2 EXPERIMENTAL RESULTS

In this section, experimental results are introduced that demonstrate the proof of concept of the adapted multi-channel probe for a femtosecond laser system, and a link measured between laser filamentation and defocus position, when a blade is inserted into a gas jet. Figure 6.6 shows an example of the multi-channel probe images obtained during the experimental campaign, where (a)  $1\omega_S$  is the earliest set channel at -370 ps before the interaction, and (b)  $1\omega_P$  is +30 ps, (c)  $2\omega_S$  is +433 ps, (d)  $2\omega_P$  is +673 ps after the interaction. In (a) we see no channel yet formed very early on at -370 ps but a small amount of self-emission which could be due to self-emission from a pre-pulse interacting with the gas jet. At 30 ps in (b) we see the shock structure formed through the main laser pulse interacting with the high density edge in the gas jet. Much later at 433 ps once the laser pulse has left, what remains in (c) is some self-emission and reduced shock structure that appears to be bending forward. Lastly in (d) at 673 ps the channel and shock structure are continuing to expand and disperse. Unfortunately, due to a delay in the arrival of the optical timing stages, two of the probe channels ( $1\omega_S$  and  $2\omega_P$ ) had fixed timings at -370 ps before, and +673 ps after, the main pulse interacts at target centre. The

analysis presented in this chapter is from one channel only,  $1\omega_P$ , due to contributing factors from self-emission disturbing the signal to noise ratio on other probe lines.

The multi-channel probe, paired with the high repetition rate of the laser system gave a movie-like insight during the experiment. As the laser energy and gas pressure were increased; the blade moving closer to the gas jet; while the target stage edging in and out of the interacting laser's focal point, the shock could be seen to expand and shrink, the number and direction of filaments and side scatter changing, and brightness of self-emission strengthening over time. Of the propagation dynamics observed and measured by the multi-channel probe, the fluctuation in filamentation either side of the shock as the target moved in and out of focus from the centre of the gas were especially intriguing.

From this defocus scan, the probe images of the interactions analysed are shown in Figure 6.7, in order of increasing defocus position (a) best focus ( $0 \mu\text{m}$ ), (b)  $+200 \mu\text{m}$ , (c)  $+800 \mu\text{m}$ , and (d)  $+1200 \mu\text{m}$ , where the XUV count exceeds 500,000; the probe timing ( $+30 \text{ ps}$ ) and blade position remain constant, and the laser energy and gas pressure are  $6.9 \pm 1.6 \text{ J}$  and  $7.1 \pm 0.5 \text{ MPa}$ . For context, the Rayleigh Range for this laser system is  $\approx 276 \mu\text{m}$ . The figure shows the change in position of the centre of the gas jet, as the target mount (gas jet and blade fixed) moves closer toward the incoming interaction laser, which, relatively, is a change in defocus position. The shock front is formed at the steep density gradient in the gas jet where the blade is fixed on the target mount. The density of the plasma at the shock front also changes with defocus position as the spot size increases and intensity of the laser pulse incident on the shock front decreases. The laser focal plane is no longer positioned at the centre of the gas jet at  $0 \mu\text{m}$  as shown in Figure 6.7(a). Relatively speaking, as the gas jet centre moves further away from the laser focal plane (fixed at  $X = 0 \mu\text{m}$ ) (a) to (d), the laser has more pre-plasma to propagate through before coming into focus

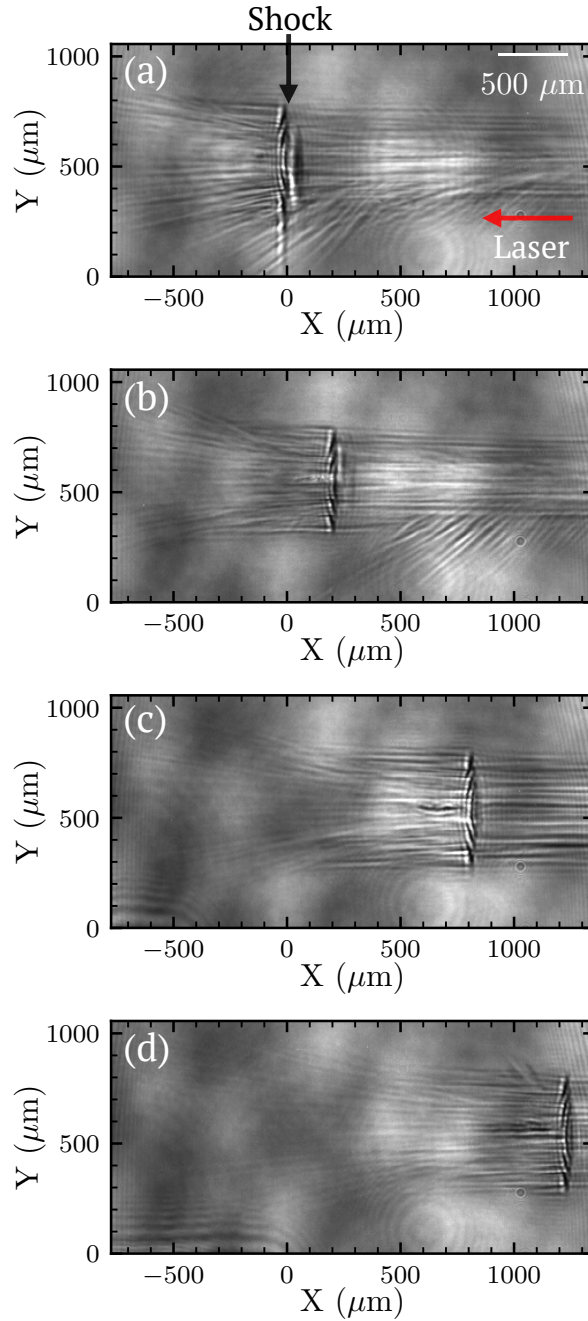


FIGURE 6.7 – Shadowgraphy images from the  $1\omega_P$  probe 30 ps after the interaction (time zero), with varying defocus positions where  $X = 0 \mu\text{m}$  represents the target mount fixed at (a) best focus, before moving toward the incoming laser pulse and therefore further away from the focal plane at  $X = 0 \mu\text{m}$  by (b)  $+200 \mu\text{m}$ , (c)  $+800 \mu\text{m}$ , and (d)  $+1200 \mu\text{m}$ .

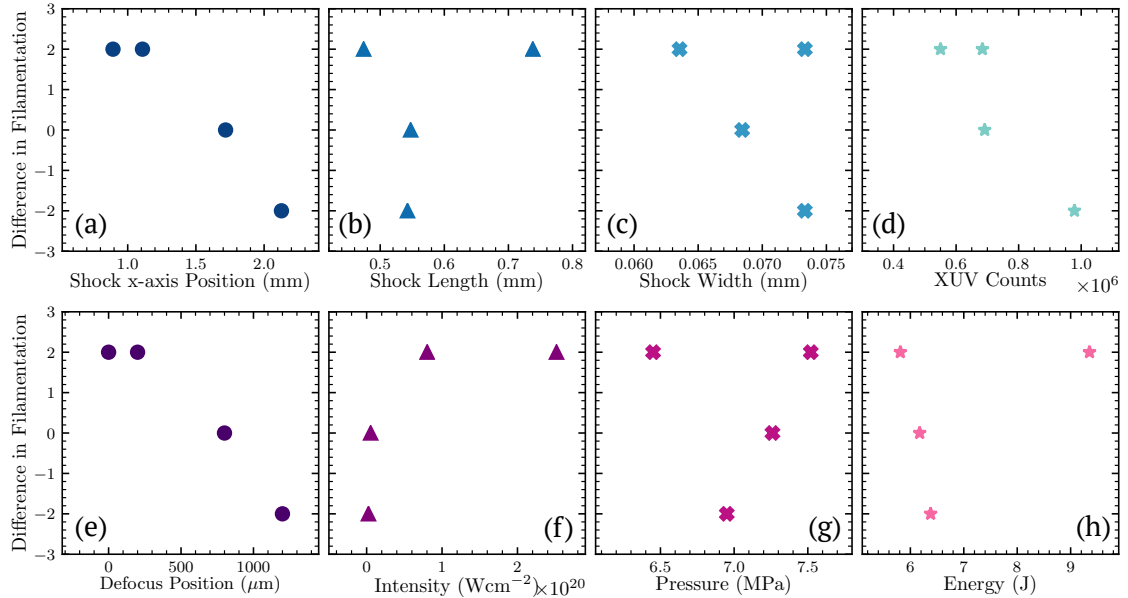


FIGURE 6.8 – The difference in filamentation measured before and after the shock with (a) shock x-axis position, (b) shock length, (c) shock width, (d) XUV counts, (e) defocus position, (f) intensity, (g) gas jet pressure, and (h) laser energy.

at  $X = 0 \mu\text{m}$ . By visual comparison, the probe images show a decrease in side scatter and turbulence as the defocus increases from (a) – (d). The degree of filamentation is quantified as the difference in the number of filaments measured before and after the shock detected by the image analysis tool introduced in Figure 6.5. A positive result indicates that more filaments have been produced after the shock than were present before, whereas a negative result indicates a loss in the number of filaments following the interaction. This analysis tool also measured the co-ordinates and dimensions of the shock.

Figure 6.8 summarises the measurements of the degree of filamentation with other experimental results and set-up parameters such as (a) shock x-axis position, (b) shock length, (c) shock width, (d) XUV counts, (e) defocus position, (f) estimated on-shot intensity, (g) gas jet pressure, and (g) laser energy. Where the degree of filamentation is the difference in the number of filaments measured before and after

the shock. In Figure 6.8(a) the difference in filamentation decreases with shock x-axis position moving upstream towards the incoming laser pulse. This is consistent with the trend of decreasing filamentation with increasing defocus position shown in Figure 6.8(e). These measurements also demonstrate the relation between the defocus and shock position previously outlined. The shock forms at the transition into the steep density gradient created by the blade regardless of the laser focal position. Therefore, it is important we account for the change in the density profile as a different part of the laser pulse interacts with density spike with increasing defocus position. As the defocus position increases, and spot size at the centre of the gas jet therefore increases, the length of the shock is measured to be increasing while decreasing in width as expected. Comparing this to the other key diagnostic in the experiment, the XUV spectrograph, Figure 6.8(d) shows the degree of filamentation decreasing with increasing XUV counts. In contrast, filamentation increases with increasing nominal intensity, at the shock position, in Figure 6.8(f). It is shown in Figure 6.8(g) and Figure 6.8(h) that there is little correlation between filamentation and pressure and energy, therefore it is deduced that the main parameter likely to be driving the change in filamentation is defocus position, and thus the change in electron density profile at these positions. Figure 6.9 takes a closer look at how the difference in filamentation, in front and behind the shock, and XUV signal vary as a function of nominal intensity in the defocus scan. The experimental results show that while the degree of filamentation increases with increasing nominal intensity, the XUV count decreases with nominal intensity. Since it is expected that the maximum XUV signal measured would be when the steep density gradient is centred at best focus [55], and therefore the XUV counts would scale directly with increasing intensity, these experimental results suggest that the intensity estimation at the centre of the gas jet at various defocus positions could be underestimated. At the defocused

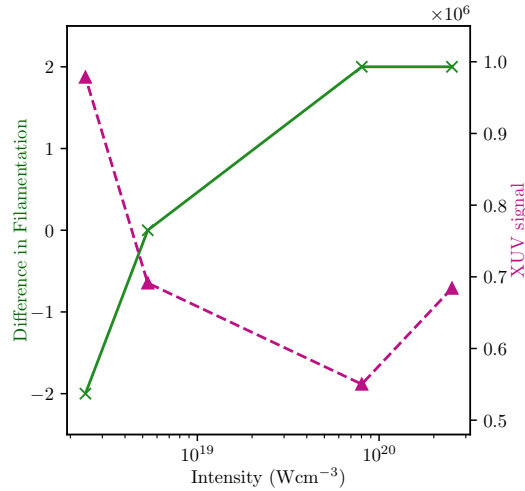


FIGURE 6.9 – The difference in filamentation as a function of nominal intensity compared with XUV counts on the secondary y-axis as a function of nominal intensity.

positions, because the laser is passing through increasing amounts of pre-plasma and interacting with a different part of the electron density profile, it is critical to consider the different effects this would have on: the filament formation either side of the shock front, and the self-focusing of the laser pulse. The unaccounted effects of self-focusing in a defocused laser pulse could explain the underestimation, but we now look to the simulation results for further investigation of self-focusing in these conditions and the relation it has to filamentation, which may also be linked to XUV strength.

### 6.3 SIMULATION RESULTS

To investigate the effects of the presence of a sharp density increase 2D PIC simulations were conducted for three set-up scenarios with the same incoming laser pulse parameters. The 2D PIC input parameters are detailed in Table 6.1.

The first of the three is the *gas jet only* case with a Gaussian approximation of the gas jet density profile; the second is the *blade* case with a simplified and symmetric up-jump ramp electron density profile added to the background Gaussian approximation electron density profile (similar to that induced by a blade positioned in the gas jet); lastly, the *no target* case is to simulate the laser propagation in vacuum without a blade or gas jet.

The three simulation scenarios allow us to gain an insight into the difference that the introduction of a blade makes over several backing pressure densities and defocus positions. Figure 6.10 shows the 2D electron density profiles of (a) gas jet only case, (b) the blade case, and (c) shows the 1D electron density profiles for both cases simulating the gas jet with and without the "blade induced" density spike.

Quantity	Value
FWHM	10 $\mu\text{m}$
Peak Intensity	$5 \times 10^{19} \text{ W/cm}^2$
Peak Density	20 $n_{\text{crit}}$
Pulse Duration	40 fs
Simulation Duration	2 ns
Ion Species	He
Initial Electron Temperature	10 keV
Mesh Size	6000 $\times$ 16000
Box Size	30 $\mu\text{m}$ $\times$ 80 $\mu\text{m}$

TABLE 6.1 – 2D PIC EPOCH simulation input parameters and values, for a laser of peak intensity  $5 \times 10^{19} \text{ W/cm}^2$  interacting with a helium gas.

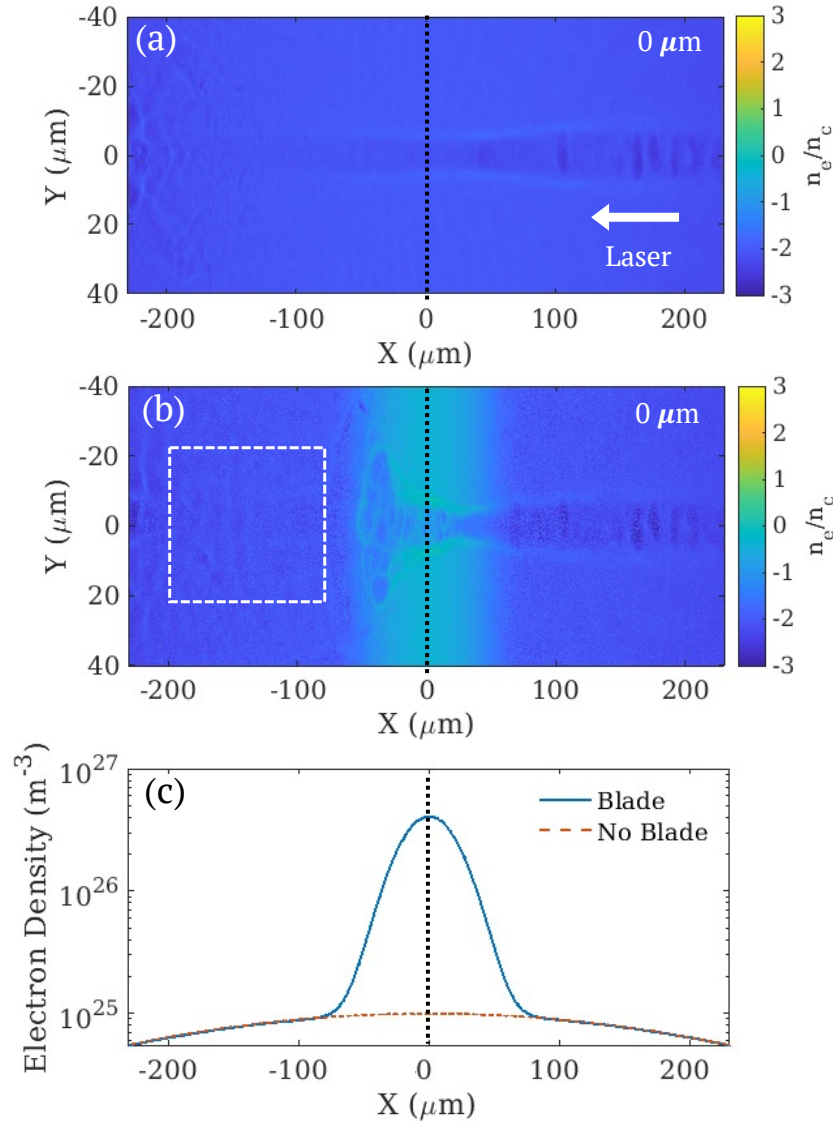


FIGURE 6.10 – 2D electron density profiles, from 2D PIC simulations, of the propagation dynamics 2 ps into the laser pulse interaction with a gas jet electron density of  $1 \times 10^{25} \text{ m}^{-3}$  at best focus, (a) without, and (b) with the blade simulated. (c) shows the electron density profiles simulating the gas jet with and without a blade inserted. The laser direction is noted on (a), and the area where the coefficient of variation is measured is shown in (b).

In each case, the electron density is varied between  $1-8 \times 10^{25} \text{ m}^{-3}$  and the defocus from  $-200 \mu\text{m}$  to  $+300 \mu\text{m}$ . Figure 6.11 shows the 2D electron density profiles of from the *blade case* at (a) best focus, (b)  $-75 \mu\text{m}$ , (c)  $+75 \mu\text{m}$ , (d)  $-125 \mu\text{m}$ , (e)  $+125$

$\mu\text{m}$ , (f)  $-200 \mu\text{m}$ , (g)  $+200 \mu\text{m}$ , and (h)  $+300 \mu\text{m}$ . By visual comparison, the region after the shock, looks more turbulent in the negative defocus position Figure 6.11(b), (d), (f), than the positive Figure 6.11(c), (e), (g). To quantify this, the coefficient of variation (CV) is calculated using Equation 6.1, where  $\sigma$  is the standard deviation and  $\mu$  is the mean, within the white square region marked in Figure 6.10(b) for all defocus positions. The results of which are represented as a percentage and plotted with defocus position in Figure 6.12.

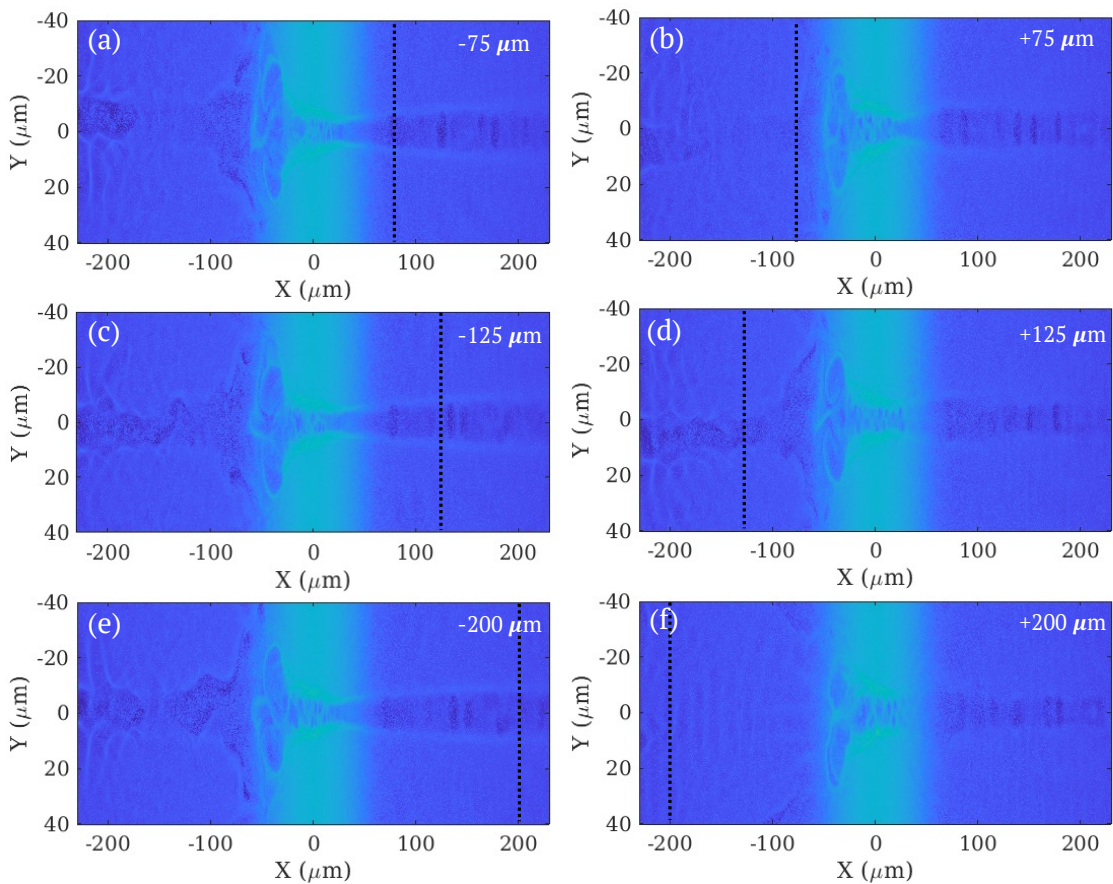


FIGURE 6.11 – 2D electron density profiles, from 2D PIC simulations, of the propagation dynamics 2 ps into the laser pulse interaction with a gas jet electron density of  $1 \times 10^{25} \text{ m}^{-3}$  and a blade simulated density jump of  $1 \times 10^{26} \text{ m}^{-3}$ , over a range of defocus positions (a)  $-75 \mu\text{m}$ , (b)  $+75 \mu\text{m}$ , (c)  $-125 \mu\text{m}$ , (d)  $+125 \mu\text{m}$ , (e)  $-200 \mu\text{m}$ , and (f)  $+200 \mu\text{m}$ . The focal plane, where the laser would be at best focus, is shown with a black dotted line and the incoming laser pulse is again from right to left.

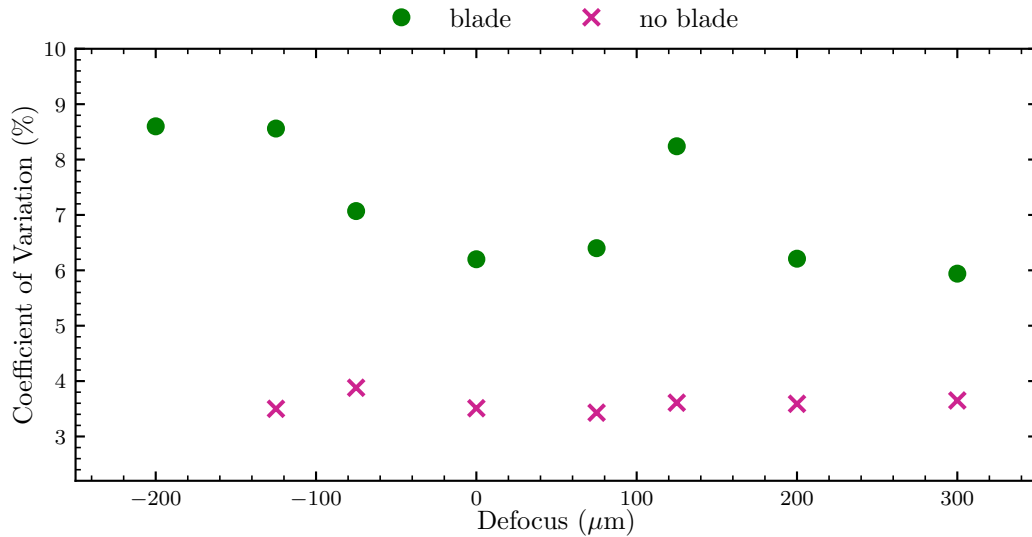


FIGURE 6.12 – Coefficient of variation with defocus position measured from the filamentation zone of 2D PIC simulations electron density plot for each simulation with varying defocus position, for the blade and no blade simulations.

$$CV = \frac{\sigma}{\mu} \quad (6.1)$$

In agreement with the visual comparison – the coefficient of variation results show an asymmetry (either side of best focus) in the turbulence measured before and after the shock with defocus position. In Figure 6.12, for the blade case, the coefficient of variation decreases from negative defocus toward best focus. However, for the same change in defocus position in the positive direction towards the incoming laser pulse, the coefficient of variation is less severe than the negative defocus, and even begins to decrease with increasing defocus beyond  $+125 \mu\text{m}$  to  $+300 \mu\text{m}$ . The turbulence at  $+300 \mu\text{m}$  is even less than that measured at best focus. These simulation results provide further evidence to suggest that the plasma turbulence and filamentation are more dominant in a negatively defocused laser and, as measured experimentally, filamentation decreases with increasing positive defocus. Although filamentation and turbulence are separate features, due to limitations in the image resolution in the

experimental probe images, the degree of filamentation is a surrogate measure of the break up of the laser beam.

To assist in our understanding of what this means in terms of intensity, Figure 6.13 compares the maximum intensity reached in the (a) gas jet only (no blade), and (b) the blade case for defocus positions  $-125 \mu\text{m}$  to  $+300 \mu\text{m}$ . In the gas jet only case, the maximum intensity increases with increasing defocus in the positive direction, but decreases with increasing defocus in the negative direction. This is most likely due to the laser pulse self-focusing more in the gas jet when there is more plasma for it to

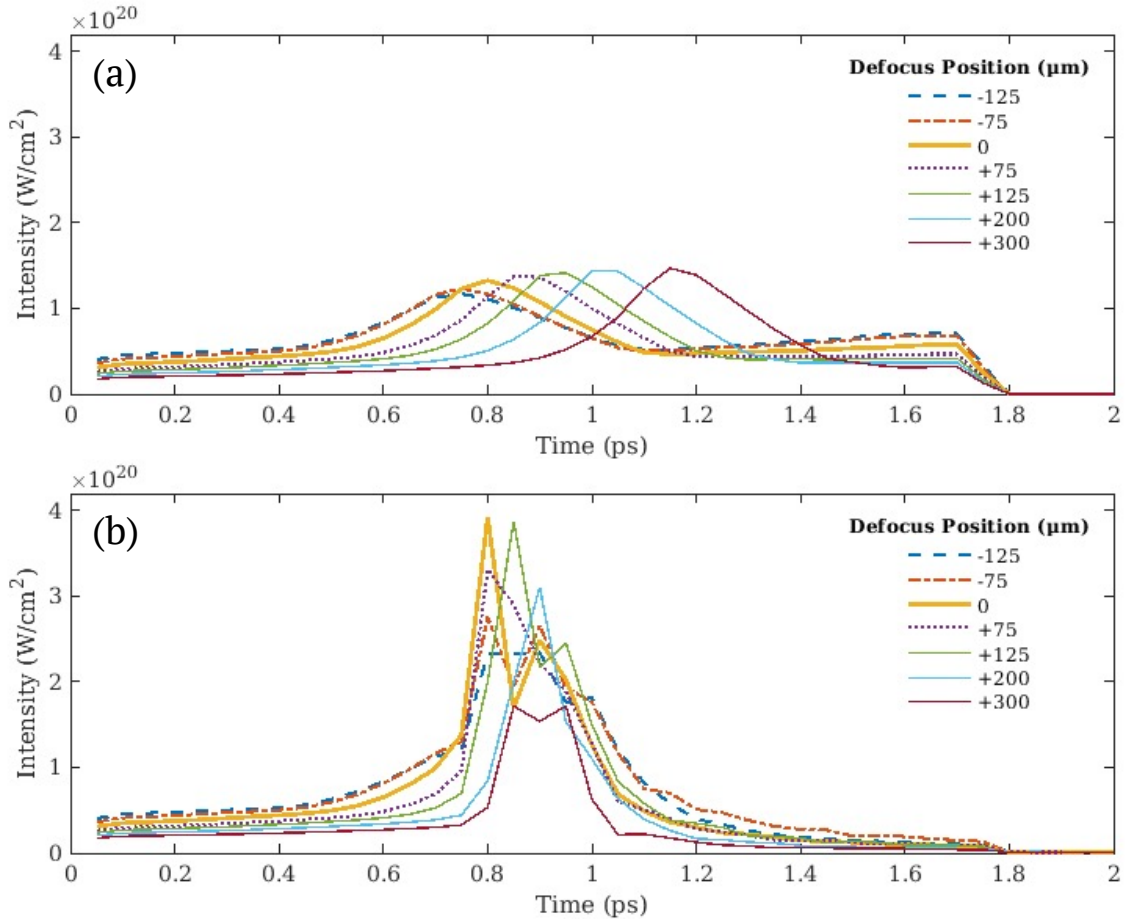


FIGURE 6.13 – Maximum intensity over the simulation time for each 2D PIC simulation at defocus positions ( $-125 \mu\text{m}$  to  $+300 \mu\text{m}$ ), (a) without, and (b) with the addition of a blade simulated in the gas jet at fixed density  $1 \times 10^{25} \text{ m}^{-3}$ .

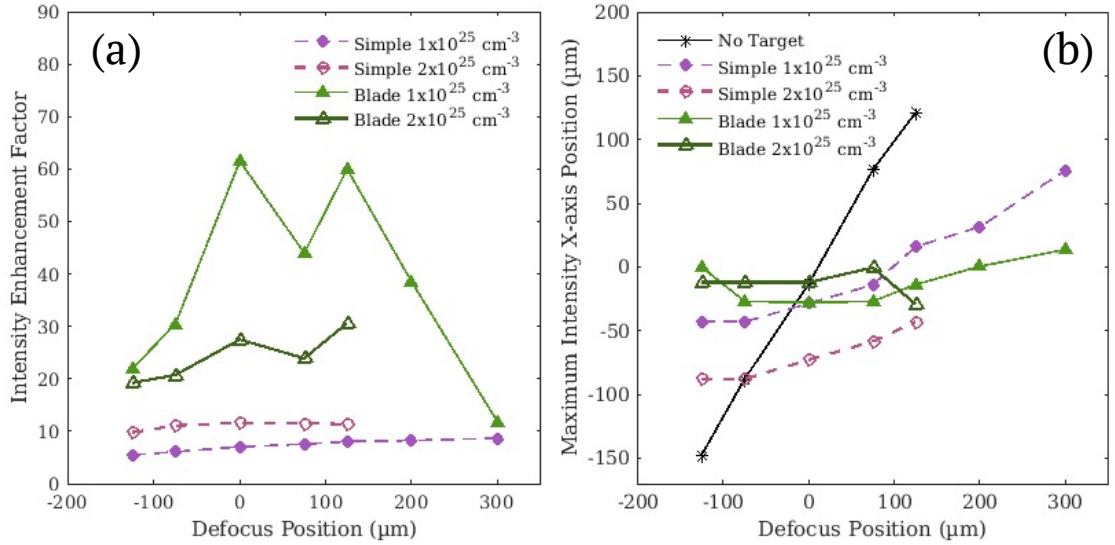


FIGURE 6.14 – 2D PIC simulation results demonstrating (a) the intensity enhancement factor, and (b) the x-axis position of the maximum intensity measured over the full simulation, with defocus position for two background densities ( $1 \times 10^{25} \text{ m}^{-3}$  and  $2 \times 10^{25} \text{ m}^{-3}$ ) with and without the addition of a blade in the gas jet path. The no blade case is labelled as the "Simple" case.

travel through before the focal plane. As expected, the time at which the maximum intensity is reached (where the pulse comes into focus) increases with positive defocus. As the focusing occurs over a larger spatial extent of plasma, the intensity is enhanced, but as a result it takes longer in time to arrive at focus. In Figure 6.13 (b), the blade case, the intensity overall is significantly greater compared to the simple gas jet only case in Figure 6.13(a) without a blade. Again, the asymmetry in intensity between positive and negative defocus can be seen. In the positively defocused cases, the timing of when the maximum intensity occurs has undergone a dramatic shift earlier than that measured in the gas jet only case in Figure 6.13(a). Furthermore, there appears to be double focal points due to the addition of the blade in the gas jet, which is symptomatic of self-focusing and scalloping behaviour. The appearance of double focal points is the behaviour of the laser pulse coming in and out and back in to focus. Notably, the intensity at a positive defocus of  $+125 \mu\text{m}$  is even comparable

to that at best focus just 0.1 ps later. These results provide further evidence that could explain the experimental findings. A positively defocused laser pulse with a blade in a gas jet, results in stronger self-focusing and less filamentation due to the laser focusing in an unperturbed pre-plasma compared to the perturbed pre-plasma that a negatively defocused laser pulse focuses through.

Figure 6.14 shows (a) the intensity enhancement factor, and (b) the x-axis position of the where the maximum intensity was measured spatially, with defocus position for the no target case, and the gas jet only and blade cases at two electron densities:  $1 \times 10^{25} \text{ m}^{-3}$  and  $2 \times 10^{25} \text{ m}^{-3}$ . The intensity enhancement factor is the maximum intensity for each simulation over all time normalised to the maximum intensity in vacuum with no gas jet or blade. The location of where the maximum intensity is spatially measured in the x-axis direction, provides us with an indication of where the laser pulse focused compared to where we would expect.

In Figure 6.14 (a), as also shown in Figure 6.13, the intensity enhancement factor decreases with increasing defocus position negatively for all densities and cases, whereas the intensity enhancement factor is notably higher when defocused positively for both densities in the blade case, especially at  $+125 \mu\text{m}$ . Similarly to the asymmetry discussed in Figure 6.13, this is due to there being no refocus when positively defocused – as the laser does not have to propagate through a perturbed plasma unlike in the negatively defocused case. For the blade case at  $2 \times 10^{25} \text{ m}^{-3}$ , beyond  $+125 \mu\text{m}$  defocus, the intensity enhancement factor decreases with further positive defocus. This decline is because at this point the laser pulse spot size (that interacts with the sharp density front of the up-jump ramp) is too large to undergo optimal plasma focusing. However, despite this decline, the intensity enhancement factor at  $+200 \mu\text{m}$  is still higher than that at  $-75 \mu\text{m}$ . Overall, the intensity is most enhanced in the blade cases, and at lower background electron density of  $1 \times 10^{25} \text{ m}^{-3}$

– as this provides a less dense pre-plasma for the laser pulse to interact with, and focus in for the first time. The higher the pressure of the gas jet, the denser the pre-plasma, the sooner in time, and spatial x-axis position, that the pulse will focus.

In Figure 6.14(b), the y-axis represents the x-axis position in space as depicted in the 2D simulation plots in Figure 6.11. The positive position is towards the incoming laser pulse, and positive defocus, likewise the negative position is in the negative defocus direction. The no target case demonstrates the change in focal position as it moves with the laser becoming positively and negatively defocused. In vacuum, with no gas or pre-plasma to focus in, the no target case provides us with a benchmark in the x-axis position of the focal planes that we can then compare the change in focal positions for the gas jet only, and blade cases with. With the introduction of the helium, in the gas jet only cases, the focal position continues to follow the same trend with defocus position as the no target case, but focuses closer to best focus due to self-focusing in the plasma. As expected, this becomes stronger for the higher electron density. The higher the gas target pressure, and therefore electron density, the sooner the laser pulse will undergo self-focusing; and in the case for the blade, too high an electron density results in the pulse undergoing self-focusing before reaching the density spike induced by the blade. In Figure 6.13(b), for the blade cases, all defocus positions come into focus, and reach a maximum intensity, much closer to the vacuum best focus position. When comparing between the gas jet only and blade case for  $1 \times 10^{25} \text{ m}^{-3}$  density, the shift in position where the pulse focuses more strongly due to the addition of the blade is clear. This is further evidence of strong self-focusing as a result of the steep density gradient, induced by the presence of a blade. These simulations confirm that the self-focusing is occurring, and that the on-shot intensities estimated for the experimental results are underestimated as they do not account for the difference in focusing through unperturbed or perturbed

plasma and the difference this makes to intensity enhancement and the focal plane position.

## 6.4 SUMMARY AND CONCLUSION

In this chapter we have explored the physics linking filamentation and defocus position to the degree of self-focusing in a gas jet with a density up-ramp. Experimentally, we found that filamentation decreases with increasing positive defocus and also increasing XUV generation. Framing filamentation as beam break up and energy loss, the experimental results suggest that the laser-plasma interaction becomes more energy efficient as the laser is defocused more positively. Simulating a similar set-up, including negative defocus positions also, the 2D PIC simulations went on to mirror this finding that turbulence decreases with increasing positive defocus, and furthermore, increases with increasing negative defocus.

From this it could be understood that in positive defocus, the laser pulse has an unperturbed plasma to self-focus through from the first time whereas, when negatively defocused, the plasma is already perturbed as the pulse is undergoing a refocus. From understanding the impact that defocus position can have on plasma turbulence, and perhaps to the benefit of XUV generation, especially in the case where a blade is simulated in the gas jet, the simulation analysis then looks to the impact this has on intensity enhancement. The results demonstrated the intensity enhancement achievable with a positively defocused laser, self-focusing through an unperturbed plasma and getting an additional enhancement from the density ramp.

Looking forward, this work could be developed further by simulating a more realistic, and asymmetric, density spike which will be closer to that induced by the blade experimentally. Future experimental and simulation research could also

include exploring the difference an up or down-ramp makes to the strength of self-focusing. Applying the same experimental analysis and filamentation analysis tool to all channels of the multi-channel probe will provide a deeper understanding of the time frame in which filaments grow or converge, and how this relates to the time of where maximum intensity is reached. The filamentation tool itself could also be developed further if the multi-channel probe imaging technique was adapted for interferometry. The multi-channel probe opens up many further research opportunities to temporally and spatially measure the filamentary structures explored in simulations.

Overall finding the optimal positive defocus position, and background density, could allow us to induce one single optimised self-focusing event through an unperturbed plasma while incurring minimal energy loss through filamentation growth, which may have benefits on XUV generation, through BISER.

## SUMMARY AND PERSPECTIVES

Throughout this thesis we have discussed the development and implementation of a novel multi-channel probe in multiple high-power laser-plasma experiments, and the new insights into plasma dynamics that were measured for the first time, as a result. Now we reflect back on the three results chapters by summarising the key findings reported, and what exciting avenues this research may lead us to going forward.

### 7.1 THE MULTI-CHANNEL PROBE

In chapter 4 we first explored the scientific and technological milestones in temporal imaging that led to the pump-probing technique being employed in laser-plasma experiments. We outlined the need for a diagnostic that can provide sufficient temporal, and spatial, resolution to probe a single laser-pulse interaction. Following this, the multi-channel probe concept and its many sources of inspiration, namely Eadward Muybridge's horse analogy, were introduced. We discussed the development of the multi-channel probe from concept into a practical optical design, and how it

was then implemented into a high power laser experiment for the first time, and the first results probing underdense plasma that followed this.

Using the multi-channel probe on the TAW arm of the Vulcan laser system at peak intensity of  $1 \times 10^{18}$  W/cm<sup>2</sup>, the evolution of channel formation in underdense plasma was investigated over 217 ps. When comparing these proof of concept results to 2D PIC simulations with the same laser-plasma parameters, the results showed differences in the early onset of channel formation and beam filamentation. The difference ultimately demonstrates that the intra-interaction dynamics that occur cannot be understood by simulations alone, or by a timing scan built from repeated single-shot probe images in inconsistent conditions. A new approach, such as the multi-channel probe, is needed to provide additional insight.

Lastly we investigated the channel formation measured by the multi-channel probe while increasing the pressure of the helium gas jet from 20–100 bar. From these shadowgraphs the channel gradient could be measured at each pressure, which is indicative of the degree of self-focusing that the laser pulse is undergoing. The results suggested that the channel gradient (degree of self-focusing) increases with gas pressure, and moreover, so does the rate of self-focusing. Capturing the change in channel gradient with time is the first measurement of its kind using the multi-channel probe. This chapter demonstrated the development, implementation, and proof of concept of the multi-channel probe as well as exploring just some of the advantages it offers as a route to better understanding the evolving dynamics within a single laser-plasma interaction.

## 7.2 THE MULTI-CHANNEL PROBE MEASURING FRONT SURFACE DYNAMICS

In chapter 5 the multi-channel probe was used to investigate if, and how, the front-surface conditions of 20  $\mu\text{m}$  Copper targets change depending on the method in which on-shot intensity is controlled: by laser energy and defocus position. The experimental results discussed were from the TAW Vulcan experimental campaign which delivered laser pulses with peak intensities up to mid  $10^{19}$   $\text{W}/\text{cm}^2$ .

Here the multi-channel probe demonstrated that there is a difference in the front surface conditions depending on the method of intensity control. The front surface conditions were compared through contour analysis, and quantified by measurements of the longitudinal and transverse plasma expansion over time. The results in this chapter gave evidence to suggest that a change in the method of intensity control, alters the front surface conditions and rate of plasma expansion, which subsequently effects the interaction dynamics – evident in the RCF, back-scatter spectra, and supported by 2D EPOCH particle-in-cell simulations.

When comparing the behaviour of the plasma when laser energy varied and defocus position varied, the findings suggest that by defocusing the laser pulse, the severity of self-focusing and therefore on-target intensity is enhanced by the preformed plasma on the front side of the target. Unexpected results also suggest that there is an asymmetry to this enhancement either side of best focus due to wavefront matching with the contour of the preplasma expansion on the target front side.

This chapter demonstrated that, ultimately, it matters how intensity is controlled, and that self-focusing can be induced when one approach is taken over another.

### 7.3 THE MULTI-CHANNEL PROBE AND FILAMENTATION WHEN A BLADE IS INSERTED INTO A GAS JET

Lastly, in chapter 6, the multi-channel probe design is adapted for use on the femto-second laser system J-KAREN-P, in a considerably more compact chamber space than the experimental set-ups reported in the two preceding results chapters. Here we discussed the considerations taken in this design, the challenges in the set-up, and the role of the multi-channel probe in this underdense plasma experiment that investigates the effect of inserting a blade into a supersonic helium gas jet.

The results of this chapter demonstrate a new found correlation between filamentation and self-focusing with a positively defocused laser pulse. The multi-channel probe results and 2D EPOCH particle-in-cell simulations demonstrate a reduction in filamentation as the laser is defocused positively. This is explained by the difference in preplasma conditions where a negatively defocused laser pulse undergoes a refocus in an already perturbed plasma, whereas a positively defocused laser pulse can optimise self-focusing in one focusing event in unperturbed plasma.

This chapter suggests that by minimising energy loss through filamentation, the on-shot intensity can be enhanced which can lead to a boost in XUV production via BISER, and other high intensity dependent mechanisms. However, further work is required to establish if there is a correlation between XUV generation and filamentation.

## 7.4 REFLECTIONS AND FUTURE WORK

Central to this thesis is the development of the multi-channel probe. We have discussed the sources that inspired the multi-channel probe, and the necessity for a single-shot imaging diagnostic, such as this, with sufficient spatial and user-defined temporal resolution in laser-plasma experiments.

The multi-channel probe has been designed and successfully implemented into two different high power laser systems, the picosecond Vulcan laser at RAL and the femtosecond J-KAREN-P laser at KPSI. The technique has measured the evolving laser-plasma dynamics in both underdense and overdense plasma. The overarching theme of this thesis is towards understanding when self-focusing occurs and what laser and plasma parameters it depends upon in a variety of experimental set-ups. With this knowledge, we could more accurately predict when the actual laser intensity is likely to be higher than the nominal laser intensity, which could lead us an enhancement of on-target intensity by optimising when self-focusing occurs. The multi-channel probe has been key in providing this insight for all investigations reported here, as it was the subtle changes it measured in the channel formation, preplasma perturbations, and filamentation that lead to a better understanding of the dynamics at play.

Looking forward towards the future of the multi-channel probe in laser-plasma experiments, it would be beneficial to compact the design into a portable optical system that is compatible with a wide range of high-power laser systems. Ideally this would comprise of two standalone sections, the multiplexing and polarisation encoding system for inside the target vacuum chamber, and the demultiplexing system for separating the pulses for imaging outside of the chamber. The optics within the portable multi-channel probe system would be fixed so the user would just have to align their input probe laser pulse in one end, and have an optic too

receive and redirect the encoded co-linear pulses at the other end towards their target centre. This would save the user chamber space and set-up time, while giving them a temporal insight into their interactions. If the multi-channel probe system became a standard imaging diagnostic in the laser-plasma community, our understanding of the ultra-fast dynamics evolving within our experiments would deepen, and our experimental measurements would better complement the evolving simulation investigations of plasma dynamics. Future adaptations could look to increase the temporal resolution of the multi-channel probe by increasing the number of channels, and therefore encoding patterns, or by choosing a delay stage with minimal spacing – since the temporal resolution is dependent on the staggering of the probe pulses that translates to a physical change in path length. However, there are limiting factors to be considered such as: the pulse length of the probe pulse; the accuracy and mechanical, positional error within the delay stage motors; the possibility of cross-talk between channels if the polarisation encoding reduces below 90 degrees separation; and ultimately, the diffraction limit.

To conclude, the future possibilities in applications and developments of the multi-channel probe are promising. This novel diagnostic has been shown to offer a flexible and reliable insight into single laser-plasma interaction events, enhancing our understanding of the interaction dynamics.

## BIBLIOGRAPHY

- [1] J. Wade. *Why we need to keep talking about equality in physics*. [HTTPS://PHYSICSWORLD.COM/A/WHY-WE-NEED-TO-KEEP-TALKING-ABOUT-EQUALITY-IN-PHYSICS/](https://physicsworld.com/a/why-we-need-to-keep-talking-about-equality-in-physics/). 2019.
- [2] D. Batty. *Uk universities condemned for failure to tackle racism*. [HTTPS://WWW.THEGUARDIAN.COM/EDUCATION/2019/JUL/05/UK-UNIVERSITIES-CONDEMNED-FOR-FAILURE-TO-TACKLE-RACISM](https://www.theguardian.com/education/2019/jul/05/uk-universities-condemned-for-failure-to-tackle-racism). 2019.
- [3] D. Batty. *More than half of uk students say they have faced unwanted sexual behaviour*. [HTTPS://WWW.THEGUARDIAN.COM/EDUCATION/2019/FEB/26/MORE-THAN-HALF-OF-UK-STUDENTS-SAY-THEY-HAVE-FACED-UNWANTED-SEXUAL-BEHAVIOUR](https://www.theguardian.com/education/2019/feb/26/more-than-half-of-uk-students-say-they-have-faced-unwanted-sexual-behaviour). 2019.
- [4] V. Jamieson. *Women in physics: why there's a problem and how we can solve it*. [HTTPS://WWW.NEWSIDENTIST.COM/ARTICLE/MG24032031-900-WOMEN-IN-PHYSICS-WHY-THERES-A-PROBLEM-AND-HOW-WE-CAN-SOLVE-IT/](https://www.newscientist.com/article/mg24032031-900-women-in-physics-why-theres-a-problem-and-how-we-can-solve-it/). 2018.
- [5] M. Allen. *Gender gap in physics among highest in science*. [HTTPS://PHYSICSWORLD.COM/A/GENDER-GAP-IN-PHYSICS-AMONGST-HIGHEST-IN-SCIENCE/](https://physicsworld.com/a/gender-gap-in-physics-amongst-highest-in-science/). 2018.

- [6] J. Lee. *6 women scientists who were snubbed due to sexism*. [HTTPS://WWW.NATIONALGEOGRAPHIC.COM/CULTURE/ARTICLE/130519-WOMEN-SCIENTISTS-OVERLOOKED-DNA-HISTORY-SCIENCE](https://www.nationalgeographic.com/culture/article/130519-women-scientists-overlooked-dna-history-science). 2013.
- [7] K. Powell. *Academia's ableist mindset needs to change*. [HTTPS://WWW.NATURE.COM/ARTICLES/D41586-021-02907-7](https://www.nature.com/articles/d41586-021-02907-7). 2021.
- [8] N. Ackerman et al. *Lgbt+ inclusivity in physics and astronomy: a best practices guide*. 2018. arXiv: [1804.08406](https://arxiv.org/abs/1804.08406) [[physics.ed-ph](https://arxiv.org/abs/1804.08406)].
- [9] W.I. Linlor. "Ion energies produced by laser giant pulse". In: *Applied physics letters* 3 (1963). DOI: [10.1063/1.1753852](https://doi.org/10.1063/1.1753852).
- [10] W.I. Linlor. "Some properties of plasma produced by laser giant pulse". In: *Physical review letters* 12 (1964). DOI: [10.1103/PHYSREVLETT.12.383](https://doi.org/10.1103/PhysRevLett.12.383).
- [11] T. Tajima and J. M. Dawson. "Laser electron accelerator". In: *Phys. rev. lett.* 43 (4 1979), pp. 267–270. DOI: [10.1103/PHYSREVLETT.43.267](https://doi.org/10.1103/PhysRevLett.43.267).
- [12] R.G. Gould. "The laser, light amplification by stimulated emission of radiation". In: *The ann arbor conference on optical pumping* 15 (1959).
- [13] T.H. Maiman. "Maser behavior: temperature and concentration effects". In: *Journal of applied physics* 31 (1960). DOI: [10.1063/1.1735412](https://doi.org/10.1063/1.1735412).
- [14] S. Cipiccia et al. "Gamma-rays from harmonically resonant betatron oscillations in a plasma wake". In: *Nature physics* 7 (2011). DOI: [10.1038/NPHYS2090](https://doi.org/10.1038/NPHYS2090).
- [15] C. Joshi et al. "Ultrahigh gradient particle acceleration by intense laser-driven plasma density waves". In: *Nature* 311 (1984). DOI: [10.1038/311525A0](https://doi.org/10.1038/311525A0).
- [16] D.A. Jaroszynski et al. "Radiation sources based on laser-plasma interactions". In: *Phil. trans. r. soc. a.* 364 (2006). DOI: [10.1098/RSTA.2005.1732](https://doi.org/10.1098/RSTA.2005.1732).

- [17] S.J. Moon et al. “A neutron star atmosphere in the laboratory with petawatt lasers”. In: *Astrophys space sci* 298 (2005). DOI: [10.1007/s10509-005-3949-6](https://doi.org/10.1007/s10509-005-3949-6).
- [18] D. Strickland and G. Mourou. “Compression of amplified chirped optical pulses”. In: *Optics communications* 56.3 (1985). DOI: [10.1016/0030-4018\(85\)90120-8](https://doi.org/10.1016/0030-4018(85)90120-8).
- [19] I.N. Ross et al. “The prospects for ultrashort pulse duration and ultrahigh intensity using optical parametric chirped pulse amplifiers”. In: *Optics communications* 144 (1997). DOI: [10.1016/S0030-4018\(97\)00399-4](https://doi.org/10.1016/S0030-4018(97)00399-4).
- [20] A. Boné et al. “Quantitative shadowgraphy for laser-plasma interactions”. In: *Journal of physics d: applied physics* 49 (2016). DOI: [10.1088/0022-3727/49/15/155204](https://doi.org/10.1088/0022-3727/49/15/155204).
- [21] M. Börner et al. “Development of a nomarski-type multi-frame interferometer as a time and space resolving diagnostic for the free electron density of laser-generated plasma”. In: *Review of scientific instruments* 83.4 (2012). DOI: [10.1063/1.3701366](https://doi.org/10.1063/1.3701366).
- [22] R. Benattar, C. Popovics, and R. Sigel. “Polarized light interferometer for laser fusion studies”. In: *Review of scientific instruments* 50.12 (1993). DOI: [10.1063/1.1135764](https://doi.org/10.1063/1.1135764).
- [23] Z. Najmudin et al. “The effect of high intensity laser propagation instabilities on channel formation in underdense plasmas”. In: *Physics of plasmas* 10.2 (2003). DOI: [10.1063/1.1534585](https://doi.org/10.1063/1.1534585).
- [24] A. J. Gonsalves et al. “Tunable laser plasma accelerator based on longitudinal density tailoring”. In: *Nature physics* 7.11 (2011). DOI: [10.1038/NPHYS2071](https://doi.org/10.1038/NPHYS2071).
- [25] J. Liang and L. V. Wang. “Single-shot ultrafast optical imaging”. In: *Optica* 5.9 (2018). DOI: [10.1364/OPTICA.5.001113](https://doi.org/10.1364/OPTICA.5.001113).

- [26] Z. Li et al. “Single-shot visualization of evolving plasma wakefields”. In: *Aip conference proceedings* 1777.1 (2016). DOI: [10.1063/1.4965612](https://doi.org/10.1063/1.4965612).
- [27] S. P. D. Mangles et al. “On the stability of laser wakefield electron accelerators in the monoenergetic regime”. In: *Physics of plasmas* 14.5 (2007). DOI: [10.1063/1.2436481](https://doi.org/10.1063/1.2436481).
- [28] S. P. D. Mangles et al. “Monoenergetic beams of relativistic electrons from intense laser–plasma interactions”. In: *Nature* 431 (2004). DOI: [10.1038/NATURE02939](https://doi.org/10.1038/NATURE02939).
- [29] P. R. Poulin and K. A. Nelson. “Irreversible organic crystalline chemistry monitored in real time”. In: *Science* 313.5794 (2006). DOI: [10.1126/SCIENCE.1127826](https://doi.org/10.1126/SCIENCE.1127826).
- [30] D. Grossmann et al. “Transverse pump-probe microscopy of moving breakdown, filamentation and self-organized absorption in alkali aluminosilicate glass using ultrashort pulse laser”. In: *Optics express* 24.20 (2016). DOI: [10.1364/OE.24.023221](https://doi.org/10.1364/OE.24.023221).
- [31] Z. E. Davidson et al. “An optically multiplexed single-shot time-resolved probe of laser-plasma dynamics”. In: *Optics express* 27.4 (2019). DOI: [10.1364/OE.27.004416](https://doi.org/10.1364/OE.27.004416).
- [32] A. S. Pirozhkov et al. “Soft-x-ray harmonic comb from relativistic electron spikes”. In: *Phys. rev. lett.* 108 (13 2012), p. 135004. DOI: [10.1103/PHYSREVLETT.108.135004](https://doi.org/10.1103/PHYSREVLETT.108.135004).
- [33] A. S. Pirozhkov et al. “High order harmonics from relativistic electron spikes”. In: *New journal of physics* 16 (2014). DOI: [10.1088/1367-2630/16/9/093003](https://doi.org/10.1088/1367-2630/16/9/093003).
- [34] A. Pirozhkov et al. “Approaching the diffraction-limited, bandwidth-limited petawatt”. In: *Optics express* 25 (2017). DOI: [10.1364/OE.25.020486](https://doi.org/10.1364/OE.25.020486).

- [35] J. Wang et al. “Over-barrier ionization of hydrogen atom in intense circular and elliptical laser fields”. In: *Frontiers in physics* 10 (2022). DOI: [10.3389/fphy.2022.976734](https://doi.org/10.3389/fphy.2022.976734).
- [36] E. Esarey et al. “Self-focusing and guiding of short laser pulses in ionizing gases and plasmas”. In: *Ieee journal of quantum electronics* 33.11 (1997). DOI: [10.1109/3.641305](https://doi.org/10.1109/3.641305).
- [37] R. S. Craxton et al. “Direct-drive inertial confinement fusion: a review”. In: *Physics of plasmas* 22.11 (2015). DOI: [10.1063/1.4934714](https://doi.org/10.1063/1.4934714).
- [38] C. Yu et al. “Study of channel formation and relativistic ultra-short laser pulse propagation in helium plasma”. In: *Plasma physics and controlled fusion* 58.5 (2016), p. 055007. DOI: [10.1088/0741-3335/58/5/055007](https://doi.org/10.1088/0741-3335/58/5/055007).
- [39] K. Keshav Walia, D. Tripathi, and Y. Tyagi. “Investigation of weakly relativistic ponderomotive effects on self-focusing during interaction of high power elliptical laser beam with plasma”. In: *Communications in theoretical physics* 68.2 (2017), p. 245. DOI: [10.1088/0253-6102/68/2/245](https://doi.org/10.1088/0253-6102/68/2/245).
- [40] A. G. Litvak. “Finite-amplitude wave beams in a magnetoactive plasma”. In: *Zh. eksp. teor. fiz.* 30 (1969).
- [41] C. E. Max, J. Arons, and A. B. Langdon. “Self-modulation and self-focusing of electromagnetic waves in plasmas”. In: *Phys. rev. lett.* 33 (4 1974), pp. 209–212. DOI: [10.1103/PhysRevLett.33.209](https://doi.org/10.1103/PhysRevLett.33.209).
- [42] C. Joshi et al. “Direct observation of laser beam filamentation in an underdense plasma”. In: *Journal of applied physics* 53.1 (1982), pp. 215–217. DOI: [10.1063/1.331595](https://doi.org/10.1063/1.331595).

- [43] R. L. Berger et al. “Theory and three-dimensional simulation of light filamentation in laser-produced plasma”. In: *Physics of fluids b: plasma physics* 5.7 (1993), pp. 2243–2258. DOI: [10.1063/1.860758](https://doi.org/10.1063/1.860758).
- [44] J. B. Rosenzweig et al. “Experimental observation of plasma wake-field acceleration”. In: *Physical review letters* 61 (1988). DOI: [10.1103/PhysRevLett.61.98](https://doi.org/10.1103/PhysRevLett.61.98).
- [45] E. Esarey, C. B. Schroeder, and W. P. Leemans. “Physics of laser-driven plasma-based electron accelerators”. In: *Rev. mod. phys.* 81 (3 2009), pp. 1229–1285. DOI: [10.1103/RevModPhys.81.1229](https://doi.org/10.1103/RevModPhys.81.1229).
- [46] J. M. Dawson. “Nonlinear electron oscillations in a cold plasma”. In: *Phys. rev.* 113 (2 1959), pp. 383–387. DOI: [10.1103/PhysRev.113.383](https://doi.org/10.1103/PhysRev.113.383).
- [47] R. M. G. M. Trines and P. A. Norreys. “Wave breaking limits for relativistic electrostatic waves in a warm plasma”. In: *Central laser facility annual report* (2005).
- [48] J. P. Palastro et al. “Dephasingless laser wakefield acceleration”. In: *Phys. rev. lett.* 124 (13 2020), p. 134802. DOI: [10.1103/PhysRevLett.124.134802](https://doi.org/10.1103/PhysRevLett.124.134802).
- [49] C. B. Schroeder et al. “Trapping, dark current, and wave breaking in nonlinear plasma waves”. In: *Physics of plasmas* 13.3 (2006), p. 033103. DOI: [10.1063/1.2173960](https://doi.org/10.1063/1.2173960).
- [50] J. Faure, C. Rechatin, and A. et al Norlin. “Controlled injection and acceleration of electrons in plasma wakefields by colliding laser pulses”. In: *Nature* 444 (2006). DOI: [10.1038/NATURE05393](https://doi.org/10.1038/NATURE05393).
- [51] D. Umstadter, J. K. Kim, and E. Dodd. “Laser injection of ultrashort electron pulses into wakefield plasma waves”. In: *Phys. rev. lett.* 76 (12 1996), pp. 2073–2076. DOI: [10.1103/PhysRevLett.76.2073](https://doi.org/10.1103/PhysRevLett.76.2073).

- [52] S. Bulanov et al. “Particle injection into the wave acceleration phase due to nonlinear wake wave breaking”. In: *Phys. rev. e* 58 (5 1998). DOI: [10.1103/PhysRevE.58.R5257](https://doi.org/10.1103/PhysRevE.58.R5257).
- [53] C. G. R. Geddes et al. “Plasma-density-gradient injection of low absolute-momentum-spread electron bunches”. In: *Phys. rev. lett.* 100 (21 2008), p. 215004. DOI: [10.1103/PhysRevLett.100.215004](https://doi.org/10.1103/PhysRevLett.100.215004).
- [54] K. Schmid et al. “Density-transition based electron injector for laser driven wakefield accelerators”. In: *Phys. rev. st accel. beams* 13 (9 2010), p. 091301. DOI: [10.1103/PhysRevSTAB.13.091301](https://doi.org/10.1103/PhysRevSTAB.13.091301).
- [55] T.Zh. Esirkepov and A.S. Pirozhkov. In: 1 (2021). DOI: [INPREPARATION](https://doi.org/10.1103/PhysRevSTAB.13.091301).
- [56] A. Sagisaka et al. “Observation of burst intensification by singularity emitting radiation generated from relativistic plasma with a high-intensity laser”. In: *High energy density physics* 36 (2020). DOI: [10.1016/J.HEDP.2020.100751](https://doi.org/10.1016/j.hedp.2020.100751).
- [57] A.A. Andreev et al. “Effect of a laser prepulse on fast ion generation in the interaction of ultra-short intense laser pulses with a limited-mass foil target”. In: *Plasma physics and controlled fusion* 48 (2006). DOI: [10.1088/0741-3335/48/11/003](https://doi.org/10.1088/0741-3335/48/11/003).
- [58] M. Roth et al. “Energetic ions generated by laser pulses: a detailed study on target properties”. In: *Phys. rev. st accel. beams* 5 (2002). DOI: [10.1103/PhysRevSTAB.5.061301](https://doi.org/10.1103/PhysRevSTAB.5.061301).
- [59] J. Fuchs et al. “Laser-foil acceleration of high-energy protons in small-scale plasma gradients”. In: *Phys. rev. lett.* 99 (2007). DOI: [10.1103/PhysRevLett.99.015002](https://doi.org/10.1103/PhysRevLett.99.015002).

- [60] F. Lindau et al. “Laser-accelerated protons with energy-dependent beam direction”. In: *Phys. rev. lett.* 95 (2005). DOI: [10.1103/PHYSREVLETT.95.175002](https://doi.org/10.1103/PhysRevLett.95.175002).
- [61] Y. Sentoku et al. “High-energy ion generation in interaction of short laser pulse with high-density plasma”. In: *Applied physics b* 74 (2002). DOI: [10.1007/s003400200796](https://doi.org/10.1007/s003400200796).
- [62] J.T. Seo, S.H. Yoo, and S.J. Hahn. “Effects of underdense preplasma on the energetic proton generation in ultraintense short laser pulse interaction with an overdense plasma slab”. In: *Journal of the physical society of japan* (2007). DOI: [10.1143/JPSJ.76.114501](https://doi.org/10.1143/JPSJ.76.114501).
- [63] H.J. Lee et al. “Enhancement of high-energy ion generation by preplasmas in the interaction of an intense laser pulse with overdense plasmas”. In: *Physics of plasmas* 11 (2004). DOI: [10.1063/1.1650844](https://doi.org/10.1063/1.1650844).
- [64] J. Badziak. “Laser-driven ion acceleration: methods, challenges and prospects”. In: *Journal of physics: conference series* 959 (2018). DOI: [10.1088/1742-6596/959/1/012001](https://doi.org/10.1088/1742-6596/959/1/012001).
- [65] S. C. Wilks et al. “Energetic proton generation in ultra-intense laser–solid interactions”. In: *Physics of plasmas* 8 (2001). DOI: [10.1063/1.1333697](https://doi.org/10.1063/1.1333697).
- [66] M. Macchi A.and Borghesi and M. Passoni. “Ion acceleration by superintense laser-plasma interaction”. In: *Rev. mod. phys.* 85 (2 2013), pp. 751–793. DOI: [10.1103/REVMODPHYS.85.751](https://doi.org/10.1103/REVMODPHYS.85.751).
- [67] J. W. Yoon et al. “Realization of laser intensity over  $10^{23}$  w/cm<sup>2</sup>”. In: *Optica* 8.5 (2021). DOI: [10.1364/OPTICA.420520](https://doi.org/10.1364/OPTICA.420520).

- [68] S. Fourmaux et al. “Pedestal cleaning for high laser pulse contrast ratio with a 100 tw class laser system”. In: *Opt. express* 19 (2011). DOI: [10.1364/OE.19.008486](https://doi.org/10.1364/OE.19.008486).
- [69] A. Lévy et al. “Double plasma mirror for ultrahigh temporal contrast ultraintense laser pulses”. In: *Optics letters* 32 (3 2007). DOI: [10.1364/OL.32.000310](https://doi.org/10.1364/OL.32.000310).
- [70] I. Musgrave et al. “Review of laser diagnostics at the vulcan laser facility”. In: *High power laser science and engineering* 3 (2015). DOI: [10.1017/HPL.2015.27](https://doi.org/10.1017/HPL.2015.27).
- [71] K. Hiromitsu et al. “High temporal and spatial quality petawatt-class ti:sapphire chirped-pulse amplification laser system”. In: *Opt. lett.* 35.10 (2010). DOI: [10.1364/OL.35.001497](https://doi.org/10.1364/OL.35.001497).
- [72] H. Kiriya et al. “Temporal contrast enhancement of petawatt-class laser pulses”. In: *Opt. lett.* 37.16 (2012). DOI: [10.1364/OL.37.003363](https://doi.org/10.1364/OL.37.003363).
- [73] P. McKenna et al. *Laser-plasma interactions and applications*. Springer, 2013. DOI: [10.1007/978-3-319-00038-1](https://doi.org/10.1007/978-3-319-00038-1).
- [74] C. K. Birdsall and A. B. Langdon. *Plasma physics via computer simulation*. CRC Press, 1991. DOI: [10.1201/9781315275048](https://doi.org/10.1201/9781315275048).
- [75] J. J. MacFarlane, I. E. Golovkin, and P. R. Woodruff. “Helios-cr – a 1-d radiation-magnetohydrodynamics code with inline atomic kinetics modeling”. In: *Journal of quantitative spectroscopy and radiative transfer* 99.1 (2006), pp. 381–397. DOI: [10.1016/J.JQSRT.2005.05.031](https://doi.org/10.1016/J.JQSRT.2005.05.031).
- [76] T. D. Arber et al. “Contemporary particle-in-cell approach to laser-plasma modelling”. In: *Plasma physics and controlled fusion* 57.11 (2015), p. 113001. DOI: [10.1088/0741-3335/57/11/113001](https://doi.org/10.1088/0741-3335/57/11/113001).
- [77] T. Tabak et al. “Ignition and high gain with ultrapowerful lasers”. In: *Physics of plasmas* 1.5 (1994). DOI: [10.1063/1.870664](https://doi.org/10.1063/1.870664).

- [78] A. Higginson et al. “Near-100 mev protons via a laser-driven transparency-enhanced hybrid acceleration scheme”. In: *Nature communications* 9.1 (2018). DOI: [10.1038/s41467-018-03063-9](https://doi.org/10.1038/s41467-018-03063-9).
- [79] B. Gonzalez-Izquierdo et al. “Optically controlled dense current structures driven by relativistic plasma aperture-induced diffraction”. In: *Nature physics* 12.5 (2016). DOI: [10.1038/NPHYS3613](https://doi.org/10.1038/NPHYS3613).
- [80] R. J. Gray et al. “Laser pulse propagation and enhanced energy coupling to fast electrons in dense plasma gradients”. In: *New journal of physics* 16 (2014). DOI: [10.1088/1367-2630/16/11/113075](https://doi.org/10.1088/1367-2630/16/11/113075).
- [81] M. R. Siegrist. “Self-focusing in a plasma due to ponderomotive forces and relativistic effects”. In: *Optics communications* 16.3 (1976). DOI: [10.1016/0030-4018\(76\)90028-6](https://doi.org/10.1016/0030-4018(76)90028-6).
- [82] J. Vieira, J. T. Mendonça, and F. Quéré. “Optical control of the topology of laser-plasma accelerators”. In: *Physical review letters* 121.5 (2018). DOI: [10.1103/PhysRevLett.121.054801](https://doi.org/10.1103/PhysRevLett.121.054801).
- [83] M. Borghesi et al. “Proton imaging: a diagnostic for inertial confinement fusion / fast ignitor studies”. In: *Plasma physics and controlled fusion* 43.12A (2001). DOI: [10.1088/0741-3335/43/12A/320](https://doi.org/10.1088/0741-3335/43/12A/320).
- [84] L. Willingale et al. “High-power kilojoule class laser channeling in millimeter-scale underdense plasma”. In: *Physical review letters* 106.10 (2011). DOI: [10.1103/PhysRevLett.106.105002](https://doi.org/10.1103/PhysRevLett.106.105002).
- [85] D. J. Bradley, B. Liddy, and W. E. Sleat. “Direct linear measurement of ultra-short light pulses with a picosecond streak camera”. In: *Optics communications* 2.8 (1971). DOI: [10.1016/0030-4018\(71\)90252-5](https://doi.org/10.1016/0030-4018(71)90252-5).

- [86] S. Jackel, B. Perry, and M. Lubin. “Dynamics of laser-produced plasmas through time-resolved observations of the  $2\omega_0$  and  $\frac{3}{2}\omega_0$  harmonic light emissions”. In: *Physical review letters* 37.95 (1976). DOI: [10.1103/PhysRevLett.37.95](https://doi.org/10.1103/PhysRevLett.37.95).
- [87] L. Volpe et al. “Proton radiography of laser-driven imploding target in cylindrical geometry”. In: *Physics of plasmas* 18.1 (2011). DOI: [10.1063/1.3530596](https://doi.org/10.1063/1.3530596).
- [88] A. J. Mackinnon et al. “Proton radiography as an electromagnetic field and density perturbation diagnostic”. In: *Review of scientific instruments* 75.10 (2004). DOI: [10.1063/1.1788893](https://doi.org/10.1063/1.1788893).
- [89] H. Shiraga et al. “Two-dimensional sampling-image x-ray streak camera for ultrafast imaging of inertial confinement fusion plasma”. In: *Review of scientific instruments* 70.1 (1999). DOI: [10.1063/1.1149285](https://doi.org/10.1063/1.1149285).
- [90] J. S. Green et al. “Enhanced proton flux in the mev range by defocused laser irradiation”. In: *New journal of physics* 12 (2010). DOI: [10.1088/1367-2630/12/8/085012](https://doi.org/10.1088/1367-2630/12/8/085012).
- [91] P. Antici et al. “Time and space resolved interferometry for laser-generated fast electron measurements”. In: *Review of scientific instruments* 81.11 (2010). DOI: [10.1063/1.3499250](https://doi.org/10.1063/1.3499250).
- [92] M. C. Kaluza et al. “Time-sequence imaging of relativistic laser-plasma interactions using a novel two-color probe”. In: *Applied physics b* 92 (2008). DOI: [10.1007/s00340-008-3150-z](https://doi.org/10.1007/s00340-008-3150-z).
- [93] K. Ward. “A short history of telecommunications transmission in the uk”. In: *The journal of the communications network* 5.1 (2006).

- [94] L. B. Da Silva et al. “Electron density measurements of high density plasmas using soft x-ray laser interferometry”. In: *Physical review letters* 74.20 (1995). DOI: [10.1103/PHYSREVLETT.74.3991](https://doi.org/10.1103/PhysRevLett.74.3991).
- [95] T. J. M. Boyd and J. J. Sanderson. “The physics of plasmas”. In: (2003).
- [96] R. Fedosejevs, X. F. Wang, and G. D. Tsakiris. “Onset of relativistic self-focusing in high density gas jet targets”. In: *Physical review e* 56.4 (1997). DOI: [10.1103/PHYSREVE.56.4615](https://doi.org/10.1103/PhysRevE.56.4615).
- [97] D. Umstadter. “Relativistic laser-plasma interactions”. In: *Journal of applied physics* 36.8 (2003). DOI: [10.1088/0022-3727/36/8/202](https://doi.org/10.1088/0022-3727/36/8/202).
- [98] F. Wagner et al. “Pre-plasma formation in experiments using petawatt lasers”. In: *Optics express* 22.24 (2014). DOI: [10.1364/OE.22.029505](https://doi.org/10.1364/OE.22.029505).
- [99] S. C. Wilks and W. L. Kruer. “Absorption of ultrashort, ultra-intense laser light by solids and overdense plasmas”. In: *Ieee journal of quantum electronics* 33.11 (1997). DOI: [10.1109/3.641310](https://doi.org/10.1109/3.641310).
- [100] P. Mora. “Plasma expansion into a vacuum”. In: *Physical review letters* 90.18 (2003). DOI: [10.1103/PHYSREVLETT.90.185002](https://doi.org/10.1103/PhysRevLett.90.185002).
- [101] J. Fuchs et al. “Laser-driven proton scaling laws and new paths towards energy increase”. In: *Nature phys* 2 (2006).
- [102] D. N. Gupta et al. “Plasma density ramp for relativistic self-focusing of an intense laser”. In: *Journal of the optical society of america b* 24.5 (2007). DOI: [10.1364/JOSAB.24.001155](https://doi.org/10.1364/JOSAB.24.001155).
- [103] C. M. Brenner et al. “Dependence of laser accelerated protons on laser energy following the interaction of defocused, intense laser pulses with ultra-thin targets”. In: *Laser and particle beams* 29.1 (2011). DOI: [10.1017/S0263034611000395](https://doi.org/10.1017/S0263034611000395).

- [104] P. McKenna et al. “Effects of front surface plasma expansion on proton acceleration in ultraintense laser irradiation of foil targets”. In: *Laser and particle beams* 26 (2008). DOI: [10.1017/S0263034608000657](https://doi.org/10.1017/S0263034608000657).
- [105] H. W. Powell et al. “Proton acceleration enhanced by a plasma jet in expanding foils undergoing relativistic transparency”. In: *New journal of physics* 17.10 (2018). DOI: [10.1088/1367-2630/17/10/103033](https://doi.org/10.1088/1367-2630/17/10/103033).
- [106] C. M. Brenner, P. McKenna, and D. Neely. “Modelling the effect of laser focal spot size on sheath- accelerated protons in intense laser-foil interactions”. In: *Plasma physics and controlled fusion* 56.8 (2014). DOI: [10.1088/0741-3335/56/8/084003](https://doi.org/10.1088/0741-3335/56/8/084003).
- [107] R. J. Gray et al. “Enhanced laser-energy coupling to dense plasmas driven by recirculating electron currents”. In: *New journal of physics* 20 (2018). DOI: [10.1088/1367-2630/AAB089](https://doi.org/10.1088/1367-2630/AAB089).
- [108] N. P. Dover et al. “Effect of small focus on electron heating and proton acceleration in ultrarelativistic laser-solid interactions”. In: *Physical review letters* 124 (2020). DOI: [10.1103/PhysRevLett.124.084802](https://doi.org/10.1103/PhysRevLett.124.084802).
- [109] M. Coury et al. “Influence of laser irradiated spot size on energetic electron injection and proton acceleration in foil targets”. In: *Applied physics letters* 100 (2012). DOI: [10.1063/1.3685615SUB](https://doi.org/10.1063/1.3685615SUB).
- [110] D. Rusby et al. “Escaping electrons from intense laser-solid interactions as a function of laser spot size”. In: *Epj web of conferences* 167 (2018). DOI: [10.1051/EPJCONF/201816702001](https://doi.org/10.1051/EPJCONF/201816702001).
- [111] K. D. Xiao et al. “Multidimensional effects on proton acceleration using high-power intense laser pulses”. In: *Physics of plasmas* 25.2 (2018). DOI: [10.1063/1.5003619](https://doi.org/10.1063/1.5003619).

- [112] H. Suk et al. “Plasma electron trapping and acceleration in a plasma wake field using a density transition”. In: *Phys. rev. lett.* 86 (6 2001). DOI: [10.1103/PHYSREVLETT.86.1011](https://doi.org/10.1103/PhysRevLett.86.1011).